

OBTAINING ADVANCED OXIDE THIN FILMS AT
LOW TEMPERATURE BY CHEMICAL METHODS.
THERMAL ANALYSIS OF THIN FILMS

Daniel SÁNCHEZ RODRÍGUEZ

Dipòsit legal: Gi. 2079-2015
<http://hdl.handle.net/10803/328723>



<http://creativecommons.org/licenses/by-nc/4.0/deed.ca>

Aquesta obra està subjecta a una llicència Creative Commons Reconeixement-
NoComercial

Esta obra está bajo una licencia Creative Commons Reconocimiento-NoComercial

This work is licensed under a Creative Commons Attribution-NonCommercial licence



PhD Thesis

Obtaining advanced oxide thin films at low temperatures by chemical methods. Thermal analysis of thin films.

Daniel Sánchez Rodríguez

2015



PhD Thesis

**Obtaining advanced oxide thin films at low
temperature by chemical methods. Thermal analysis
of thin films.**

Daniel Sánchez Rodríguez

2015

DOCTORAL PROGRAMME IN EXPERIMENTAL SCIENCES AND SUSTAINABILITY

Supervisors: Dr. Jordi Farjas Silva

PhD thesis submitted to aim for PhD degree for the University of Girona



Dr. Jordi Farjas Silva of Universitat de Girona,

I DECLARE:

That the thesis entitled "Obtaining advanced oxide thin films at low temperature by chemical methods. Thermal analysis of thin films", presented by Daniel Sánchez Rodríguez to obtain a doctoral degree, has been completed under our supervision and meets the requirements to opt for an International Doctorate.

For all intents and purposes, I hereby sign this document.

Girona, May 21st 2015

A la meva mare, el meu pare i el meu germà.

Acknowledgements

First of all, I wish to express my sincere thanks to my supervisor, Dr. Jordi Farjas Silva, and to Prof. Pere Roura Grabulosa. I have no words to express my gratitude for all they have taught me and for all the time they have dedicated to me. Their commitment and passion for science has inspired me and made me redefine my career aims. I feel fortunate to have worked with them.

I would like to thank for the technical support I got from Serveis Tècnics de Recerca (STR) of the University of Girona and particularly, from Dr. Joan Pere López Olmedo. I would like to highlight above everything the positive attitude and infinite patience he had with me.

I would also like to acknowledge the Department of Materials Science and Biotechnology of Ehime University and especially Prof. Yahiro who gave me the opportunity of joining his group. It has been a rewarding experience both, at personal and professional level. In addition, all the people I met in Matsuyama made me feel like home even though I was at 10.000 km far from my country. I took with me very pleasant memories from Japan. Moreover, the greatest reward I took from there is my girlfriend, Ayu. Thank you for make my life more enjoyable.

I want to make especial mention of my family: My mother, my father and my brother. Without their effort and support, I would never have come this far. They had been a key part of my success. I will always be thankful to them. I can never thank them enough.

Last but not least, I want to devote a few words to my friends: Laura, Ernest, Edu, Hugas, Miquel, Quim and Alex. Everything is much easier when you are surrounded by good people. The time we have spent doing simply nothing is not time wasted.

LIST OF PUBLICATIONS

Publications derived from this thesis:

- **D. Sánchez-Rodríguez**, J. Farjas, P. Roura, Thermal Analysis for Low Temperature Synthesis of Oxide Thin Films from Chemical Solutions, Journal of Physical Chemistry C, Vol. 117, No. 39, pp 20133-20138, October, 2013. Impact factor: 4.772. 1st quartile.
- **D. Sánchez-Rodríguez**, H. Eloussifi, J. Farjas, P. Roura, M. Dammak, Thermal gradients in thermal analysis experiments: Criteria to prevent inaccuracies when determining sample temperature and kinetic parameters, Thermochimica Acta, Vol. 589, No. 1, pp. 37-46, August, 2014. Impact factor: 2.184. 2nd quartile.
- **D. Sánchez-Rodríguez**, J.P. López-Olmedo, J. Farjas, P. Roura, Determination of thermal conductivity of powders in different atmospheres by differential scanning calorimetry, Journal of Thermal Analysis and Calorimetry, Vol. 121, No. 1, pp. 469-473, January, 2015. Impact factor: 2.042. 3rd quartile.

Manuscripts in preparation derived from this thesis:

- **D. Sánchez-Rodríguez**, J. Farjas, P. Roura, Thermal explosion: When is a solid-state self-sustained reaction front formed? The Frank-Kamenetskii criterion revisited, 2015
- **D. Sánchez-Rodríguez**, H. Wada, S. Yamaguchi, J. Farjas, H. Yahiro, Self-propagating high-temperature synthesis of LaMO₃ perovskite-type oxide using heteronuclearcyano metal complex precursors, 2015

LIST OF ABBREVIATIONS

Activation energy	E_A
Adiabatic temperatura	T_{AD}
Alternating direction implicit method	ADI
Amplitude of the modulate heat flow	A_{HF}
Amplitude of the modulation	A_T
Characteristic diffusion time	t_D
Characteristic reaction time scale	t_R
Chemical solution deposition	CSD
Combustion synthesis	CS
Cyano complex	CN
Degree of transformation during the induction period	α_{Ind}
Degree of transformation or conversion factor	α
Density	ρ
Determining temperatura	T_0
Differential scanning calorimetry	DSC
Differential thermal analysis	DTA
Dimensionless characteristic linear dimension	$\delta^{(2D)}$
Dimensionless inner radius	ε
Dimensionless radial space coordinate	ζ
Dimensionless reciprocal of the adiabatic temperature	η
Dimensionless sample height	δ
Dimensionless temperatura	ϑ
Dimensionless time	τ
Dimensionless vertical space cordinate	ζ
Evolved Gas Analysis	EGA
Finite difference method	FDM

Finite-element method	FEM
Frank-Kamenestkii parameter	Λ
Furnace temperatura	T_f
Gas phase combustión	GC
Heating rate	β
Inner radius of the reaction vessel	R
Maximum rate transformation temperature	T_{CHR}
Metal organic decomposition	MOD
Moving particle semi-implicit method	MPS
Period	P
Pre-exponential constant	A
Radial space coordinate	r
Sample height or film thickness	H
Sample mass	m
Sample volumen	V
Self-propagating high-temperature synthesis	SHS
Simultaneous thermal analysis	STA
Solid flame phenomenon	SFP
Solid state combustión	SSC
Solution combustión	SC
Solution combustion synthesis	SCS
Specific heat capacity	c
Specific heat of reaction	q
Temperature	T
Temperature of an isothermal treatment	T_{ISO}
Thermal analysis	TA
Thermal conductivity	λ
Thermal diffusivity	a
Thermogravimetry	TG

Time	t
Universal gas constant	R_G
Vertical space coordinate	z
Volume averaged degree of transformation	$\bar{\alpha}$
Volumetric combustion synthesis	VCS
Yttrium trifluoroacetate	$Y(TFA)_3$

LIST OF FIGURES

Figure I-1. Geometry analyzed. The sample is placed inside a cylindrical vessel without a cover.	15
Figure I-2. Typical DSC signal for a polymer.....	21
Figure I-3. Common TG curve of the decomposition of a metal-organic precursor.....	22
Figure I-4. (a) power–compensation DSC; (a) Heat flux DSC.....	23
Figure I-5. The four methods for measuring c_p with a conventional DSC (a and b) and modulated DSC (c and d) that we have mentioned above. From Measurement by differential scanning calorimetry of specific heat capacity variation due to crystallization: Application to amorphous silicon by P. Roura et al., <i>Thermochimica Acta</i> , Vol. 522, pp. 161–165, 2010.	26
Figure III-1. tG and DTA (or DSC) curves of the thermal decomposition of several metal oxide precursors.	46
Figure III-2. TG curves for the decomposition of $Y(TFA)_3$ powders when heated at 20 K/min and significant staves of the decomposition curse.....	47
Figure III-3. TG curves of the decomposition of $Y(TFA)_3$ 250 nm film.....	48
Figure III-4. XRD curves of In_2O_3 synthesized from precursor powders and from a 450 nm thin filmannealed at 250 and 200°C, respectively.	49
Figure IV-1. Schematic representation of the geometry analyzed.....	54
Figure IV-2. $C(h/R)$ calculated from numerical integration	56
Figure IV-3. Evolution of the thermal decomposition of $Ba(TFA)_2$ for different sample masses.	57
Figure IV-4. Comparative between 2D model and the equivalent 1D model.	57
Figure IV-5. Rate of the diffusion and reation times at which the maximum temperature difference within the sample related to the heat of the exothermic reaction is equal to 1K....	58
Figure IV-6. Evolution of the thermal decomposition of $Ba(TFA)_2$ in the form of powders and films obtained from TG experiments performed at different heating rates.	59
Figure IV-7. 2D simulations of the evolution of thermal decomposition of $Ba(TFA)_2$ for a fixed mass of 7.3 mg and inner crucible radius of 2 mm, and for different heating rates.	59
Figure IV-8. Determination of the activation eregy of simulations shown in Fig. IV-7 using modified Ortega's isoconversional method.	59

Figure IV-9. Experimental activation energy of the thermal degradation of Ba(TFA) ₂ powders determined with the modified Ortega's isoconversional method.....	60
Figure IV-10. Experimental activation energy of the thermal decomposition of Y(TFA) ₃ determined with the modified Ortega's isoconversional method.....	60
Figure IV-11. Evolution of the thermal degradation of Y(TFA) ₃ in the form of powders and films obtained from TG experiments performed at different heating rates.	60
Figure IV-12. Comparison between the experimental results plotted in Fig. IV-11 and the related numerical simulations.....	61
Figure V-1. Geometric appearance of the hemispherical pan placed on the sensor disk.	66
Figure V-2. SEM micrographs of the alumina, iron, tin oxide and Ba(TFA) ₂ powders.	66
Figure V-3. Typical DSC melting curves with and without powders.	67
Figure V-4. Temperature dependence of the thermal conductivity of alumina powders in several gases.	68
Figure VI-1. Geometry analyzed. The sample is placed inside a cylindrical vessel without a cover.....	80
Figure VI-2. Thermal decomposition of Y(TFA) ₃ powders inside an alumina crucible.....	82
Figure VI-3. 1D numerical temperature profiles along cylinder axis ($r=0$) at the different stages of the Y(TFA) ₃ thermal decomposition powders inside an alumina crucible.....	84
Figure VI-4. Value of $\Lambda_{cr, Iso, 0}^{(1D)}$ determined numerically for an isothermal treatment and assuming a semi-infinite slab (or thin film) geometry for different values of the dimensionless parameters ϑ_{Iso} and η	87
Figure VI-5 Value of $\Lambda_{cr, Iso}^{(1D)}$ determined numerically for a semi-infinite slab and an infinite cylinder for an isothermal treatment.....	88
Figure VI-6. Percent error of the critical sample size calculated from Eq. VI-19 using our approximate solution and the constant value of the FK model for a semi-infinite slab, $\Lambda_{cr} = 0.88$, and for an infinite cylinder, $\Lambda_{cr} = 2.0$	89
Figure VI-7. Value of $\Lambda_{cr, CHR}^{(1D)}$ determined numerically for a semi-infinite slab and an infinite cylinder for a non-isothermal treatment..	91
Figure VI-8. Critical sample height determined from the numerical simulation and from Eqs. VI-19 and VI-22 for a semi-infinite slab geometry and a non-isothermal treatment.....	92
Figure VI-9. Percent error of the critical sample size calculated from Eq. 19 using our approximate solution for a semi-infinite slab, Eq. VI-22, and for an infinite cylinder, Eq. VI-25, for a non-isothermal temperature program.	93

Figure VI-10. Parameter $C^{(2D)}$ calculated numerically for an isothermal treatment and a non-isothermal treatment for different values of parameters η and ϑ_{iso} or β	95
Figure VI-11. Percent error of the critical sample size, $d^{(2D)}$, calculated from Eq. VI-19 using our solution, Eq. VI-26, for an isothermal and non-isothermal temperature program..	96
Figure VI-12. Experimental and numerical evolution of the thermal evolution of Ba(TFA) ₂ powders inside an alumina crucible.....	98
Figure VI-13. Plot of the critical thickness versus the substrate thickness.....	100
Figure VII-1. The apparatus of gas-flow system and the locations of thermocouple detectors at on the sample, such as entrance (i), middle (ii), and exit sites(iii)	113
Figure VII-2. Evolution of the thermal decomposition of La[Fe(CN) ₆] under O ₂ (a), air (b) and N ₂ (c) for different sample masses. Plot (d) shows a comparison of the characteristic thermal decomposition for high sample masses under different atmospheres.....	114
Figure VII-3. Evolution of the thermal decomposition of La[Co(CN) ₆] under O ₂ (a), air (b) and N ₂ (c) for different sample masses. Plot (d) shows a comparison of the characteristic thermal decomposition for high sample masses under different atmospheres including DTA measurement.....	115
Figure VII-4. Evolution of the temperature at different positions of the sample: the extreme closer to the gas entrance(i), in the middle (ii) and at the extreme opposite to the gas entrance(iii). La[Fe(CN) ₆] treated under different atmospheres and during different times: (a) N ₂ -300°C-1h, (b) Air-300°C-1h (c) O ₂ -250°C. The furnace is powered off after combustion starts (approximately 40min. at 250°C).....	116
Figure VII-5. Evolution of the temperature at different positions of the sample: the extreme closer to the gas entrance (i), in the middle (ii) and at the extreme opposite to the gas entrance(iii). La[Co(CN) ₆] treated under different atmospheres and during different times ..	117
Figure VII-6. XRD patterns of La[Fe(CN) ₆].5H ₂ O treated under different atmospheres and during different times.....	118
Figure VII-7. XRD patterns of La[Co(CN) ₆].5H ₂ O treated under different atmospheres and during different times	118
Figure VII-8. XRD patterns of LaFeO ₃ produced by SHS.....	120
Figure VII-9. XRD patterns of LaCoO ₃ produced by SHS..	120
Figure VII-10. Photographs of LaFeO ₃ (a) and LaCoO ₃ (b) samples and its respectively perovskite-type oxides produced by SHS.....	121
Figure VII-11. SEM micrographs of LaFeO ₃ produced by SHS at an ignition temperature of 150°C, 100°C, 50°C, and room temperature.	123

Figure VII-12. SEM micrographs of LaCoO_3 produced by SHS at an ignition temperature of 150°C, 100°C, 50°C, and room temperature. 124

LIST OF TABLES

Table I-1. B and C parameters for different approximations based on Eq. 84.	33
Table IV-1. Physical parameters of the Ba(TFA) ₃ and Y(TFA) ₃ metalorganic powders analyzed.	54
Table IV-2. Thermal parameters of different substrates.	56
Table V-1. Thermal conductivity of Al ₂ O ₃ , Fe, SnO ₂ , Ba(CF ₃ CO ₂) ₃ powders at the melting point of In in N ₂	67
Table V-2. Parameters and results of experiments carried out with powders in N ₂ at the melting point of In.	67
Table VI-1. Physical parameters of the two metal organic powders analyzed.	83
Table VI-2. Physical parameters of the substrates.	83
Table VI-3. Fixed physical parameters used in the validation of the models.	87
Table VI-4. Combustion threshold parameters.	96
Table VII-1. Experiments performed with the gas flow system.	119
Table VII-2. Specific surface area of perovskite-type oxides obtained by SHS.	122

LIST OF CONTENTS

ACKNOWLEDGEMENTS	III
LIST OF PUBLICATIONS.....	IV
LIST OF ABBREVIATIONS	V
LIST OF FIGURES.....	VIII
LIST OF TABLES	XII
LIST OF CONTENTS	XIII
SUMMARY	XVI
RESUM	XIX
RESUMEN	XXII
I. GENERAL INTRODUCTION.....	1
I.1. CHEMICAL SOLUTION SYNTHESIS.....	4
I.2. COMBUSTION.....	7
I.3. MODELLING OF HEAT TRANSFER.....	13
I.4. THERMAL ANALYSIS.....	20
I.4.1. <i>Specific heat Capacity</i>	24
I.4.2. <i>Thermal conductivity</i>	26
I.4.3. <i>Kinetic parameters</i>	29
I.5. REFERENCES.....	33
II. MAIN OBJECTIVES	41
III. THERMAL ANALYSIS FOR LOW TEMPERATURE SYNTHESIS OF OXIDE THIN FILMS FROM CHEMICAL SOLUTIONS	43
III.1. ABSTRACT	45
III.2. INTRODUCTION.....	45
III.3. EXPERIMENTAL SECTION	46
III.5. RESULTS AND DISCUSSION	47
III.6. CONCLUSIONS.....	49
III.7. ACKNOWLEDGMENTS.....	49
III.9. REFERENCES.....	50
IV. THERMAL GRADIENTS IN THERMAL ANALYSIS EXPERIMENTS: CRITERIONS TO PREVENT INACCURACIES WHEN DETERMINING SAMPLE TEMPERATURE AND KINETIC PARAMETERS	51
IV.1. ABSTRACT	53

IV.2.	INTRODUCTION.....	53
IV.3.	EXPERIMENTAL.....	54
IV.4.	NUMERICAL MODEL.....	54
IV.5.	TEMPERATURE DELAY RELATED TO HEAT CONDUCTION WITHIN THE SAMPLE.....	55
IV.6.	TEMPERATURE DELAY RELATED TO HEAT EVOLVED FROM THE SAMPLE.....	56
IV.7.	KINETIC ANALYSIS.....	58
IV.8.	CONCLUSIONS.....	61
IV.9.	ACKNOWLEDGMENTS.....	61
IV.10.	APPENDIX: CONDITIONS FOR HEATING A SAMPLE AT CONSTANT RATE FROM ITS SURFACE.....	61
IV.11.	APPENDIX B. SUPPLEMENTARY DATA.....	61
IV.12.	REFERENCES.....	61
V.	DETERMINATION OF THERMAL CONDUCTIVITY OF POWDERS IN DIFFERENT ATMOSPHERES BY DIFFERENTIAL SCANNING CALORIMETRY.....	63
V.1.	ABSTRACT.....	65
V.2.	INTRODUCTION.....	65
V.3.	EXPERIMENTAL.....	65
V.4.	METHOD DESCRIPTION.....	66
V.5.	RESULTS.....	67
V.6.	REFERENCES.....	69
VI.	THERMAL EXPLOSION: WHEN IS A SOLID-STATE SELF-SUSTAINED REACTION FRONT FORMED? THE FRANK-KAMENETSKII CRITERION REVISITED.....	70
VI.1.	ABSTRACT.....	72
VI.2.	INTRODUCTION.....	75
VI.3.	THE MODEL.....	79
VI.4.	ANALYTICAL SOLUTION.....	86
VI.4.1.	<i>Accuracy of FK model.....</i>	86
VI.4.2.	<i>Criterion under isothermal conditions and 1D.....</i>	88
VI.4.3.	<i>Critical condition under non-isothermal heating and 1D.....</i>	90
VI.4.4.	<i>Critical condition for a cylindrical vessel (2D).....</i>	93
VI.5.	EXPERIMENTAL RESULTS AND DISCUSSION.....	97
VI.6.	COMBUSTION IN FILMS AND SUBSTRATE INFLUENCE.....	99
VI.7.	CONCLUSIONS.....	101
VI.8.	REFERENCES.....	102
VII.	SELF-PROPAGATING HIGH-TEMPERATURE SYNTHESIS OF LAMO₃ PEROVSKITE-TYPE OXIDE USING HETERONUCLEAR CYANO METAL COMPLEX PRECURSORS.....	108
VII.1.	ABSTRACT.....	110

VII.2.	INTRODUCTION.....	111
VII.3.	EXPERIMENTAL DETAILS.....	112
VII.4.	RESULTS AND DISCUSSION.....	113
VII.4.1.	<i>Thermal analysis of the decomposition of La[Fe(CN)₆] and La[Co(CN)₆]</i>	113
VII.4.2.	<i>Production of LaFeO₃ and LaCoO₃ perovskite-type oxides via. SHS</i>	119
VII.5.	CONCLUSIONS.....	125
VII.6.	ACKNOWLEDGMENT.....	125
VII.7.	REFERENCES.....	125
VIII.	GENERAL DISCUSSION.....	130
VIII.1.	REFERENCES.....	138
IX.	GENERAL CONCLUSIONS.....	139

Summary

Due to their unique properties, functional oxides are currently attracting much attention. Advanced oxides are used in electronics, spintronics and superconductors, just to mention a few important applications. Chemical methods based on solutions or sol-gel are preferred over physical methods as they are more versatile and easily scalable for large batch production. Physical methods usually allow a better control of the final properties but the use of high vacuum significantly increases the cost and complicates large-scale use, thus, dramatically reducing its viability in industry. Among the chemical methods, chemical solution deposition (CSD) is one of the most promising low-cost routes for the preparation of advanced oxide films due to its simplicity, versatility and relative low cost. In the case of powders, a wide range of chemical methods that do not use vacuum systems exist, which we could classify in three categories: solid state reactions, synthesis from liquid solutions and vapour-phase reactions. The method we will deal with here, combustion synthesis (CS), belongs to the first category.

At present, combustion synthesis is a widespread method for the synthesis of advanced oxides from powders at low temperature while in the synthesis of films its use is at best scarce. Combustion synthesis is often referred as a low thermal budget method because the heat emanating from the precursors is used to produce advanced oxides at low temperatures. In fact, the heat evolved from the reaction can locally raise the temperature of the precursors many hundreds of degrees while keeping the system at a low temperature. This local overheating facilitates product formation and sintering in relatively short time periods with the advantage that energy consumption is minimal and no high temperature equipment is necessary. A self-sustained reaction supplies most of the power so the contribution of external heat sources is minimised. Depending on the ignition mode, it is worth distinguishing between self-propagating high-temperature synthesis (SHS) and volumetric combustion synthesis (VCS). In the former, a solid sample is locally ignited while in the latter the sample is heated uniformly until combustion occurs. Depending on the state of the reactants, we can also differentiate between solid state combustion (SSC), solution combustion (SC) and gas phase combustion (GC). This last one will not be analysed in this work. While both ignition modes are possible in SSC, in SC synthesis (SCS) only VCS is possible. SCS has recently attracted considerable interest in the synthesis of thin films due to the apparent possibility of fabricating electronic devices on flexible plastic substrates.

The aim of this work is to analyse chemical methods as a route to synthesise advanced oxides at low cost and low temperatures. In particular, we have successfully explored the combustion synthesis via SHS of a catalytic perovskite-type oxide from a heteronuclear cyano complex precursor presented in the form of powder. Heteronuclear cyano complex precursors were selected due to their structural similarity with perovskite-type oxides. The oxides obtained have surface areas that are up to two orders of magnitude greater than those of others similar perovskites produced using the same technique but obtained from other types of precursors.

We have also explored the possibility of synthesising thin films by SCS and spin coating has been used for CSD of the precursor candidates. In addition, we have examined low temperature synthesis of advanced oxides in the form of thin films through chemical methods. In particular, we have explored heat transfer to synthesise films via precursor combustion and concluded that thin films will hardly experience combustion. However, thin films can be obtained at lower temperatures than powders because of the enhanced gas transport mechanism that usually limits the decomposition rate.

Two main approaches have been used. On the one hand, we have studied the heat transfer in films and powders that are submitted to a controlled temperature program both analytically and numerically. In the case of systems undergoing an exothermic reaction two mechanisms control the system's temperature: the heat released by the reaction that tends to increase the temperature, and the heat transport to the crucible wall or film substrate that tends to reduce the temperature. Overheating occurs when heat generation dominates heat dissipation. We have focused the analysis on the conditions needed for a thermal explosion to occur in a solid sample reacting without any gas exchange with its surroundings. A minor correction allowed us to extend the Frank-Kamenetskii relationship to continuous heating systems and to cylindrical reactors without limiting its dimensions whilst at the same time significantly improving its accuracy.

On the other hand, chemical methods involve two heat treatments: pyrolysis to remove the organic compounds and annealing to grow the crystal oxide. Characterisation of the first process is essential to enhance chemical methods and to explore the viability of combustion as well as to explore low temperature synthesis of films. To this end, we have used thermal analysis methods (TA) since they permit the evolution of the process to be monitored for a specific temperature program under controlled ambient conditions (pressure and atmosphere composition). In particular we have used differential scanning calorimetry (DSC), thermogravimetry (TG) and Evolved Gas Analysis (EGA) methods. DSC also allowed us to

calculate system parameters such as heat capacity, activation energy, enthalpy and thermal conductivity. We have developed a new method to measure this last parameter since none of the already existing DSC's methods for measuring thermal conductivity is suitable when samples are in the form of uncompressed powders. The determination of these parameters allowed us to predict through numerical and analytical methods the occurrence of combustion and the evolution of the system under a set of given conditions. Furthermore, the numerical results may be compared to TA measurements so providing a way to check the validity of the theoretical models and numerical methods used in this work.

Finally, overheating depends on heat dissipation and, consequently, on sample thickness and mass. We have developed two analytical relationships that relate sample mass with the temperature gradient within the sample that provide a straightforward criterion for checking the reliability of the sample temperature in TA experiments.

Resum

Degut a les seves propietats úniques, avui en dia els òxids funcionals estan despertant un gran interès. Tan sols per citar alguna de les seves aplicacions més rellevants, es fan servir en el camp de l'electrònica, de l'espíntrònica i dels superconductors. Per a produir-los, es prefereixen els mètodes químics basats en solucions o sol-gels davant dels mètodes físics atès que són més versàtils i fàcilment escalables. Tot i que els mètodes físics proporcionen un millor control de les propietats finals, fan servir sistemes de buit que encareix el procés i redueixen dràsticament la viabilitat d'implementar-los a la indústria. Entre els mètodes químics, el dipòsit de solucions químiques (CSD) és una de les rutes de baix cost més prometedores per a la preparació de capes perquè es simple, versàtil i té un cost relativament baix. Pel que fa a la producció de pólvores d'òxids avançats, hi ha un ampli ventall de mètodes químics adients, que es podrien classificar en tres categories: les reaccions en fase sòlida, la síntesi a partir de solucions líquides i les reaccions en estat vapor. La síntesi per combustió, que pertany a la primera categoria, ha estat el mètode que s'ha tractat en aquest treball.

A l'actualitat, la síntesi per combustió és un mètode àmpliament utilitzat per a la producció de pólvores d'òxids avançats a baixa temperatura. Per contra, està poc estès per a la síntesi de capes. A la síntesi per combustió se la qualifica com una tècnica de baix cost tèrmic perquè aprofita la calor que prové dels precursors per a produir els òxids avançats a baixa temperatura. De fet, la calor despresada per la reacció pot elevar localment la temperatura dels precursors forces centenars de graus mentre el sistema es manté a temperatures baixes. Aquest sobreescalfament local facilita la formació i sinterització del producte en un temps relativament curt amb l'avantatge de que el consum d'energia es mínim i no es necessari disposar d'equipament per a altes temperatures. Una reacció autosostinguda proporciona gran part de la potència de forma que es minimitza la contribució de recursos de calor externs. Depenent del mode d'ignició, és important distingir entre la *self-propagating high-temperature synthesis* (SHS) i la *volumetric combustion synthesis* (VCS). Mentre que en el primer es provoca localment la ignició d'una mostra sòlida, en el segon la mostra sencera es escalfada uniformement fins a desencadenar una reacció de combustió. Depenent també de l'estat inicial dels reactius, podem diferenciar entre la combustió en estat sòlid (SSC), la combustió de solucions (SC) i la combustió en fase gas (GC). Aquesta última no serà analitzada en aquest treball. A diferència de la SSC que només pot fer servir la VCS com a mode d'ignició, a la SSC és possible fer servir tant la SHS com la VCS. Recentment, l'SSC ha despertat molt d'interès en la

síntesi de capes primes degut a la possibilitat aparent de fabricar aparells electrònics sobre substrats de plàstic.

L'objectiu d'aquest treball és analitzar mètodes químics com a ruta per a sintetitzar òxids avançats a baix cost i baixa temperatura. En particular, hem explorat la síntesi per combustió mitjançant l'SHS d'un òxid catalitzador amb estructura perovskita fent servir pólvores de precursors ciano complexes heteronuclears. Es van triar aquests precursors degut a que tenen una estructura similar a la perovskita. Els òxids que vam obtenir tenen unes àrees de superfície de fins a dos ordres de magnitud més grans que d'altres perovskites similars produïdes amb la mateixa tècnica però fent servir uns altres tipus de precursor.

També hem explorat la possibilitat de sintetitzar capes primes fent servir l'SCS i vam fer servir un *spin coater* per a dipositar els precursors que considerarem com a candidats. A més, hem examinat el per què de les baixes temperatures de síntesi d'òxids avançats quan es dipositen fent servir mètodes químics en forma de capes. En particular, hem explorat el transport de calor per a sintetitzar capes a través de la combustió de precursors conclouent que les capes primes rarament experimentaran una combustió. Tanmateix, les capes primes poden ser obtingudes a temperatures més baixes que les pólvores perquè es millora el mecanisme de transport de gas que normalment limita la velocitat de descomposició.

Vam enfocar l'estudi del transport de calor tenint en compte dos punts de vista. Per una banda, hem estudiat analíticament i numèricament la transferència de calor en capes i pólvores sotmeses a un programa de temperatura controlat. En el cas dels sistemes que experimenten reaccions exotèrmiques, dos són els mecanismes que controlen la temperatura del sistema: la calor despesa per la reacció que tendeix a augmentar la temperatura i el transport de calor cap a les parets del gresol o el substrat de les capes que tendeix a reduir la temperatura. Hi ha sobreescalfament quan la generació de calor domina sobre la dissipació. Nosaltres hem enfocat l'anàlisi en la condició necessària per que tingui lloc una combustió volumètrica en una mostra sòlida que reacciona sense intercanvi de gasos amb el seu entorn. Una petita correcció ens ha permès ampliar la relació de Frank-Kaminetskii per a sistemes d'escalfament continu i per a reactors cilíndrics de qualsevol dimensió. Alhora, hem millorat significativament la precisió.

Per altra banda, els mètodes químics involucren dos tractaments tèrmics: una piròlisi per a eliminar els compostos orgànics i un tractament per a créixer els cristalls dels òxids. La caracterització del primer procés és essencial per a millorar els mètodes químics i explorar la viabilitat de la combustió o explorar per què la síntesi de capes succeeix a baixa temperatura.

És per això que hem fet servir mètodes d'anàlisi tèrmica (AT) atès que permeten l'enregistrament de l'evolució d'un procés sota un programa específic de temperatura i unes condicions ambientals controlades (pressió i composició atmosfèrica). Molt especialment, hem fet servir la calorimetria diferencial de rastreig (CDR), la termogravimetria (TG) i l'anàlisi de gas evolvent (EGA). A més, el mètode DSC permet calcular paràmetres del sistema com la capacitat calorífica, l'energia d'activació, l'entalpia o la conductivitat tèrmica. Hem desenvolupat un nou mètode per a mesurar aquest últim paràmetre perquè cap dels mètodes que existeixen actualment són adients per a determinar-ho en pólvores sense premsar. La determinació d'aquests paràmetres et permet predir l'ocurrència de la combustió i l'evolució del sistema donades unes condicions. A part, els resultats numèrics poden ser comparats a les mesures de TA, proporcionant així una manera de validar els models teòrics i els mètodes numèrics que hem fet servir en aquest treball.

Finalment, el sobreescalfament depèn de la dissipació de calor i conseqüentment depèn del gruix de la mostra i de la seva massa. Hem desenvolupat dos relacions analítiques que relacionen la massa de la mostra amb el gradient de temperatura al llarg de la mostra i que proporciona un criteri directe per a comprovar la fiabilitat de la temperatura de la mostra als experiments de TA.

Resumen

Debido a sus propiedades únicas, hoy en día los óxidos funcionales están despertando un gran interés. Tan solo por citar alguna de sus aplicaciones más relevantes, se usan en los campos de la electrónica, la espintrónica y de los superconductores. Para producirlos, se prefieren los métodos químicos basados en soluciones o "sol-gels" frente a los métodos físicos pues son más versátiles y fácilmente escalables. Pese a que los métodos físicos proporcionan un mejor control de las propiedades finales, usan sistemas de vacío que encarecen el proceso y reducen drásticamente la viabilidad de implementarlos en la industria. De entre todos los métodos químicos, el Depósito de soluciones químicas (DSQ) es una de las rutas de bajo coste más prometedoras para la preparación de capas porque es simple, versátil y tiene un coste relativamente bajo. Por lo que concierne a la producción de polvo de óxidos avanzados, hay un amplio abanico de métodos químicos adecuados y se pueden clasificar en tres categorías: las reacciones en fase sólida, la síntesis a partir de soluciones líquidas o las reacciones en estado vapor. La síntesis por combustión, que pertenece a la primera categoría, ha sido el método con el que hemos tratado en este trabajo.

Actualmente, la síntesis por combustión es un método ampliamente utilizado para la producción de polvo de óxidos avanzados a baja temperatura. En cambio, está poco extendido para sintetizar capas. A la síntesis por combustión se la califica como una técnica de bajo coste térmico porque aprovecha el calor que proviene de los precursores para producir los óxidos avanzados a baja temperatura. De hecho, el calor desprendido por la reacción puede elevar localmente la temperatura de los precursores centenas de grados mientras el sistema se mantiene a temperaturas bajas. Este sobrecalentamiento local facilita la formación y sinterización del producto en un tiempo relativamente corto con la ventaja de que el consumo de energía es mínimo y no son necesarios equipos para altas temperaturas. Una reacción auto sostenida proporciona gran parte de la potencia de forma que se minimiza la contribución de recursos de calor externos. Dependiendo del modo de ignición, es importante distinguir entre la *self-propagating high-temperature synthesis* (SHS) y la *volumetric combustion synthesis* (VCS). Mientras que en el primero se provoca localmente la ignición de una muestra sólida, en el segundo la muestra entera se calienta uniformemente hasta desencadenar una reacción de combustión. Dependiendo también del estado inicial de los reactivos podemos diferenciar entre la combustión en estado sólido (SSC), la combustión de soluciones (SC) i la combustión en fase gas (GC). Ésta última no será analizada en este trabajo. A diferencia de la SCS que solo

puede combustionar mediante VCS, en la SSC es posible utilizar tanto la SHS como la VCS. Recientemente, la SCS ha despertado mucho interés en la síntesis de capas delgadas debido a la aparente posibilidad de fabricar aparatos electrónicos sobre sustratos de plástico.

El objetivo de este trabajo es analizar métodos químicos como ruta para sintetizar óxidos avanzados a un bajo coste y a baja temperatura. En particular, hemos explorado la síntesis por combustión mediante la SHS de un óxido catalizador con estructura perovskita utilizando polvo de precursores ciano complejos heteronucleares. Se escogieron estos precursores debido a que tienen una estructura similar a la perovskita. Los óxidos que obtuvimos tienen un área de superficie de hasta dos órdenes de magnitud mayores que otras perovskitas similares producidas mediante la misma técnica pero usando otro tipo de precursores.

También hemos explorado la posibilidad de sintetizar capas delgadas usando la SHS y usamos un *spin coater* para depositar aquellos precursores que consideramos como candidatos. Además, hemos examinado porqué los óxidos avanzados sintetizan a temperaturas más bajas cuando sus precursores se depositan en forma de capas usando métodos químicos. En particular, hemos explorado el transporte de calor para sintetizar capas a través de la combustión de precursores concluyendo que las capas delgadas raramente experimentarían una combustión. Aun así, las capas delgadas pueden ser obtenidas a temperaturas más bajas que el polvo porqué se mejora el mecanismo de transporte de gas que normalmente limita la velocidad de descomposición.

Para ello hemos utilizado dos enfoques distintos. Por un lado, hemos estudiado analítica y numéricamente la transferencia de calor en capas y polvo cuando son sometidos a un programa de temperatura controlado. En el caso de los sistemas que experimenten reacciones exotérmicas dos son los mecanismos que controlan la temperatura del sistema: el calor desprendido por la reacción que tiende a aumentar la temperatura y el transporte de calor hacia las paredes del crisol o el sustrato de las capas que tiende a reducir la temperatura. Hay sobrecalentamiento cuando la generación de calor domina sobre la disipación. Hemos enfocado el análisis en la condición necesaria para que tenga lugar una combustión volumétrica en una muestra sólida que reacciona sin intercambio de gases con su entorno. Una pequeña corrección nos ha permitido ampliar la relación de Frank Kaminestkii para sistemas de calentamiento continuo y para reactores cilíndricos de cualquier dimensión. A su vez, hemos mejorado significativamente la precisión.

Por otro lado, los métodos químicos involucran dos tratamientos térmicos: una pirólisis para eliminar los compuestos orgánicos y un tratamiento para crecer los cristales del óxido. La

caracterización del primer proceso es esencial para mejorar los métodos químicos y explorar la viabilidad de la combustión o explorar porqué la síntesis de capas sucede a baja temperatura. Es por ello que hemos utilizado métodos de análisis térmico (AT) pues permiten monitorizar la evolución de un proceso que está sometido a un programa específico de temperatura y bajo una atmósfera controlada (presión y composición atmosférica). En particular hemos usado la calorimetría diferencial de barrido (DSC), la termogravimetría (TG) y el análisis de gas evolvente (EGA). Además, el método DSC permite calcular parámetros del sistema como la capacidad calorífica, la energía de activación, la entalpía o la conductividad térmica. Hemos desarrollado un nuevo método para medir este último parámetro porque ninguno de los métodos que existen actualmente son adecuados para determinarlo en muestras que se encuentran en forma de polvo sin prensar. La determinación de estos parámetros permite predecir una posible combustión y la evolución del sistema dadas unas condiciones. A parte, los resultados numéricos pueden ser comparados a las mediciones de TA, proporcionando así una manera de validar los modelos teóricos y los métodos numéricos que hemos utilizado en este trabajo.

Finalmente, el sobrecalentamiento depende de la disipación de calor y consecuentemente depende del grosor de la muestra y de su masa. Hemos desarrollado dos relaciones analíticas que relacionan la masa de la muestra con el gradiente de temperatura a lo largo de la muestra y que proporcionan un criterio directo para comprobar la fiabilidad de la temperatura de la muestra en los experimentos de TA.

I. GENERAL INTRODUCTION

Nowadays the search for new metal oxides with interesting and useful properties is attracting much attention. The efforts being made on the research of functional oxides have already provided important discoveries which have a wide variety of applications in diverse fields such as electronics¹, spintronics² and superconductors³. However, the high costs involved in their synthesis are often a limitation for its commercial use. Therefore, it is important to explore the implementation of new low cost techniques that allow a large scale industrial production. This is why more resources are being allocated to develop chemical methods based on solutions or sol-gel, that unlike physical methods, they do not require the use of high vacuum systems which increases significantly the cost. The choice of the most suitable technique for the synthesis of any advanced oxide depends on the particular final properties that we are looking for. However, with regard to simplicity, versatility and low cost we will highlight two methods among the rest. In the one hand, chemical solution deposition (CSD) is one of the most promising routes for the production of films⁴. In the other hand, Combustion Synthesis (CS) has proven to be an effective low cost route for the production of powders⁵. In addition, these two routes share another interesting feature. Both stand out as low temperature synthesis routes. This is interesting in terms of costs but it is also interesting to expand the possible applications of the synthesized oxides such as using flexible plastic substrates in electronics.

Compared with traditional methods, decreased of temperature synthesis is especially remarkable on CS techniques; we have been able to synthesize at room temperature. This route takes advantage of the heat evolved during a self-sustained exothermic reaction so the power required from external heat resources is minimized. Moreover, due to the quasi-adiabatic nature of the process the sample can locally reach a temperature of hundreds of degrees higher than the surroundings⁵. This is particularly attractive for the synthesis of thin films since the substrate would remain at low temperature during film synthesis⁶⁻⁹. In this work we will only deal with solid state and liquid reactants, i.e. solid state combustion (SSC) and solution combustion (SC), and two combustion modes, i.e. the self-propagating high-temperature synthesis (SHS) and the volumetric combustion synthesis (VCS). In SHS ignition is induced by locally heating the sample and in the VCS the sample is homogeneously heated^{10,11}.

Our aim is to analyse chemical methods as a route to synthesize both, advanced oxides powders and films at low cost and low temperature. Regarding the synthesis of powders we will explore the synthesis of a catalytic perovskite-type oxide via SHS which. The novelty will be the use of heteronuclear cyano complex precursors which have attract great interest due to

their similar structure with perovskite-type oxides. With respect to the synthesis of films we will explore the possibility of synthesizing thin films by solution combustion synthesis (SCS) from precursors deposited via CSD. In addition, we will examine numerically, analytically and experimentally transport mechanisms in films since the enhanced gas transport in films with respect to powders allows to synthesize the oxides at lower temperatures.

In order to accomplish the above mentioned objectives we will analyse heat transfer in films and powders that are submitted to a controlled temperature program. For that purpose we will develop a numerical method based on finite differences. Additionally, we will use thermal analysis (TA) techniques for monitoring and characterizing the thermal processes involved during the heat treatments. Moreover, TA analysis will be essential for the determination of the system parameters that allow us to numerically predict the numerical occurrence of combustion.

I.1. Chemical solution synthesis

The synthesis of advanced oxides by chemical solution techniques has a great number of advantages independently of their geometry. In the case of thin films, the main advantage is associated with the production cost and the ease by which the process can be transferred to an industrial scale. The high cost of other methods, such as the physical ones, limit their use to the production of materials with superior properties or materials that are only available using these routes. This, however, is not the case for bulk geometries since powder processing methods are cheaper although these methods require high temperature and long processing treatments. Furthermore, they usually involve milling and mixing steps which may add impurities to the final product.¹² These problems can be overcome using solution routes, which also have additional advantages such as providing precise control of the stoichiometry and producing fully dense and homogeneous materials.

Chemical solution techniques differ from each other in the type of precursor and solvents used and in the chemical interactions that occur between the starting reagents. Among the wide variety of techniques, we will briefly present six of the most popular methods: the sol-gel process, the polymeric complexing method, the co-precipitation method, the hydrothermal method, the heteronuclear cyano complex method (abbreviated as the CN method) and the metal organic decomposition (MOD). Solution combustion synthesis (SCS) is also a chemical

solution synthesis method. However, we will discuss this method in depth in the following section which is devoted to combustion methods.

All the above-mentioned methods are suitable for the production of advanced oxide powders. Moreover, sol-gel process, polymeric complexing method and MOD are suitable for the fabrication of films by direct deposition of the initial chemical solution onto a substrate. This synthesis approach, which is called chemical solution deposition (CSD),⁴ is particularly suitable for the synthesis of films due to its low cost and flexibility.

Deposition can be carried out in any of the following four ways: dropping the solution onto a rotating substrate (spin coating), immersing a substrate in a solution bath (deep coating), spraying the solution (spray coating) or inkjet printing deposition.¹³⁻¹⁶ A subsequent thermal treatment completely decomposes the organic ligands and crystallizes the desired oxide.

- The sol-gel process is one of the most extended methods¹⁷⁻²⁰ and is characterised by the evolution of the liquid solution towards a gel while the solvent is eliminated. Hydrolysis and polycondensation are the two main reactions that take place before decomposition. Some of the advantages that make this technique so popular are the high phase purity and good compositional homogeneity. Besides, it is possible to control the composition of the final product by modifying the concentration of the precursors in the solution. In addition, powders produced using sol-gel process present high surface activity, which is particularly attractive for catalytic purposes. The use of alkoxide precursors and ethanol as a solvent is the most common combination.

- The so-called polymeric complexing method is a particular case of sol-gel method where the precursor salts are mixed with hydrocarboxylic acid to form a metal complexation or a polymer. The Pechini²¹⁻²³ and citrate^{24,25} processes belong to this method and are the most popular techniques. In both processes, metal nitrates are dissolved in water and citric acid. However, in the Pechini process a polyhydroxyalcohol, usually ethylene glycol, is also added.

- Metal organic decomposition routes (MOD) are a simple mixture of metal organic compounds that, unlike sol-gel routes, in which no significant condensation reactions take place. Thus, precursors do not react with the solvent to form gels. Both powders and films synthesised by this route have similar properties to those obtained from a sol-gel process. Traditionally, MOD has used 2-ethylhexanoate^{26,27} and di-neodecanoate²⁸ as precursors. However, cracking during film processing is a common problem related to the use of these precursors as a result of the large weight loss associated to the decomposition of their long organic ligands. For this reason short-chain carboxylates,²⁹ such as acetates,³⁰ are preferred to grow films. Most precursors employed in this work are of this kind.

- In the co-precipitation method, the precipitation of metal hydroxides is controlled by the value of the pH of the solution which determines the solubility of the potential products.³¹⁻³³ Thus, the pH value will be set depending on the oxide that one wants to synthesise. It is possible to use many different precursors, including hydroxides,³² carbonates, oxalates, formates, and citrates. Precipitation is caused by adding precipitating agents, such as hexamethylenetetramine,³⁴ diethylamine, NH_4OH ^{33,35,36} or hydrazine hydrate, formic acid, urea,³⁷ ammonium carbonate and oxalic acid,¹⁹ to the solution. Metal hydroxide nanopowders are collected by filtration and then thermally treated to obtain the desired oxide.

- Hydrothermal synthesis is also a chemical solution route based on high pressure treatments to achieve the precipitation of ceramic powders.³⁸⁻⁴¹ The solution is sealed and heated up to a few hundred degrees Celsius. Unlike the previous methods, in hydrothermal synthesis no calcination process is necessary, however, there is usually a subsequent thermal treatment. Crystal size and shape are controlled by mineralisers, which are additives that control the solubility of the precursors and can enhance the growth rate. Alkaline hydroxides^{38,39} or alkaline carbonate solutions³⁹ are the most common mineralisers.

- In 1968 Gallagher proposed a simple technique to prepare rare earth FeO_3 and CoO_3 from the thermal decomposition of heteronuclear cyano complexes.⁴² Later, Sadaoka et al. explored this chemical solution synthesis route to prepare perovskite-type oxide ABO_3 , i.e. the CN method.⁴³⁻⁴⁵ Cyano complex precursors are especially convenient for the preparation of this type of oxides due to their similar structure. The procedure is simple. A solution with the

appropriate amounts of an already available cyano complex precursor and a nitrate reacts to form a new cyano complex precursor. This new precursor precipitates in the form of nanopowders, which are collected by filtration. Thermal decomposition of this powder then leads to the desired perovskite-type oxide. Chapter VII explores the possibility of synthesising perovskite-type oxide powders via the combustion of this type of precursors.

I.2. Combustion

Ever since the days of the alchemists when the obsolete phlogiston theory was formulated, many studies have been undertaken in an effort to understand the complex mechanisms that control combustion. It is no longer a mystery that combustion processes are the self-sustained exothermic reaction between a fuel and an oxidant. It is these two key properties, self-sustenance and exothermicity, that make combustion processes so interesting in terms of technology and innovation since it is possible to synthesise materials that would otherwise require the contribution of external heat resources during long treatments. Beketov and Goldschmidt, in the 19th century, are widely credited with being the first to take advantage of self-sustained exothermic reactions in the manufacture of new products. However, it was not until the mid-1960s when combustion made its presence felt in industry as a new route in the production of materials. This was when the so-called solid flame phenomenon (SFP) was discovered that allowed the development of the first solid state combustion method (SSC), i.e. the self-propagating high temperature synthesis (SHS) introduced by Merzhanov et al.^{10,46,47}

SFP is characterised by the fact that all the compounds involved in the combustion process – even the intermediate and the final products – are in the solid state. Techniques that take advantage of SFP to synthesise materials are classified as SSC techniques. SSC has two variants depending on the ignition mode, SHS and volumetric combustion synthesis (VCS).¹¹ In SHS a solid sample is locally heated until a combustion wave is set while in VCS the sample is heated uniformly until it undergoes a thermal runaway known as thermal explosion. The VCS is more convenient for weakly exothermic compounds as ignition occurs at higher temperatures than in the case of SHS. Therefore, the sample achieves higher temperatures and the possibility to synthesise the oxide increases. Despite its simplicity, the implementation of SSC is limited by the search for new precursors. Notwithstanding, hundreds of compounds are today synthesized by SSC.^{11,47}

During the last few decades, a new combustion synthesis method – solution combustion synthesis (SCS) – has become popular.^{11,48} First reported by Kingsley et al. in 1988,⁴⁹ this technique involves the heating of an aqueous solution of a precursor salt and a suitable organic fuel, commonly urea,⁵⁰⁻⁵² until volumetric combustion occurs. However, we will show that some metal-organic precursor salts such as yttrium trifluoroacetate, $Y(CF_3COO)_3$, $Y(TFA)_3$ already contain both, the oxidiser and the fuel, and its decomposition becomes self-sustained under specific conditions. There are two different approaches depending on the temperature heating rate at which the solution is heated, i.e. uncontrolled or controlled thermal treatment. In the first, the temperature of the solution is rapidly increased and a violent chemical reaction occurs due to the huge amount of gas that evolves in a very short time. On the other hand, in the controlled thermal treatment approach, slow heating rates are used and melting and dehydration of the metal salts may occur before decomposition. The product properties may be modified depending on which approach is adopted.

The practical application of CS methods requires a thorough knowledge of the mechanisms involved in combustion processes. In particular, the conditions that make the ignition and propagation of a combustion wave possible need to be understood. A simultaneous analysis of the equations of heat transfer (Eq.1) and the equations of chemical kinetics (Eq. 2) led Frank Kaminetskii to formulate a parameter named after him that includes all the essential magnitudes for thermal ignition to occur. Kaminetskii's model was based on the assumptions of a purely conductive heat transfer problem and continuously distributed sources of heat. Furthermore, he assumed that physical magnitudes did not evolve with temperature. In this case, ignition and combustion can be described by the following set of equations. A partial differential equation that accounts for the heat conduction and a non-linear ordinary differential equation describing the heat generation from the chemical reaction:

$$\rho c \frac{\partial T}{\partial t} = \lambda \nabla^2 T + \rho q \frac{\partial \alpha}{\partial t} \quad (1)$$

$$\frac{\partial \alpha}{\partial t} = A e^{-E_A/R_G T} f(\alpha) \quad (2)$$

And the boundary conditions are:

$$\left. \frac{\partial T}{\partial r} \right|_{r=0} = 0, \quad T(R) = T_0 \quad (3)$$

For the sake of simplicity, Kaminetskii did not take into account the reagent consumption ($f(\alpha)=1$, a zero order reaction). His model was formulated for gases that were introduced in the system from an unlimited resource. Since for highly exothermic reactions, the precursor consumption prior to ignition is negligible, the model can be applied to solid state gasless reactions. Otherwise, a second parameter should be added to account for the reagent consumption. In addition, Kaminetskii assumed that the temperature rise below the explosion limit is small:

$$\Delta T = T - T_0 \ll T_0 \Rightarrow \exp\left(-\frac{E_a}{R_G T}\right) \approx \exp\left(-\frac{E_a}{R_G T_0}\right) \exp\left(-\frac{E_a}{R_G T_0^2} \Delta T\right) \quad (4)$$

The latter approximation is equivalent to the assumption that

$$\frac{E_a}{R_G T_0} \ll 1$$

Roura et. al.⁵³ analysed the value of this parameter for most common reactions carried out under constant heating rate conditions. Typical values of thermal decomposition of most molecules, for ease of reference, are within the $1/8 < R_G T_m / E_a < 1/35$ range (T_m is the temperature at which the transformation rate is maximum).

Adimensional FK model:

The parameter analysis is greatly simplified by introducing a convenient dimensionless system. FK developed the following dimensionless system:^{54,55}

$$\frac{\partial \theta}{\partial \tau} = \nabla^2 \theta + e^{\frac{\theta}{1+\beta\theta}} f(\alpha) \quad (5)$$

$$\frac{\partial \alpha}{\partial \tau} = \frac{1}{\theta_r} e^{\frac{\theta}{1+\beta\theta}} f(\alpha) \quad (6)$$

$$\left. \frac{\partial \theta}{\partial \chi} \right|_{\chi=0} = 0, \quad \theta(\sqrt{\Lambda}) = \theta_0 \quad (7)$$

The dimensionless temperature ϑ , time τ and space coordinate χ are defined as follows:

$$\theta \equiv \frac{E_A}{R_G T_0^2} (T - T_0) \quad (8)$$

$$\tau \equiv \frac{t}{t_R}, \quad t_R \equiv \left(\frac{q}{c} \frac{E_A}{R_G T_0^2} A e^{-\frac{E_A}{R_G T_0}} \right)^{-1} \quad (9)$$

$$\chi \equiv \frac{x}{x_R}, \quad x_R \equiv \sqrt{\frac{\lambda}{\rho c} t_R} = \sqrt{\frac{\lambda}{\rho q A} \frac{R_G T_0^2}{E_A} e^{\frac{E_A}{R_G T_0}}} \quad (10)$$

where T_0 is the initial temperature of the system, t_R is an induction period of a thermal runaway at T_0 and x_R is a scale of the width of the zone where the reaction rate is significant.

The system behaviour depends on three parameters,

$$\psi \equiv \frac{R_G T_0}{E_A} \quad (11)$$

$$\theta_T \equiv \frac{E_A}{R_G T_0^2} (T_{AD} - T_0) = \frac{E_A}{R_G} \frac{\Delta T_{AD}}{T_{Iso}^2} \quad (12)$$

$$\Lambda \equiv \frac{\rho q}{\lambda} \frac{E_A}{R_G T_0^2} R^2 A e^{-\frac{E_A}{R_G T_0}} = \left(\frac{R}{x_R} \right)^2 \quad (13)$$

ψ is the so called Arrhenius parameter, θ_T is known as the Todes parameter or the Zeldovich number and Λ is the Frank-Kaminetskii parameter. After introducing FK approximations, i.e., $\psi=0$ and $f(\alpha)=1$ so the system can be reduced to:

$$\frac{\partial \theta}{\partial \tau} = \nabla^2 \theta + e^\theta \quad (14)$$

$$\left. \frac{\partial \theta}{\partial \chi} \right|_{\chi=0} = 0, \quad \theta(\sqrt{\Lambda}) = \theta_0 \quad (15)$$

Note that the simplified system depends only on one single parameter, the FK parameter, Λ .

Due to the computational limitations at that time, the numerical integration of partial differential equations presented great difficulties. For this reason, Kaminetskii approached the problem applying the theory of similitude using two different approximate methods: the

stationary and non-stationary approaches. It is noteworthy that both models lead to the formal dependence but allow different issues related to the model to be explored.

On the one hand Kaminetskii assumed that if no combustion front is set, a stationary solution will be reached. Therefore, he deduced the conditions that make combustion possible from determining the conditions under which the stationary model fails.

$$\lambda \nabla^2 T = -\rho q \cdot A e^{-E_A / R_G T} \quad (16)$$

And its dimensionless counterpart is:

$$\nabla^2 \theta = -e^\theta \quad (17)$$

The stationary model reveals a dependence on the geometry of the vessel since the solution depends on a Lagrangian operator. Therefore, a constant value of the Frank-Kaminetskii's parameter, Λ_{cr} , must be found for each particular geometry. Thus, for a given combustible mixture and a given geometry, volumetric combustion could only be controlled by two parameters: the furnace temperature and the vessel size. Kaminetskii solved two one-dimensional (1D) cases: the spherical and the infinitely long cylindrical vessel. He obtained, respectively, $\Lambda_{cr}=3.32$ and $\Lambda_{cr}=2.00$. However, more realistic geometries such as a finite cylinder or a parallelepiped remain unsolved.

On the other hand, the non-stationary approach is based on a similar reasoning: from determining the conditions under which the non-stationary model fails. This model, however, is based on a homogeneous temperature distribution within the sample if combustion does not occur, which is a poor approximation.

$$\rho c \frac{\partial T}{\partial t} = \frac{h \cdot S}{V} (T - T_0) + \rho q \cdot A e^{-E_A / R_G T} \quad (18)$$

Where h is the heat transfer coefficient, S and V are the wall surface area and the volume of the vessel, respectively. The mathematical derivation of the non-stationary model used by Kaminetskii is particularly interesting. A first transformation where only the dimensionless temperature is used leads to:

$$\frac{\partial \theta}{\partial t} = \frac{q}{c} \frac{E_A}{R T_0^2} A e^{-E_A / R_G T_0} e^\theta - \frac{h S}{c \rho V} \theta \quad (19)$$

Each member of Equation 19 has the dimensions of a reciprocal time. Where the following magnitudes could be considered as a yardstick of time:

$$\tau_1 = \left(\frac{q}{c} \frac{E_A}{RT_0^2} A e^{-E_A / RGT_0} \right)^{-1} \quad (20)$$

$$\tau_2 = \left(\frac{hS}{c\rho V} \right)^{-1} \quad (21)$$

Therefore,

$$\frac{\partial \theta}{\partial t} = \frac{e^\theta}{\tau_1} - \frac{\theta}{\tau_2} \quad (22)$$

While τ_1 could be considered as a characteristic reaction time, τ_2 is a characteristic diffusion time. Notice also that $V/S=f(R)$ and τ_2/τ_1 coincides with Λ . By then using τ_1 as the yardstick of time the model parameter dependence is reduced again to a single parameter, which is precisely the Frank-Kaminetskii parameter. In this case, the dependence of the solution on the geometry comes implicitly with the parameter h that accounts for the contribution of diffusion.

From equation 22 it can be deduced that heat diffusion plays a main role in combustion processes, as has been concluded by many other authors.⁵⁶ Only sufficiently slow heat dissipation allows the necessary local sample overheating for a combustion process to take place. Therefore, due to its low thermal conductivity, the setting of a combustion front is further facilitated when samples are in the form of powders. On the other hand, and as we will see in chapter 3, the very small thickness of a thin film makes the onset of a combustion front virtually impossible. The present computational capabilities make it possible to solve the exact system, Eq. 1 and 2, for 1D and 2D systems in a reasonable amount of time. However, it is not an easy task since it is a highly non-linear system and, as we already explained, combustion is controlled by two mechanisms that have very different timescales.

I.3. Modelling of heat transfer

Numerical methods, which all attempt to resolve the value of dependent variables at a finite number of locations in the calculation domain, are commonly used to solve differential equations. These locations are usually called grid points and divide the solution domains into subdomains. There are several discretisation methods that provide an algebraic relation between the dependent variable and the grid points. These relations are derived from the differential equations and try to accurately describe its physical information. Therefore, all possible discretisation equations are expected to give the same solution, which is the solution of the differential equation, provided that the number of grid points is large enough. Since each procedure has its advantages and disadvantages, the procedure used to discretise the solution depends on the particular problem that is being addressed. Furthermore, the solution techniques, which are the path followed to solve the equations, are independent from the discretisation method. For example, and without going into detail, the variational formulation has been commonly employed in finite-element methods (FEM) for stress analysis as it can be easily linked to the virtual-work principle.⁵⁷ However, its applicability is limited because the principle on which it is based cannot be applied to all kinds of differential equations. Another example is the method of weighted residuals, which is very popular in boundary-layer analysis.⁵⁸ The control-volume formulation, which can be understood as a special version of this last one, stands out because the solution exhibits exact integral balances.⁵⁹ In this work, we deal with a numerical method where its discretized equations have been derived using a Taylor-series formulation, i.e. the finite difference method (FDM). The Taylor-series formulation consists of discretising the differential equations as a Taylor series.

The previously mentioned numerical techniques, FEM and FDM, are the two main techniques for solving heat transfer problems. While in the FDM, subdomains are rectangular with a regular grid, in the FEM subdomains may be any polygon shape. Therefore, FDM is more convenient for the discretisation of complicated shape problems. Another important difference is that unlike FDM, the FEM solution provides interpolation functions for each subdomain. However, FDM will be discussed here because it is used more often to solve heat transfer problems in elemental problems since it provides a more accurate solution.⁶⁰ In particular, we will discuss the Taylor-series formulation approach. However, FDM discretization can be also derived from a control-volume approach. There are other

discretisation approaches and numerical techniques that overcome some specific heat transfer problems. For example, the moving particle semi-implicit method (MPS) based on a Lagrangian approach is also used to solve multiple dimension heat transfer problems by applying a semi-implicit prediction-correction process.⁶¹ MPS is an effective numerical method for incompressible in viscid flows with free surfaces. However, discussion of this falls beyond the scope of the present work as here we are concerned with solid state combustion.

In FDM there are two main schemes that are traditionally used depending on whether preference is given to greater accuracy or to the stability of the model. However, in the particular case of the analysis of a combustion process, this dilemma is necessarily avoided. As we will now see, the selection of an implicit scheme is mandatory. Nevertheless, accuracy can be preserved.

We will now describe the numerical approach used to solve the following set of equations developed by Fort et. al. that corresponds to a dimensionless expression of equations 1 and 2 for a cylindrical geometry (Figure I-1):⁶²

$$\frac{\partial \theta}{\partial \tau} = \left(\frac{1}{\zeta} \frac{\partial}{\partial \zeta} \zeta \frac{\partial \theta}{\partial \zeta} + \frac{\partial^2 \theta}{\partial \zeta^2} \right) + \frac{1}{\eta} \frac{\partial \alpha}{\partial \tau} \quad (23)$$

$$\frac{\partial \alpha}{\partial \tau} = \eta e^{-1/\theta} (1 - \alpha) \quad (24)$$

$$\left. \frac{\partial \theta}{\partial \zeta} \right|_{\zeta=0} = 0, \quad \theta(\varepsilon, \zeta) = \theta_f, \quad \left. \frac{\partial \theta}{\partial \zeta} \right|_{\zeta=\delta} = 0, \quad \theta(\zeta, 0) = \theta_f \quad (25)$$

Where the dimensionless temperature ϑ , time τ and space coordinates ζ and ζ , are defined as follows:

$$\theta \equiv T \frac{R_G}{E_A} \quad (26)$$

$$\tau \equiv t \frac{R_G q A}{c E_A} \quad (27)$$

$$\zeta \equiv r \sqrt{\frac{R_G q A \rho}{\lambda E_A}}, \quad \zeta \equiv z \sqrt{\frac{R_G q A \rho}{\lambda E_A}} \quad (28)$$

The dimensionless reciprocal adiabatic temperature rise η is defined as

$$\eta \equiv c \frac{E_A}{R_G q} \quad (29)$$

Notice that unlike the FK approach, this model is not based on an approximation.

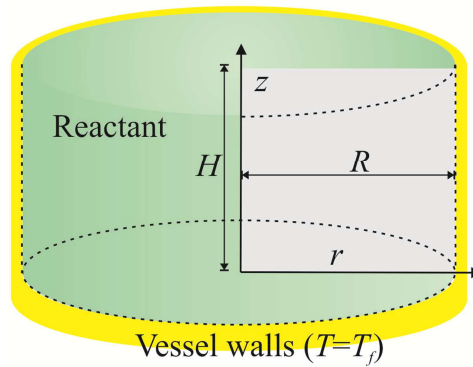


Figure I-1. Geometry analyzed. The sample is placed inside a cylindrical vessel without a cover.

First we describe the 1D models that arise when we neglect one term of the Laplacian. Afterwards we describe the integration of the reaction kinetics. We then describe the 2D model which will be used either for analysing powders or films.

First, we will consider the case of a semi-infinite volume with a flat surface, $H/R \rightarrow 0$ (Fig.1), so we can ignore the partial derivative with respect ζ . The finite differences method is based on the discretisation of space and time:

$$\zeta_i = \zeta_0 + i\Delta\zeta, \quad \tau_n = n\Delta\tau, \quad (30)$$

where $\Delta\zeta$ is the grid spacing and $\Delta\tau$ is the time step used in the discretisation.

The finite difference 1-dimensional explicit scheme of equation 27 is:⁶³

$$\frac{\theta_i^{n+1} - \theta_i^n}{\Delta\tau} = \frac{\theta_{i+1}^n - 2\theta_i^n + \theta_{i-1}^n}{\Delta\zeta^2} + \frac{1}{\eta} \frac{\alpha_i^{n+1} - \alpha_i^n}{\Delta\tau} \quad (31)$$

where $\theta_i^n \equiv \theta(\tau_n, \zeta_i)$, $\alpha_i^n \equiv \alpha(\tau_n, \zeta_i)$, $i = 1, 2, \dots, N-1$ and N is the number of points of the space grid. The method is called explicit because the new value θ_i^{n+1} is given explicitly in terms of the previous value θ_i^n :

$$\theta_i^{n+1} = \frac{\Delta\tau}{\Delta\zeta^2} (\theta_{i+1}^n - 2\theta_i^n + \theta_{i-1}^n) + \frac{1}{\eta} (\alpha_i^{n+1} - \alpha_i^n) + \theta_i^n \quad (32)$$

In 1947, Crank and Nicolson explored several methods of evaluating solutions of the same dimensionless heat transfer equation that we have presented in the previous section (Eq. 5).⁶⁴ That work was the precursor of the Von Neumann stability analysis, which is widely used to evaluate the stability criterion of the explicit scheme of partial differential equations. In the particular case that we are dealing with, they concluded that the numerical method will be unstable if $2\Delta\tau / \Delta\zeta^2 > 1$. Thus, the time step range is limited by the space discretisation. We have previously seen in the derivation of the non-stationary model of Frank-Kaminetskii, however, that combustion deals with two competing mechanisms, heat transfer and reaction evolution, which possess very different time scales. In the case of short characteristic reaction time scales, we are required to use a very short length scale to maintain the stability of the solution with the explicit scheme. A decrease in the space scale strongly increases the computer memory and the time requirements to the point that calculations are very cumbersome or unaffordable in most practical situations. On the other hand, this restriction disappears for the implicit scheme:

$$\frac{\theta_i^{n+1} - \theta_i^n}{\Delta\tau} = \frac{\theta_{i+1}^{n+1} - 2\theta_i^{n+1} + \theta_{i-1}^{n+1}}{\Delta\zeta^2} + \frac{1}{\eta} \frac{\alpha_i^{n+1} - \alpha_i^n}{\Delta\tau} \quad (33)$$

The implicit scheme is always numerically stable but is more numerically intensive. Unlike the explicit scheme, θ_i^{n+1} cannot be directly calculated from the previous value of θ_i^n . Sometimes, the implicit system of equations cannot be solved. For instance, in our case the full implicit method has no analytical solution because of the reaction term. For example, in this work, we ignore the dependence of α_i^{n+1} on θ_i^{n+1} , i.e., the value of α_i^{n+1} is determined from θ_i^n . Under this assumption, Eq. 33 becomes a tridiagonal system that can be solved by using:

$$\theta_i^{n+1} = A_1^i \theta_{i-1}^{n+1} + A_2^i \quad (34)$$

Thus, once we know θ_0^{n+1} , A_1^i and A_2^i , the values of θ_i^{n+1} can be directly calculated from Eq. 34. θ_0^{n+1} is determined from the boundary conditions; $\theta_0^{n+1} = \theta_f$. As for the coefficients A_1^i and A_2^i , substitution of Eq. 34 in Eq. 33 gives,

$$A_1^i = \frac{\gamma}{1 + \gamma(2 - A_1^{i+1})} \quad (35)$$

$$A_2^i = \frac{\gamma A_2^{i+1} + \theta_i^n + (\alpha_i^{n+1} - \alpha_i^n) / \eta}{1 + \gamma(2 - A_1^{i+1})} \quad (36)$$

where $\gamma = \Delta\tau / \Delta\zeta^2$ and the coefficients A_1^{N-1} and A_2^{N-1} are determined from the boundary conditions; from Eqs. 25 and 34 one obtains $A_1^{N-1} = 1$ and $A_2^{N-1} = 0$. To ensure the convergence, the system of equations is solved iteratively using the values of θ_i^{n+1} obtained from the previous iteration to determine α_i^{n+1} . The iterations are stopped when the difference in the values of α_i^{n+1} between two successive iterations are below a certain value which is near to the minimum value of a double precision number.

Note that for the explicit scheme, the stability criterion imposes $\gamma \leq 0.5$. Thanks to the use of the implicit scheme we have been able to use a value of γ as large as 10^{12} . Needless to say that no computer is capable of performing the same calculation using the explicit scheme.

For the case of an infinitely long cylinder, $H/R \rightarrow \infty$, we can neglect the partial derivative with respect ζ and under the implicit scheme, Eq. 23 becomes:

$$\frac{\theta_i^{n+1} - \theta_i^n}{\Delta\tau} = \frac{\left(1 + \frac{1}{2i}\right)\theta_{i+1}^{n+1} - 2\theta_i^{n+1} + \left(1 - \frac{1}{2i}\right)\theta_{i-1}^{n+1}}{\Delta\zeta^2} + \frac{1}{\eta} \frac{\alpha_i^{n+1} - \alpha_i^n}{\Delta\tau} \quad (37)$$

And the coefficients A_1^i and A_2^i become for the radial integration,

$$A_1^i = \frac{\gamma\left(1 - \frac{1}{2i}\right)}{1 + \gamma\left[2 - \left(1 + \frac{1}{2i}\right)A_1^{i+1}\right]} \quad (38)$$

$$A_2^i = \frac{\gamma\left(1 + \frac{1}{2i}\right)A_2^{i+1} + \theta_i^n + (\alpha_i^{n+1} - \alpha_i^n) / \eta}{1 + \gamma\left[2 - \left(1 + \frac{1}{2i}\right)A_1^{i+1}\right]} \quad (39)$$

At a given iteration, the value of α_i^{n+1} is given by Eq. 24. Eq. 24 may be solved by finite differences, but since the time scale of the reaction may be significantly smaller than that of

diffusion, it is very important to determine α_i^{n+1} as accurately as possible to improve the stability of the calculus. So instead of solving Eq. 24 by finite differences, in this work we integrated Eq. 24 analytically; for $\theta_i^{n+1} = \theta_i^n$,⁶⁵

$$\alpha_i^{n+1} = G(\zeta_{iso} + g(\alpha_i^n)) \quad (40)$$

where $g(\alpha) = \int_0^\alpha \frac{dx}{f(x)}$, $\zeta_{iso} = \eta e^{-1/\theta_i^n} \Delta\tau$ and $G(\zeta)$ is the inverse function of $g(\alpha)$. The expression of G and g for a number of reaction models is given by Farjas et al.⁶⁶ For instance, for a first order reaction; $f(\alpha) = 1 - \alpha$, $g(\alpha) = -\ln(1 - \alpha)$, $G(z) = 1 - e^{-z}$ and $\alpha_i^{n+1} = 1 - (1 - \alpha_i^n) \exp[-\eta e^{-1/\theta_i^n} \Delta\tau]$.

For $\theta_i^{n+1} \neq \theta_i^n$, we perform a linear interpolation, i.e., we assume that the temperature increases linearly between θ_i^n and θ_i^{n+1} during the time interval $\Delta\tau$. The integration of 24 gives,⁶⁵

$$\alpha_i^{n+1} = G(z_{li} + g(\alpha_i^n)) \quad (41)$$

where, $z_{li} = \eta \frac{\Delta\tau}{\theta_i^{n+1} - \theta_i^n} [p(1/\theta_i^{n+1}) - p(1/\theta_i^n)]$ and $p(x) \equiv \int_x^\infty \frac{\exp(-u)}{u^2} du$. $p(x)$ has no analytical solution. Since the integration of $p(x)$ would be very time consuming, we use the Padé expansion given in Ref.⁶⁵ that is accurate enough for double precision calculations.

When dealing with multiple dimension problems in FDM, the calculation of the resulting discretisation equations of the Taylor-series formulation has a very high and complicated computing cost. Peaceman and Rachford developed the alternating direction implicit (ADI) method in 1955 as a simple and cost efficient numerical method in terms of computing power.⁶⁷ The method belongs to the operator splitting method family, which means that the differencing scheme for a given variable is split into a sum of pieces. Each of these pieces is calculated independently. The addition of their results gives the solution of the primitive differential scheme. In the particular case of a 2 dimensional case this approach consists of splitting the integration into two time steps $\Delta\tau/2$ where one of the directions is calculated implicitly and the other explicitly.⁶³ Therefore, the pure conductive heat transfer discrete equation with heat generation is then rewritten as follows:

For the first step the finite differences equation is,

$$\frac{\theta_{i,j}^{n+1} - \theta_{i,j}^n}{\Delta \tau / 2} = \frac{\left(1 + \frac{1}{2i}\right)\theta_{i+1,j}^{n+1} - 2\theta_{i,j}^{n+1} + \left(1 - \frac{1}{2i}\right)\theta_{i-1,j}^{n+1}}{\Delta \zeta^2} + \frac{\theta_{i,j+1}^n - 2\theta_{i,j}^n + \theta_{i,j-1}^n}{\Delta \zeta^2} + \frac{1}{\eta} \frac{\alpha_{i,j}^{n+1} - \alpha_i^n}{\Delta \tau / 2} \quad (42)$$

where $\theta_{i,j}^n \equiv \theta(\tau_n, \zeta_i, z_j)$, $\alpha_i^n \equiv \alpha(\tau_n, \zeta_i, \zeta_j)$, $i = 1, 2, \dots, N_r - 1$, $j = 1, 2, \dots, N_z - 1$, and N_r and N_z are the number of points of the radial and axial grids, respectively.

And the coefficients A_1^i and A_2^i become for the radial implicit integration,

$$A_1^i = \frac{\frac{\gamma}{2} \left(1 - \frac{1}{2i}\right)}{1 + \frac{\gamma}{2} \left[2 - \left(1 + \frac{1}{2i}\right)A_1^{i+1}\right]} \quad (43)$$

$$A_2^i = \frac{\frac{\gamma}{2} \left(1 + \frac{1}{2i}\right)A_2^{i+1} + \frac{\gamma}{2} (\theta_{i,j+1}^n - 2\theta_{i,j}^n + \theta_{i,j-1}^n) + \theta_{i,j}^n + (\alpha_i^{n+1} - \alpha_i^n) / \eta}{1 + \frac{\gamma}{2} \left[2 - \left(1 + \frac{1}{2i}\right)A_1^{i+1}\right]} \quad (44)$$

For the second step the finite differences equation is,

$$\frac{\theta_{i,j}^{n+1} - \theta_{i,j}^n}{\Delta \tau / 2} = \frac{\left(1 + \frac{1}{2i}\right)\theta_{i+1,j}^{n+1} - 2\theta_{i,j}^{n+1} + \left(1 - \frac{1}{2i}\right)\theta_{i-1,j}^{n+1}}{\Delta \zeta^2} + \frac{\theta_{i,j+1}^{n+1} - 2\theta_{i,j}^{n+1} + \theta_{i,j-1}^{n+1}}{\Delta \zeta^2} + \frac{1}{\eta} \frac{\alpha_{i,j}^{n+1} - \alpha_i^n}{\Delta \tau / 2} \quad (45)$$

And the coefficients A_1^i and A_2^i become for the axial implicit integration,

$$A_1^i = \frac{\frac{\gamma}{2}}{1 + \frac{\gamma}{2} \left[2 - A_1^{i+1}\right]} \quad (46)$$

$$A_2^i = \frac{\frac{\gamma}{2} \left(1 + \frac{1}{2i}\right)A_2^{i+1} + \frac{\gamma}{2} \left[\left(1 + \frac{1}{2i}\right)\theta_{i+1,j}^n - 2\theta_{i,j}^n + \left(1 - \frac{1}{2i}\right)\theta_{i-1,j}^n\right] + \theta_{i,j}^n + (\alpha_i^{n+1} - \alpha_i^n) / \eta}{1 + \frac{\gamma}{2} \left[2 - A_1^{i+1}\right]} \quad (47)$$

Finally, we would like to mention that it has traditionally been difficult to obtain a good spatial accuracy in ADI methods when dealing with interface problems. For example, when a crucible or a substrate is taken into account. Although it is not going to be discussed here, Zaho recently developed a new ADI method for solving 2-dimension heat equations with interfaces.⁶⁸ This method maintains a good computational efficiency and, most importantly, unconditional stability. For our part, we will analyse in this work the effect of an interface

between sample and substrate or a crucible (depending on whether we are analysing films or powders) where thermal parameters change in a one dimensional problem. We impose the continuity of heat flow in the interface but the element of the grid at the interface also has a certain volume. We assume that half of this volume belongs to the sample, so heat is generated due to the reaction; and that the heat capacity is different at both sides of the interface. Therefore, the finite differences equation at the interface is,

$$\frac{\theta_i^{n+1} - \theta_i^n}{\Delta \tau} = \frac{\delta(\theta_{i+1}^n - \theta_i^n)}{\Delta \zeta^2} + \frac{\delta \lambda_s / \lambda (\theta_i^n - \theta_{i-1}^n)}{\Delta \zeta^2} + \frac{1}{2} \frac{\delta}{\eta} \frac{\alpha_i^{n+1} - \alpha_i^n}{\Delta \tau} \quad (48)$$

And the coefficients A_1^l and A_2^l become,

$$A_1^l = \frac{\gamma \delta}{1 + \gamma \delta \left[1 + \frac{\lambda_s}{\lambda} - \frac{\lambda_s}{\lambda} A_1^{l+1} \right]} \quad (49)$$

$$A_2^l = \frac{\gamma \delta \frac{\lambda_s}{\lambda} A_2^{l+1} + \theta_i^n + \delta(\alpha_i^{n+1} - \alpha_i^n) / (2\eta)}{1 + \gamma \delta \left[1 + \frac{\lambda_s}{\lambda} - \frac{\lambda_s}{\lambda} A_1^{l+1} \right]} \quad (50)$$

where l stands for the index of the element of the grid that is located at the interface, λ and λ_s ,

are the sample and substrate conductivities respectively, $\delta \equiv \frac{2}{1 + \frac{\lambda_s}{\lambda a_s}}$, and a_s is the

substrate diffusivity (note that the dimensionless diffusivity of the sample is 1).

I.4. Thermal Analysis

Thermal analysis (TA) is a set of techniques that are especially suited to analysing the transformations that take place when a sample is submitted to a controlled temperature program. It is particularly convenient for the study of thermal transformations and, more specifically, combustion processes. TA provides us with valuable information to determine some reaction and sample key parameters such as the enthalpy of the reaction, the kinetic parameters, the sample heat capacity and its thermal conductivity. In addition, TA allows us to monitor the evolution of sample with the temperature under controlled atmosphere.

Information may be enhanced if different techniques are applied simultaneously, commonly known as simultaneous thermal analysis (STA). In particular, we will highlight in this section differential thermal analysis (DTA), thermogravimetry (TG) and differential scanning calorimetry (DSC) since they are the main TA techniques that we have deal with in this work. Additionally we will refer to, although to a lesser extent, evolved gas analysis (EGA).TA has a long history over the last century and, at present, it is still evolving. In order to obtain a global vision of each technique we will introduce them in the chronological order in which they were developed.

The first TA technique that was invented was DTA, which provides qualitative information of exothermic and endothermic processes by measuring the temperature difference between a sample and an inert reference. For example, it is useful to analyse decompositions, evaporations, crystallisations and melting processes. Its history starts in 1887, when Le Chatelier carried out the first DTA experiments.⁶⁹ However, what we know today as DTA was not in fact developed until 1899 with the introduction of reference materials. A typical DTA signal for a polymer is depicted in Figure I-2.

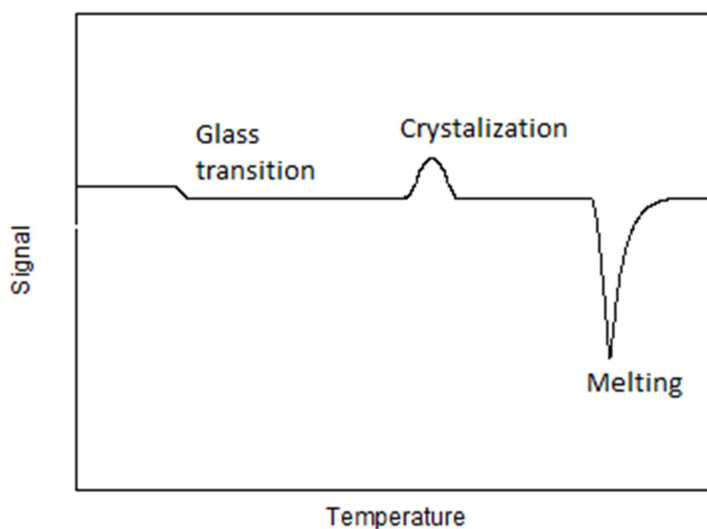


Figure I-2. Typical DSC signal for a polymer.

The second thermal analysis technique appeared, thermogravimetry, appeared in 1915. This is the measurement of mass changes under a specific thermal treatment. The operating principle is simple: a sample is placed inside a furnace and its mass is constantly measured and recorded by means of a microbalance. Thus, every process involving mass changes can be monitored.

This includes either physical phenomena, for example vaporisation or sublimation processes, or chemical phenomena such as decompositions or solid-gas reactions.⁷⁰⁻⁷² Only 10 years later, in 1925, a TG apparatus was used to analyse reaction kinetics for the very first time. Nevertheless, it would be 30 years before TG stood out as a remarkable technique in the field of solid phase transformation kinetics. Freeman and Carroll took advantage of the potential of TG for kinetic purposes in order to study thermal decompositions.⁷³ A common TG curve of the decomposition of a metal-organic precursor is shown in Figure I-3.

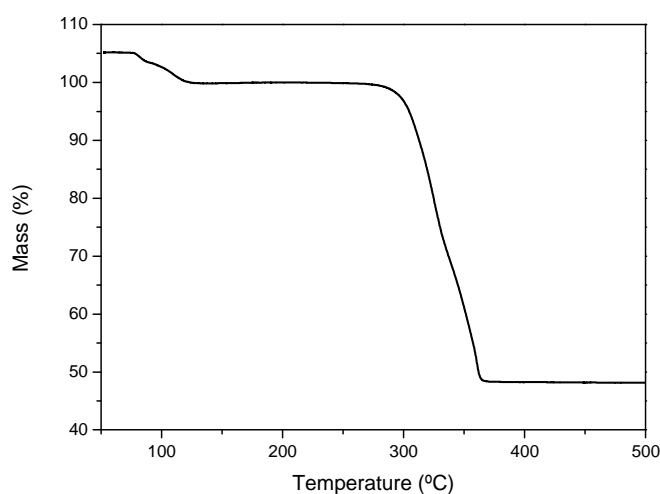


Figure I-3. Common TG curve of the decomposition of a metal-organic precursor.

Since 1960, it has been possible to perform precise quantitative measurements in DTA experiments. For this purpose, the structure of the conventional DTA apparatus has been modified. For instance, it allows the heat capacity of samples to be measured accurately. This improved version of the DTA is known as the heat-flux differential scanning calorimeter (hf-DSC) or quantitative DTA and nowadays is probably the most widely-spread TA apparatus. At approximately the same time, power compensation DSC (pc-DSC) was being developed. Although, both DSC techniques implicitly provide the same information, the way this information is obtained differs substantially. On the one hand, a small thermal resistance connects sample and reference in the hf-DSC and what is measured is the temperature difference between both, which is directly linked to the heat flow between sample and reference. According to the DSC relationship,

$$DSCsignal = \dot{Q} = \frac{T_S - T_{ref}}{R} \quad (51)$$

where \dot{Q} is the heat flow between the sample and the reference, R is the thermal resistance between sample and reference, T_S is the sample temperature and T_{ref} is the temperature of the inert reference.

On the other hand, in a pc-DSC, the sample and reference are located in identical but separate furnaces. A pc-DSC measures the difference in the power supplied to the furnaces to keep the sample and the reference at the same temperature. Both types of DSC can be compared in Figure I-4.

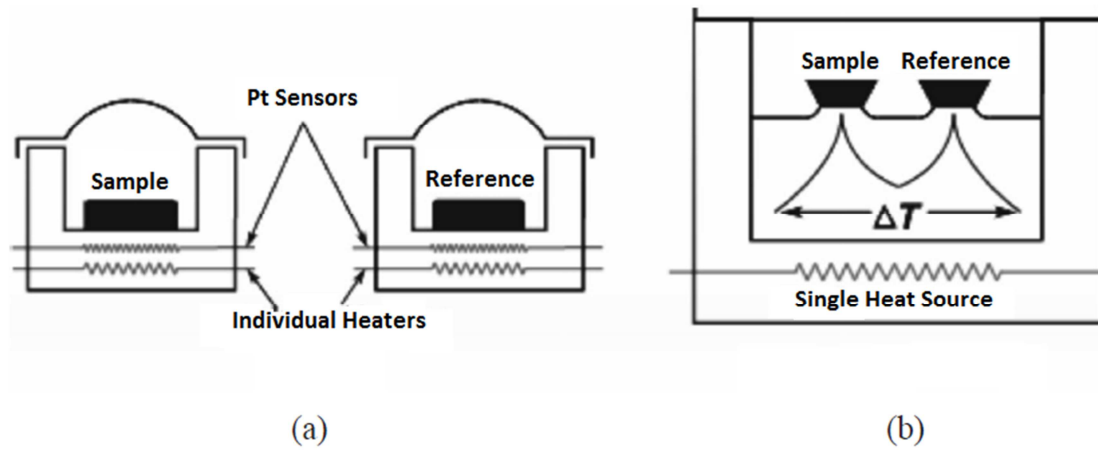


Figure I-4. (a) power-compensation DSC; (a) Heat flux DSC. From Differential thermal analysis (DTA) and differential scanning calorimetry (DSC) as a method of material investigation, by G. Klancnik et al., Materials and Geoenvironment, Vol. 57, No. 1, pp. 127–142, 2010.

Thermal analysis is used in many and diverse fields concerning the study of all kinds of thermal processes. Among these, we would particularly like to point to the synthesis of materials through chemical methods due to its importance in this work.^{74–77} More specifically, it is important in the context of the present work to emphasise the common use of TA to investigate the thermal decomposition of precursors used in CS techniques such as SCS or SHS.^{78–83} Besides, combustion has been broadly analysed by TA techniques in a more generic way in order to understand the mechanisms that rule the process. For example, numerous TA studies have been carried out to investigate the susceptibility of coal to spontaneous heating.⁸⁴

In particular, the ignition point temperature has been extensively characterised by DTA, TG and DSC.

Despite its long history, thermal analysis still has an important role in responding to the needs and challenges that scientific evolution raise. For example, despite the current importance of thin films, appropriate thermal analysis techniques have not been completely developed yet. Thin film properties cannot be generally extrapolated from bulk samples due to their very different geometries. However, this has been usually by-passed and ignored.⁸⁵ The reason for this is that TA equipment is not designed to hold samples in the form of thin films and, more importantly, because the signal is usually proportional to the sample mass, and sample masses in thin films are typically one order of magnitude smaller than samples in the form of powders.

On another subject, quantitative measurements in thermal analysis experiments are based on the assumption that the temperature distribution within a sample is homogenous. This is not a realistic assumption when dealing with low thermal conductivity materials and high sample masses. Furthermore, it is especially incorrect in the case of combustion processes since the reaction is not homogeneous but is confined to a combustion front. Therefore, it would be very interesting to study the temperature gradients within a sample in order to establish a criterion to prevent inaccuracies in TA experiments as well as to better understand combustion processes.

I.4.1. Specific heat Capacity

Under ideal conditions, when an inert sample is heated at a constant heating rate the heat flow measured by a conventional DSC is proportional to the sample heat capacity and to the heating rate:

$$\dot{Q} = c_p \cdot m \cdot \beta \quad (52)$$

Where, c_p is the sample specific heat capacity, m is the sample mass and β is the heating rate.

There are two main procedures to calculate the specific heat capacity based on this definition, i.e. the direct and the steady state methods. The direct method simply relies on applying the abovementioned definition. That is, it is based on measuring c_p from a sample that is heated at a constant heating rate. A more sophisticated version of the direct approach is the so-called

enthalpic method which calculates an average heat capacity.⁸⁶ First, a temperature interval is chosen and the entire area under the DSC curve is determined. Therefore, an average heat capacity is obtained from the quotient between the area and the temperature span.

$$\overline{c_p} = \frac{\int_{T_1}^{T_2} \dot{Q} \cdot dT}{m \cdot \Delta T} \quad (53)$$

With regard to the steady state method, c_p is calculated from the shift experienced by the signal once β changes abruptly from a finite value to zero or from zero to a finite value, i.e., when changing from a constant temperature increase rate program to an isotherm program or vice versa. Both methods require the correction of the signal using a baseline that, ideally, must be measured under identical experimental conditions.

Alternatively, c_p can be measured by a modulated DSC, which is essentially the same apparatus except that it uses a sinusoidal modulation of the temperature rate. In this particular case:

$$T = T_0 + \beta t + A_T \sin \omega t \quad (54)$$

Where, A_T is the amplitude of the modulation.

Rewriting equation 52 as:

$$\dot{Q} = c_p \cdot m \cdot \frac{dT}{dt} \quad (55)$$

And, combining equations 52 and 54:

$$\dot{Q} = c_p m (\beta + A_T \omega \cos \omega t) \quad (56)$$

Therefore, the amplitude of the modulated heat flow signal is:

$$A_{HF} = m \cdot c_p \cdot \omega \cdot A_T \quad (57)$$

The main advantage of the modulated method is that c_p is obtained as a continuous function of temperature. Figure I-5 shows a comparison of the methods used to measure c_p :

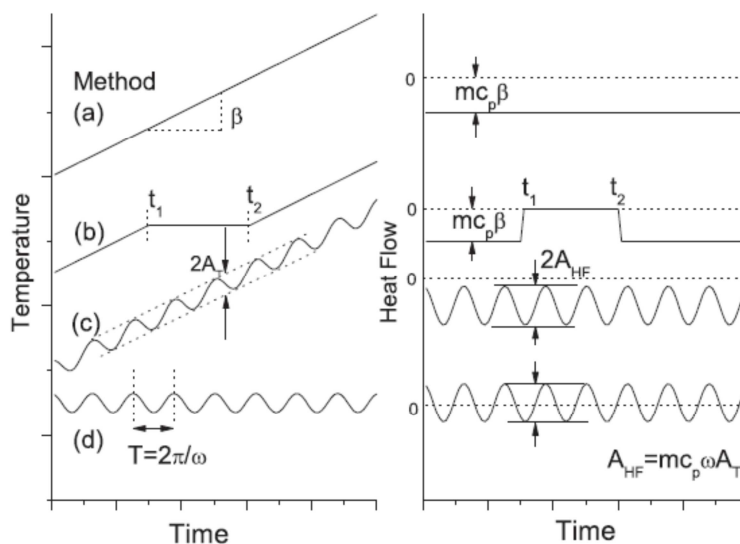


Figure I-5. The four methods for measuring c_p with a conventional DSC (a and b) and modulated DSC (c and d) that we have mentioned above. From Measurement by differential scanning calorimetry of specific heat capacity variation due to crystallization: Application to amorphous silicon by P. Roura et al., *Thermochimica Acta*, Vol. 522, pp. 161–165, 2010.

I.4.2. Thermal conductivity

Although thermal conductivity (λ) is usually measured using specific apparatus especially designed for that purpose, there are several methods that provide alternative methods of doing it using a DSC. This is particularly convenient since the DSC is widely available and, in contrast to many traditional methods, only requires a small amount of sample. However, all DSC methods are only suitable for low conductivity samples. None of them, though, could be applied to uncompressed powders, which is probably the most used geometry in thermal analysis of solid state reactions.

The first methods developed were based on modifying conventional heat flux DSCs in order to find out the temperature on both sides of the sample. To that end, an additional temperature sensor was incorporated.^{87–89} In so doing, λ calculation is straightforward using the equation:

$$\frac{dQ}{dt} = -\lambda \cdot A \cdot \frac{dT}{dx} \quad (58)$$

Where A is the sample cross sectional area.

At present, two main approaches exist that do not require any apparatus modification. On the one hand, there are methods using a commercial Modulated DSC.^{90–92} These methods

determine λ from the ratio of apparent and true heat capacities measured for a sample in the form of a disk. The first method was developed by Marcus and Blaine.⁹⁰ According to their approach, the modulated heat flow generated by a MDSC Equation 58 can be expanded as:

$$\left(\frac{dQ}{dt}\right)^2 = 2(Z\lambda AT_0)^2 \cdot \frac{[1 - 2e^{2ZL} \cos 2ZL + e^{4ZL}]}{[1 + 2e^{2ZL} \cos 2ZL + e^{4ZL}]} \quad (59)$$

Where:

$$Z^2 = \omega \rho c_p / 2 \quad (60)$$

The e^{4ZL} term is significantly larger for materials of low thermal conductivity. In this case,

$$\frac{[1 - 2e^{2ZL} \cos 2ZL + e^{4ZL}]}{[1 + 2e^{2ZL} \cos 2ZL + e^{4ZL}]} \approx 1 \quad (61)$$

Then, assuming a cylindrical geometry

$$\lambda = \frac{8LC^2}{c_p m d^2 P} \quad (62)$$

Where L, d and m are the length, diameter and mass of the sample, respectively. The period, P, and the apparent heat capacity, C, are calculated as follows:

$$C = \frac{dQ/dt}{\omega \cdot T_0} \quad (63)$$

$$P = \frac{2\omega}{\omega} \quad (64)$$

Simon and McKenna detected two problems.⁹¹ The approximation used in the derivation, Eq. 58, significantly limits the thermal conductivity range. In addition, thermal resistance between the sample and the furnace has a significant effect that is not taken into account.

Later, Merzlyakov and Schick⁹² developed a new method based on the same principle. Their approach assumes that the thermal contact and the thermal conductivity led to different frequency dependencies of apparent heat capacity. They needed to determine two parameters in order to calculate λ : specific heat capacity and effective thermal contact between the sample and the furnace. Their model is described by the following 3 equations:

$$C_{app}(\omega) = \frac{C_p + C_\beta(\omega)}{1 - (i\omega / K_{op}) \cdot (C_p + C_\beta(\omega))} \quad (65)$$

Where C_p is the heat capacity of the pan.

The apparent heat capacity directly measured at the surface of the sample pan is given by:

$$C_\beta(\omega) = \frac{C_\alpha(\omega)}{1 - (i\omega / K_{op}) \cdot C_\alpha(\omega)} \quad (66)$$

And the apparent heat capacity directly measured at the surface of the sample is given by:

$$C_\alpha(\omega) = -\frac{1}{i\omega} \lambda S \alpha \tanh(\alpha d) \quad (67)$$

Where,

$$\alpha = \sqrt{\omega / |\chi|} e^{(i/2)\arg(-i(\omega/\chi))} \quad (68)$$

And,

$$\chi = \lambda / \rho c_p \quad (69)$$

Alternatively, Hakvoort⁹³ developed a method to determine λ with a non-modified conventional DSC⁹³. This method was improved by Flynn and Levin first and Camirand thereafter.^{94,95} Their method is based on the measurement of the melting slope of a reference metal which is located on the top of a solid flat sample. The slope corresponds to the reciprocal of all the thermal resistances located under the reference metal:

$$s = \frac{1}{R} \quad (70)$$

And we can split R as follows:

$$R = R_1 + R_2 + R_s \quad (71)$$

Where R_1 is the thermal contact resistance between the sample and the sample furnace, R_2 the thermal contact resistance between the sample and the reference metal and R_s the thermal resistance of the sample.

$$R_s = \frac{L_s}{\lambda_s A_s} \quad (72)$$

Where L_s , λ_s , A_s are, respectively, the height, thermal conductivity and the area of the horizontal cross-section of the sample.

The introduction of R_2 into the model was the main contribution of Flynn and Levin since Hakvoort did not take this into account. For his part, Camirand slightly modified the procedure. At first λ was calculated performing only a second DSC curve where the reference metal is melted with the same settings of the first experiment but without sample. Sample thermal resistance and, consequently, its thermal conductivity were deduced from the difference between the slopes. By contrast, Camirand's method is as follows; different DSC curves are recorded where the reference metal is melted using the same setting but changing the sample height. Then, λ_s is the inverse of the slope when plotting the total thermal resistance of the experiments against $\frac{L_s}{A_s}$. Notice that it is assumed that thermal contact resistance does not change when changing the sample.

In chapter 5 we introduce an alternative method which allowed us to determine thermal conductivity of powders with a high degree of accuracy.

I.4.3. Kinetic parameters

Reaction kinetics deals with the measurement and parameterization of process rates. In this work we will exclusively deal with parameterization of single-step reaction kinetic which is usually described by the following equation if the dependence on the pressure is avoided:

$$\frac{d\alpha}{dt} = k(T)f(\alpha) \quad (73)$$

where $k(T)$ and $f(\alpha)$ represent the dependence of the process on the temperature and on the extent of conversion respectively.

The extent of conversion increases from 0 to 1 and is determined experimentally using physical properties that evolve with the process. Since we are devoted to the study of decomposition processes, which involve mass loss and the release of heat, the extent of conversion could be

either evaluated as a fraction of the total mass loss or as a fraction of the total heat released during the process.

For thermally activated processes, temperature dependence of a reaction is usually described by the Arrhenius equation:

$$k(T) = Ae^{-E_A/R_G T} \quad (74)$$

Where, R is the gas constant and E_a is the activation energy of the thermal barrier and the preexponential term A is the occurrence frequency factor.

For its part, there are several reaction models that try to describe the extent of conversion dependency for different mechanisms. However, we are not going to discuss them since, as we shall see, the model-free methods we will deal with for determining the kinetic parameters, i.e. the method of Kissinger and the isoconversional methods, do not, as their name suggests, need to assume any particular form of the reaction model. In addition, we will only discuss methods that belong to the group that use multiple temperature programs which are strongly recommended instead of using single temperature programs.⁹⁶

- The Kissinger method is derived from the condition that at the maximum reaction rate $d^2\alpha/dt^2 = 0$.

Therefore, assuming the Arrhenius temperature dependence and an independency of the conversion extend dependency of the heating rate, the following equation is obtained:

$$\frac{E_A}{RT_m^2} = \frac{A}{\beta} e^{-E_A/R_G T_m} \quad (75)$$

T_m is the temperature at which the transformation rate is at its maximum.

After a few arrangements we obtain the so called Kissinger equation:

$$\ln\left(\frac{\beta}{T_m^2}\right) = \ln\left(-\frac{AR}{E_A}\right) - \frac{E_A}{R_G T_m} \quad (76)$$

The assumption of the independency of the heating rate is, as will be shown in this work, extremely inconvenient for the analysis of samples that suffer overheating, as is the case in combustion processes.

In the Kissinger method, $\ln\left(\frac{\beta}{T_m^2}\right)$ is plotted against $\frac{1}{T_m}$. The slope of the resulting linear dependence is the activation energy.

To deal with kinetics that are more complex than single-step reactions, isoconversional methods have been developed that are based on the isoconversional principle, which is a generalization of Eq.74. According to the isoconversional principle, at a constant degree of transformation, the reaction rate is only a function of temperature and no assumption on the a reaction model must be made.⁹⁷

$$\left[\frac{d \ln(d\alpha / dt)}{dT^{-1}} \right]_{\alpha} = -\frac{E_{\alpha}}{R} \quad (77)$$

where E_{α} is the activation energy for this degree of transformation. Integration of Eq. 1 results in single-step transformations where the activation energy, E_{α} , and pre-exponential factor, A_{α} , depend on the degree of transformation:

$$\frac{d\alpha}{dt} = A_{\alpha} e^{-\frac{E_{\alpha}}{RT}} f(\alpha) \quad (78)$$

We can distinguish between two types of isoconversional methods: differential and integral ones.

- Differential isoconversional methods are based on the following equation which is easily derived from applying the isoconversional principle to Eq. 73. Friedman's⁹⁸ is, probably, the most widely used.

$$\ln\left(\frac{d\alpha}{dt}\right)_{\alpha,i} = \ln[f(\alpha)A_{\alpha}] - \frac{E_{a_{\alpha}}}{R_G T_{\alpha,i}} \quad (79)$$

Where the index α denotes a given degree of transformation and index i identifies each of the experiments. For multiple heating rate experiments Eq. 79 is usually presented as:

$$\ln \left[\beta_i \left(\frac{d\alpha}{dt} \right)_{\alpha,i} \right] = \ln [f(\alpha)A_\alpha] - \frac{E_{a_\alpha}}{R_G T_{\alpha,i}} \quad (80)$$

E_a is obtained at any given degree of transformation from the slope that results from plotting the left term of the equation against $1/T_i$. A is determined from the independent term of the resulting linear dependence.

- Integral isoconversional methods are based on the integral form of Eq. 73:

$$g(\alpha) \equiv \int_0^\alpha \frac{d\alpha}{f(\alpha)} = A \int_0^t e^{\left(\frac{-E_a}{R_G T} \right) dt} \quad (81)$$

An analytical solution can be obtained for isothermal experiments:

$$\ln t_{\alpha,i} = \ln \left[\frac{g(\alpha)}{A_\alpha} \right] + \frac{E_\alpha}{RT_i} \quad (82)$$

On the contrary, no analytical solution can be obtained from the non-isothermal expression of the Eq. 73:

$$\int_0^\alpha \frac{d\alpha}{f(\alpha)} = \frac{A}{\beta} \int_0^t e^{\left(\frac{-E_a}{R_G T} \right) dT} \quad (83)$$

However, there are some approximations of the general form:

$$\ln \left(\frac{\beta}{T_{\alpha,i}^B} \right) = Const - C \frac{E_A}{R_G T_{\alpha,i}} \quad (84)$$

Where B and C are parameters determined for each specific approximation. In Table I-1 we show three of the most popular approximations and the names of the researchers who proposed them. They are ordered from top to bottom from the crudest to the most accurate one.

Table I-1. B and C parameters for different approximations based on Eq. 84.

	B	C
Doyle	0	1.052
Murray and White(Kissinger-Akahira-Sunose)^{99*}	2	1
Starink	1.92	1.008

*Based on the Kissinger equation

E_A can be calculated as the plot slope of representing the left term of the equation vs $\frac{1}{T_i}$ or

$\frac{1}{T_{\alpha,i}}$ depending on the type of experiment, i.e. isothermal or non-isothermal.

I.5. References

1. Ramesh, R. & Schlom, D. G. Whither Oxide Electronics? *MRS Bull.* **33**, 1006–1014 (2008).
2. Chambers, S. A. & Yoo, Y. K. New Materials for Spintronics. *MRS Bull.* **28**, 706–710 (2003).
3. Paranthaman, M. P. & Izumi, T. High-Performance YBCO-Coated Superconductor Wires. *MRS Bull.* **29**, 533–541 (2004).
4. Schwartz, R. W., Schneller, T. & Waser, R. Chemical solution deposition of electronic oxide films. *Comptes Rendus Chim.* **7**, 433–461 (2004).
5. Morsi, K. The diversity of combustion synthesis processing: a review. *J. Mater. Sci.* **47**, 68–92 (2012).
6. Kim, M.-G., Kanatzidis, M. G., Facchetti, A. & Marks, T. J. Low-temperature fabrication of high-performance metal oxide thin-film electronics via combustion processing. *Nat Mater* **10**, 382–388 (2011).
7. Everaerts, K. *et al.* Printed Indium Gallium Zinc Oxide Transistors. Self-Assembled Nanodielectric Effects on Low-Temperature Combustion Growth and Carrier Mobility. *ACS Appl. Mater. Interfaces* **5**, 11884–11893 (2013).

8. Branquinho, R. *et al.* Aqueous Combustion Synthesis of Aluminum Oxide Thin Films and Application as Gate Dielectric in GZTO Solution-Based TFTs. *ACS Appl. Mater. Interfaces* **6**, 19592–19599 (2014).
9. Wen, W. & Wu, J.-M. Nanomaterials via solution combustion synthesis: a step nearer to controllability. *RSC Adv.* **4**, 58090–58100 (2014).
10. Varma, A., Rogachev, A. S., Mukasyan, A. S. & Hwang, S. Combustion Synthesis of Advanced Materials: Principles and Applications. *Adv. Chem. Eng.* **24**, 79–226 (1998).
11. Patil, K. C., Aruna, S. T. & Mimani, T. Combustion synthesis: An update. *Curr. Opin. Solid State Mater. Sci.* **6**, 507–512 (2002).
12. Chandler, C. D., Roger, C. & Hampden-Smith, M. J. Chemical aspects of solution routes to perovskite-phase mixed-metal oxides from metal-organic precursors. *Chem. Rev.* **93**, 1205–1241 (1993).
13. Derby, B. Inkjet Printing of Functional and Structural Materials: Fluid Property Requirements, Feature Stability, and Resolution. *Annu. Rev. Mater. Res.* **40**, 395–414 (2010).
14. HEINZL, J. & HERTZ, C. H. INK-JET PRINTING. *Adv. IMAGING ELECTRON Phys.* **65**, 91–171 (1985).
15. Vilardell, M. *et al.* Flexible manufacturing of functional ceramic coatings by inkjet printing. *Thin Solid Films* **548**, 489–497 (2013).
16. Wijshoff, H. The dynamics of the piezo inkjet printhead operation. *Phys. Rep.* **491**, 77–177 (2010).
17. Kunshina, G. B., Bocharova, I. V. & Lokshin, E. P. Synthesis and ionic conductivity of lithium-ion-conducting Li_{0.5}La_{0.5}TiO₃ oxide ceramics. *Inorg. Mater.* **51**, 369–374 (2015).
18. Răileanu, M. *et al.* Sol-gel zirconia-based nanopowders with potential applications for sensors. *Ceram. Int.* **41**, 4381–4390 (2015).
19. Shao, G. N., Engole, M., Imran, S. M., Jeon, S. J. & Kim, H. T. Sol-gel synthesis of photoactive kaolinite-titania: Effect of the preparation method and their photocatalytic properties. *Appl. Surf. Sci.* **331**, 98–107 (2015).
20. Shen, Y. & Lua, A. C. Sol-gel synthesis of titanium oxide supported nickel catalysts for hydrogen and carbon production by methane decomposition. *J. Power Sources* **280**, 467–475 (2015).
21. Mashreghi, a. & Davoudi, F. The effect of ethylene glycol/citric acid molar ratio in the initial precursor of TiO₂ nanoparticle paste synthesized by a polymerizable complex method on the photovoltaic properties of dye-sensitized solar cells. *Mater. Sci. Semicond. Process.* **30**, 618–624 (2015).

22. Vargas-Becerril, N., Téllez-Jurado, L., Reyes-Gasga, J., Alvarez-Perez, M. a. & Rodríguez-Lorenzo, L. M. Synthesis of nanosized carbonated apatite by a modified Pechini method: hydroxyapatite nucleation from a polymeric matrix. *J. Sol-Gel Sci. Technol.* **72**, 571–580 (2014).
23. Gonzlez Martinez, J. M., Munoz Meneses, R. A. & da Silva, C. R. Synthesis of Gadolinium Doped Ceria Ceramic Powder by Polymeric Precursor Method (Pechini). in *BRAZILIAN CERAMIC CONFERENCE 57* (ed. Castanho, SM and Acchar, W and Hotza, D) **798-799**, 182–188 (TRANS TECH PUBLICATIONS LTD, 2014).
24. Cao, Y., Zhu, K., Qiu, J., Pang, X. & Ji, H. Sol-gel processing and characterization of potassium niobate nano-powders by an EDTA/citrate complexing method. *Solid State Sci.* **14**, 655–660 (2012).
25. Cao, Y., Zhu, K., Zheng, H., Qiu, J. & Gu, H. Synthesis of potassium sodium niobate powders using an EDTA/citrate complexing sol-gel method. *Particuology* **10**, 777–782 (2012).
26. Ousi-Benommar, W. *et al.* Structural and optical characterization of BaTiO₃ thin films prepared by metal-organic deposition from barium 2-ethylhexanoate and titanium dimethoxy dineodecanoate. *J. Mater. Res.* **9**, 970–979 (1994).
27. Xue, S., Ousi-Benommar, W. & Lessard, R. A. α -Fe₂O₃ thin films prepared by metalorganic deposition (MOD) from Fe(III) 2-ethylhexanoate. *Thin Solid Films* **250**, 194–201 (1994).
28. Zhu, W., Liu, Z. Q., Tse, M. S. & Tan, H. S. Raman, FT-IR and dielectric studies of PZT 40/60 films deposited by MOD technology. *J. Mater. Sci. Mater. Electron.* **6**, 369–374 (1995).
29. Sathyamurthy, S. & Salama, K. Application of metal–organic decomposition techniques for the deposition of buffer layers and {Y123} for coated-conductor fabrication. *Phys. C Supercond.* **329**, 58–68 (2000).
30. Zhou, Y. X. *et al.* Strontium titanate buffer layers deposited on rolled Ni substrates with metal organic deposition. *Supercond. Sci. Technol.* **16**, 901 (2003).
31. Chakraborty, A., Sanfui, B. K. & Parya, T. K. Densification characteristics of ZrO₂ doped pure Al₂O₃ ceramics synthesized through co-precipitation route. *J. INDIAN Chem. Soc.* **90**, 963–972 (2013).
32. Gu, Y. *et al.* The thermodynamic analysis of Ni_{1/2}Mn_{1/2}(OH)₂ prepared by hydroxide co-precipitation method. in *ADVANCED RESEARCH ON BIOCHEMICAL MATERIALS AND NANOTECHNOLOGY APPLICATION* (ed. Zhang, H and Jin, D and Zhao, XJ) **643**, 104–107 (TRANS TECH PUBLICATIONS LTD, 2013).

33. Shameli, K. *et al.* SYNTHESIS OF NICKEL DOPED COBALT FERRITE IN PRESENCE OF SDS WITH DIFFERENT HEAT TREATMENT BY CO-PRECIPIATION METHOD. *Dig. J. Nanomater. BIOSTRUCTURES* **8**, 981–985 (2013).
34. Parya, T. K., Bhattacharyya, R. K., Banerjee, S. & Adhikari, U. B. Co-precipitated ZnAl₂O₄ spinel precursor as potential sintering aid for pure alumina system. *Ceram. Int.* **36**, 1211–1215 (2010).
35. Liang, L., Hu, G., Cao, Y., Du, K. & Peng, Z. Synthesis and characterization of full concentration-gradient LiNi_{0.7}Co_{0.1}Mn_{0.2}O₂ cathode material for lithium-ion batteries. *J. Alloys Compd.* **635**, 92–100 (2015).
36. Zhang, Y. *et al.* Synthesis, structure and optical properties of polycrystalline Cr,Nd:GSAG powders by a co-precipitation method. *J. Alloys Compd.* **617**, 58–62 (2014).
37. Fangming, Z. *et al.* Preparation of Nd:YAG Nanopowders by the urea co-precipitation. in *SENSORS, MECHATRONICS AND AUTOMATION* (ed. Choi, SB and Yarlagadda, P and AbdullahAlWadud, M) **511-512**, 78–80 (TRANS TECH PUBLICATIONS LTD, 2014).
38. Dell'Agli, G. & Mascolo, G. Low temperature hydrothermal synthesis of ZrO₂-CaO solid solutions. *J. Mater. Sci.* **35**, 661–665 (2000).
39. Annamalai, A., Eo, Y. D., Im, C. & Lee, M.-J. Surface properties and dye loading behavior of Zn₂SnO₄ nanoparticles hydrothermally synthesized using different mineralizers. *Mater. Charact.* **62**, 1007–1015 (2011).
40. Hirano, M. & Kato, E. Hydrothermal Synthesis of Nanocrystalline Cerium(IV) Oxide Powders. *J. Am. Ceram. Soc.* **82**, 786–788 (1999).
41. Meligrana, G., Gerbaldi, C., Tuel, A., Bodoardo, S. & Penazzi, N. Hydrothermal synthesis of high surface LiFePO₄ powders as cathode for Li-ion cells. *J. Power Sources* **160**, 516–522 (2006).
42. Gallagher, P. K. A simple technique for the preparation of R.E. FeO₃ and R.E. CoO₃. *Mater. Res. Bull.* **3**, 225–232 (1968).
43. Matuura, Y., Matsushima, S., Sakamoto, M. & Sadaoka, Y. NO₂-sensitive LaFeO₃ film prepared by thermal decomposition of the heteronuclear complex {,} {La[Fe(CN)₆][middle dot]5H₂O}. *J. Mater. Chem.* **3**, 767–769 (1993).
44. Sadaoka, Y., Traversa, E. & Sakamoto, M. Preparation and characterization of heteronuclear hexacyano complexes, Ln(x)Sm(1-x){[Co(CN)₆]center dot nH₂O} (Ln=La, Er, and Yb). *Chem. Lett.* 177–178 (1996). doi:10.1246/cl.1996.177

45. Sadaoka, Y., Traversa, E. & Sakamoto, M. Preparation and structural characterization of perovskite-type $\text{La}_x\text{Ln}_{1-x}\text{CoO}_3$ by the thermal decomposition of heteronuclear complexes, $\text{La}_x\text{Ln}_{1-x}[\text{Co}(\text{CN})_6] \cdot n\text{H}_2\text{O}$ ($\text{Ln} = \text{Sm}$ and Ho). *J. Alloys Compd.* **240**, 51–59 (1996).
46. Merzhanov, a. G. Combustion processes that synthesize materials. *J. Mater. Process. Technol.* **56**, 222–241 (1996).
47. Merzhanov, a. G. History and recent developments in SHS. *Ceram. Int.* **21**, 371–379 (1995).
48. González-Cortés, S. L. & Imbert, F. E. Fundamentals, properties and applications of solid catalysts prepared by solution combustion synthesis (SCS). *Appl. Catal. A Gen.* **452**, 117–131 (2013).
49. Kingsley, J. J. & Patil, K. C. A novel combustion process for the synthesis of fine particle α -alumina and related oxide materials. *Mater. Lett.* **6**, 427–432 (1988).
50. LIU, Y. *et al.* Solution combustion synthesis of Ni–Y₂O₃ nanocomposite powder. *Trans. Nonferrous Met. Soc. China* **25**, 129–136 (2015).
51. Subohi, O., Kumar, G. S., Malik, M. M. & Kurchania, R. Synthesis of bismuth titanate with urea as fuel by solution combustion route and its dielectric and ferroelectric properties. *Opt. - Int. J. Light Electron Opt.* **125**, 820–823 (2014).
52. Zhuravlev, V. D. *et al.* Solution combustion synthesis of α -Al₂O₃ using urea. *Ceram. Int.* **39**, 1379–1384 (2013).
53. Roura, P. & Farjas, J. Analytical solution for the Kissinger equation. *J. Mater. Res.* **24**, 3095–3098 (2009).
54. Frank-Kamenetskii, D. A. *Diffusion and Heat Exchange in Chemical Kinetics*. **2nd enl. a**, (Princeton University Press, 1955).
55. Merzhanov, A. G. & Averson, A. E. The present state of the thermal ignition theory: An invited review. *Combust. Flame* **16**, 89–124 (1971).
56. Merzhanov, A. G. & Khaikin, B. I. Theory of combustion waves in homogeneous media. *Prog. Energy Combust. Sci.* **14**, 1–98 (1988).
57. Kerimov, M. K. *Numerical methods in finite element analysis*. *USSR Computational Mathematics and Mathematical Physics* **20**, (1980).
58. Finlayson, B. a. *The Method of Weighted Residuals and Variational Principles - With Application in Fluid Mechanics, Heat and Mass Transfer*. *Mathematics in Science and Engineering* **87**, (1972).
59. Patankar, S. Numerical heat transfer and fluid flow. *Series in computational methods in mechanics and thermal sciences* 1–197 (1980).

60. Singh, B. & Agarwal, P. K. An alternating direction implicit method for magnetohydrodynamic heat transfer in cylindrical geometry with discontinuity in wall temperature. *Int. J. Heat Fluid Flow* **7**, 307–312 (1986).
61. Sakurai, H. Transient and steady-state heat conduction analysis of two-dimensional functionally graded materials using particle method. **64**, 45–54
62. Fort, J., Campos, D., González, J. R. & Velayos, J. Bounds for the propagation speed of combustion flames. *J. Phys. A. Math. Gen.* **37**, 7185 (2004).
63. Press, W., Teukolsky, S., Vetterling, W. & Flannery, B. *Numerical Recipes: The Art of Scientific Computing. Technometrics* **29**, (1987).
64. Crank, J. & Nicolson, P. A practical method for numerical evaluation of solutions of partial differential equations of the heat-conduction type. *Math. Proc. Cambridge Philos. Soc.* **43**, 50–67 (1947).
65. Farjas, J. & Roura, P. Isoconversional analysis of solid state transformations. *J. Therm. Anal. Calorim.* **105**, 757–766 (2011).
66. Farjas, J. & Roura, P. Simple approximate analytical solution for nonisothermal single-step transformations: Kinetic analysis. *AIChE J.* **54**, 2145–2154 (2008).
67. Peaceman, D. W. & H. H. Rachford, J. The Numerical Solution of Parabolic and Elliptic Differential Equations. *J. Soc. Ind. Appl. Math.* **3**, 28–41 (1955).
68. Zhao, S. A Matched Alternating Direction Implicit (ADI) Method for Solving the Heat Equation with Interfaces. *J. Sci. Comput.* 118–137 (2014).
doi:10.1007/s10915-014-9887-0
69. Le Chatelier. De l'action de la chaleur sur les argiles. *Bull. Soc. Franç. Minéral. Cryst* **10**, 204–211 (1887).
70. Beyler, C. L. & Hirschler, M. M. Beyler_Hirschler_SFPE_Handbook_3. 110–131
71. Brebu, M. & Vasile, C. Thermal degradation of lignin—a review. *Cellul. Chem. Technol.* **44**, 353–363 (2010).
72. Chaturvedi, S. & Dave, P. N. Review on Thermal Decomposition of Ammonium Nitrate. *J. Energ. Mater.* **31**, 1–26 (2013).
73. Freeman, E. S. & Carroll, B. The application of thermoanalytical techniques to reaction kinetics: the thermogravimetric evaluation of the kinetics of the decomposition of calcium oxalate monohydrate. *J. Phys. Chem.* **62**, 394–397 (1958).
74. Chakrabarti, S. *et al.* PHYSICAL JOURNAL B Synthesis of γ -Fe₂O₃ nanoparticles coated on silica spheres : **171**, 163–171 (2003).

75. Crisan, M., Jitianu, A., Zaharescu, M., Mizukami, F. & Niwa, S. Sol-Gel Mono- and Poly-component Nanosized Powders in the Al₂O₃-TiO₂-SiO₂-MgO System. *J. Dispers. Sci. Technol.* **24**, 129–144 (2003).
76. Dippong, T., Levei, E. A., Borodi, G., Goga, F. & Barbu Tudoran, L. Influence of Co/Fe ratio on the oxide phases in nanoparticles of Co_xFe_{3-x}O₄. *J. Therm. Anal. Calorim.* **119**, 1001–1009 (2014).
77. Sadek, H. E. H., Khattab, R. M., Gaber, a. a. & Zawrah, M. F. Nano Mg_{1-x}Ni_xAl₂O₄ spinel pigments for advanced applications. *Spectrochim. Acta Part A Mol. Biomol. Spectrosc.* **125**, 353–358 (2014).
78. Guo, X. *et al.* Phase evolution of yttrium aluminium garnet (YAG) in a citrate/nitrate gel combustion process. *J. Mater. Chem.* **14**, 1288 (2004).
79. Hwang, C. C., Huang, T. H., Tsai, J. S., Lin, C. S. & Peng, C. H. Combustion synthesis of nanocrystalline ceria (CeO₂) powders by a dry route. *Mater. Sci. Eng. B Solid-State Mater. Adv. Technol.* **132**, 229–238 (2006).
80. Hwang, C. C., Tsai, J. S. & Huang, T. H. Combustion synthesis of Ni-Zn ferrite by using glycine and metal nitrates - Investigations of precursor homogeneity, product reproducibility, and reaction mechanism. *Mater. Chem. Phys.* **93**, 330–336 (2005).
81. Pathak, L. C., Bandyopadhyay, D., Srikanth, S., Das, S. K. & Ramachandrarao, P. Effect of Heating Rates on the Synthesis of Al₂O₃ - SiC Composites by the Self-Propagating High-Temperature Synthesis (SHS) Technique. **20**, (2001).
82. Ramanathan, S. *et al.* Thermal decomposition behavior of precursors for yttrium aluminum garnet. *J. Therm. Anal. Calorim.* **84**, 511–519 (2006).
83. Suan, M. S. M., Johan, M. R. & Chua Siang, T. Synthesis of Y₃Ba₅Cu₈O₁₈ superconductor powder by auto-combustion reaction: Effects of citrate-nitrate ratio. *Phys. C Supercond. its Appl.* **480**, 75–78 (2012).
84. Mohalik, N. K., Panigrahi, D. C. & Singh, V. K. Application of thermal analysis techniques to assess proneness of coal to spontaneous heating. *J. Therm. Anal. Calorim.* **98**, 507–519 (2009).
85. Kim, M.-G., Kanatzidis, M. G., Facchetti, A. & Marks, T. J. Low-temperature fabrication of high-performance metal oxide thin-film electronics via combustion processing. *Nat. Mater.* **10**, 382–388 (2011).
86. Shaw, T. L. & Carrol, J. C. Application of baseline correction techniques to the 'ratio method' of DSC specific heat determination. **19**, 1671–1680 (1997).
87. Chiu, J. & Fair, P. G. Determination of thermal conductivity by differential scanning calorimetry. *Thermochim. Acta* **34**, 267–273 (1979).

88. Keating, M. Y. & McLaren, C. S. Thermal conductivity of polymer melts. *Thermochim. Acta* **166**, 69–76 (1990).
89. Sircar, A. K. & Wells, J. L. Thermal Conductivity of Elastomer Vulcanizates by Differential Scanning Calorimetry. *Rubber Chem. Technol.* **55**, 191–207 (1982).
90. Marcus, S. M. & Blaine, R. L. Thermal conductivity of polymers, glasses and ceramics by modulated DSC. *Thermochim. Acta* **243**, 231–239 (1994).
91. Simon, S. L. & McKenna, G. B. Measurement of Thermal Conductivity Using TMDSC : *Reinf. Plast.* **18**, 559–571 (1999).
92. Merzlyakov, M. & Schick, C. Thermal conductivity from dynamic response of DSC DO US EX CL PL US EX CL. *Thermochim. Acta* **377**, 183–191 (2011).
93. Hakvoort, G., van Reijen, L. L. & Aartsen, A. J. Measurement of the thermal conductivity of solid substances by DSC. *Thermochim. Acta* **93**, 317–320 (1985).
94. Flynn, J. H. & Levin, D. M. A method for the determination of thermal conductivity of sheet materials by differential scanning calorimetry (DSC). *Thermochim. Acta* **126**, 93–100 (1988).
95. Camirand, C. P. Measurement of thermal conductivity by differential scanning calorimetry. *Thermochim. Acta* **417**, 1–4 (2004).
96. Vyazovkin, S. *et al.* ICTAC Kinetics Committee recommendations for performing kinetic computations on thermal analysis data. *Thermochim. Acta* **520**, 1–19 (2011).
97. Vyazovkin, S. Evaluation of activation energy of thermally stimulated solid-state reactions under arbitrary variation of temperature. *J. Comput. Chem.* **18**, 393–402 (1997).
98. Friedman, H. L. Kinetics of thermal degradation of char-forming plastics from thermogravimetry. Application to a phenolic plastic. *J. Polym. Sci. Part C Polym. Symp.* **6**, 183–195 (1964).
99. Akahira, T. & Sunose, T. Trans. Joint Convention of Four Electrical Institutes , Paper No. 246 , 1969 Research Report. *Chiba Inst. Technol. Sci. Technol.* **16**, 22–31 (1971).

II. MAIN OBJECTIVES

The main objective of this work is to analyze chemical methods as a route to synthesize advanced oxides at low cost and at low temperature with special focus on combustion synthesis. Two chapters are explicitly devoted to this principal goal, Chapter 3 which is dedicated to thin films and Chapter 7, which is dedicated to powders. Several specific objectives are defined:

- In chapter 3 we aimed to analyze the possibility of synthesizing functional oxide thin films at low temperature via combustion synthesis. In addition, we aimed to analyze the low temperature synthesis of thin films in comparison with powders through chemical methods.
- The objective of chapter 7 was to explore the combustion synthesis of perovskite-type oxide powders via SHS using heteronuclear cyano complex precursors.

Given the differences that we found between powders and films we dedicated chapter 6 to analyze analytically and numerically the heat transfer in films and powders that are submitted to a controlled temperature program. We focused the analysis on the condition needed for a thermal explosion to occur in a solid sample reacting without any gas exchange with its surroundings.

As a result, several issues had to be solved:

- Chapter 4 is devoted to analyze the effect of temperature gradients within a sample in the measurement of the temperature in TA. A
- In chapter 5 we aimed to obtain an alternative route to determine the thermal conductivity of powders by DSC.

III. Thermal analysis for low temperature synthesis of oxide thin films from chemical solutions

Reproduced with permission from:

D. Sánchez-Rodríguez, J. Farjas, P. Roura. "Thermal Analysis for Low Temperature Synthesis of Oxide Thin Films from Chemical Solutions". *Journal of Physical Chemistry C*. Vol. 117, Issue 39 (2013) : 20133-20138

<http://dx.doi.org/10.1021/jp4049742>

Copyright © 2013 American Chemical Society

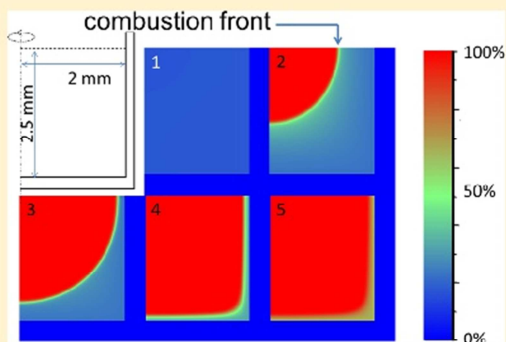
Thermal Analysis for Low Temperature Synthesis of Oxide Thin Films from Chemical Solutions

Daniel Sanchez-Rodriguez,[†] Jordi Farjas,[†] Pere Roura,^{*,†} Susagna Ricart,[‡] Narcís Mestres,[‡] Xavier Obradors,[‡] and Teresa Puig[‡]

[†]GRMT, Department of Physics, University of Girona, Campus Montilivi, 17071 Girona, Catalonia, Spain

[‡]Institut de Ciència de Materials de Barcelona (ICMAB-CSIC), Campus de la UAB, 08193 Bellaterra, Catalonia, Spain

ABSTRACT: The possibility of synthesizing functional oxide thin films at low temperature via combustion synthesis is analyzed both experimentally and numerically. To this aim, the decomposition of several oxide precursors [copper and cerium acetates, yttrium trifluoroacetate, and In_2O_3 and $\text{La}_{0.7}\text{Sr}_{0.3}\text{MnO}_3$ (LSMO) nitrate based precursors] has been analyzed by thermal analysis techniques. It is shown that, although these precursors decompose via combustion when they are in the form of powders, their corresponding films show no evidence of combustion. The reason for this different behavior is clearly revealed with numerical simulations. Thin films will hardly experience combustion because the precursor front extinguishes before reaching the precursor–substrate interface leaving a “cool zone” hundreds of micrometers thick. In contrast, it is argued that thin oxide films can be obtained at temperatures lower than powders because of the enhanced gas transport mechanisms that usually limit the decomposition rate.



INTRODUCTION

The low-temperature fabrication of oxide thin films is attracting much interest because of its remarkable impact on the fabrication of electronic devices on flexible plastic substrates.^{1,2} Films can be obtained by chemical solution deposition (CSD). A solution containing the precursor salt is spread over a substrate, and after solvent evaporation, the precursor is pyrolyzed to obtain the oxide film. Through control of the spreading conditions and solution composition, the film thickness can vary from tens of nanometers to several micrometers. CSD is much more cost-effective than physical deposition techniques and is easily scalable to industrial production. It has been successfully applied to the preparation of superconductor tapes,³ magnetic oxides,⁴ optical films,^{5,6} etc.

Reduction of the processing temperature near or below 200 °C has been achieved by either a suitable choice of the oxide precursor¹ or by improving the annealing conditions. It has been shown that the annealing temperature can be significantly reduced in sol–gel derived films by in situ hydrolysis applied on the surface of the films,⁷ in an O_2/O_3 atmospheric environment,⁸ by microwave assisted annealing,⁹ and by photochemical means.¹⁰

It has been recently claimed¹¹ that a general route to achieving low-temperature processing of films is the choice of suitable chemical precursors that undergo a combustion process. In the case where decomposition is highly exothermic, the heat of reaction may increase the material temperature over the furnace temperature by a large amount leading to thermal runaway. The reaction is no longer homogeneous, but it is almost confined at the combustion front that propagates

through the material. Although the local temperature at the front is very high (a significant fraction of the adiabatic temperature),¹² if the reactive volume is small, the surrounding material may remain at low temperature. This means that the substrate of a thin film could remain unaffected by the high local temperature of the film. Recently, Kim et al.¹¹ have reported that combustion synthesis occurs in nitrate-based precursor oxides for films well below 100 nm in thickness, and they propose that their procedure could constitute a general route for low-temperature synthesis of oxide films on temperature-sensitive substrates.

In fact, combustion synthesis (CS) has been intensively applied for more than 20 years to obtain powders and sintered compacts of refractory materials¹³ and has led to an impressive diversity of processing practices.¹⁴ Nevertheless, its application to the synthesis of layers is essentially limited to foils of Ni–Al and other intermetallic multilayers¹⁵ used for joining technology. In this particular case, practice indicates that CS is only feasible when the foils are several tens of micrometers thick.¹⁶ The reason is that heat dissipation to the substrate limits foil overheating.¹⁷ Although the reaction kinetics of these foils (governed by atomic interdiffusion) is very different from that of precursor decomposition (described approximately by first order kinetics; see below), the role of the substrate on film thermalization remains the same. Consequently, the great expectation¹ arising from the claim that combustion occurs in

Received: May 23, 2013

Revised: September 3, 2013

Published: September 6, 2013

submicrometric films^{11,18,19} demands a more thorough thermal analysis of CS directly performed in films.

In this paper, we report on thermal analysis experiments carried out on a number of precursors currently used in CSD of thin films that find application in fields as diverse as nonvolatile memories [$\text{La}_{0.7}\text{Sr}_{0.3}\text{MnO}_3$ (LSMO)],²⁰ optical films (CeO_2),⁶ nanostructured coated conductors (Y_2O_3 , CeO_2),²¹ electrical contacts (Cu),²² and thin film transistors (In_2O_3).¹¹ Our aim is to show that their decomposition kinetics are very different when they are in the form of powders rather than thin films. These experiments suggest that combustion only takes place in powders. In a second step, the decomposition course of one particular precursor [$\text{Y}(\text{CF}_3\text{COO})_3$] is numerically simulated, giving confirmation that a combustion front only develops for powders. Finally, several general arguments are given to justify why films tend to decompose at a temperature lower than powders.

Before we continue, we should clarify what we mean by “combustion”. According to several papers published 20 years ago,^{23,24} when the research on materials synthesis through combustion processes began: “Combustion necessarily involves an exothermic reaction with sufficient heat release to become self-sustained”. This definition includes those processes where oxidizer and fuel are already contained in the precursor (“autocombustion”) as well as those reactions that need transport of an oxidative gas from the surrounding atmosphere to progress. In this paper we analyze the decomposition of several precursors that experience combustion with or without an internal oxidizer.

EXPERIMENTAL SECTION

Acetate (CeAc_3 and CuAc_2) and trifluoroacetate [$\text{Y}(\text{TFA})_3$] precursors were used in the form of commercially available powders. The water solution of the LSMO precursor contained the corresponding metal nitrates plus 2% by weight polyvinyl alcohol (PVA).^{25,26} The In_2O_3 precursor was synthesized following the procedure described in ref 11. Its molar composition was 1 $\text{In}(\text{NO}_3)_3 \cdot 2.85 \text{H}_2\text{O} / 2.8$ acetylacetone / 5 $\text{NH}_3 / 1 \text{NH}_4\text{NO}_3$. In these last two cases, powders were obtained by evaporation of the solvent.

For the film preparation, the precursors were dissolved in the appropriate solvents. Films of several hundreds of nanometers were obtained by the free spreading of a microdrop containing the precursor on glass substrates (diameter, 12 mm). Films were dried near 100 °C in a vacuum for several minutes. Although most solvent was evaporated, a residual amount remained on the film, giving a characteristic mass loss step in the thermogravimetric (TG) curves (see Figure III-1b). The drying step was avoided for the In_2O_3 precursor films because acetylacetone, which was added to act as fuel, partially evaporated.

Thermal analysis experiments were carried out with a Mettler Toledo TGA851eLF thermobalance that simultaneously delivers the differential thermal analysis (DTA) signal. Since, at the typical decomposition temperatures (200–400 °C), the time response of the DTA signal is very long (tens of seconds),²⁷ the DTA peaks have been deconvoluted by the apparatus time constant to obtain a DTA signal dependence on time (or temperature) closer to reality. The heat of decomposition was obtained through time integration of the DTA peak after calibration with the melting peaks of In and Zn samples. The TG/DTA curves were corrected by the apparatus baseline that was usually measured with a second heating ramp.

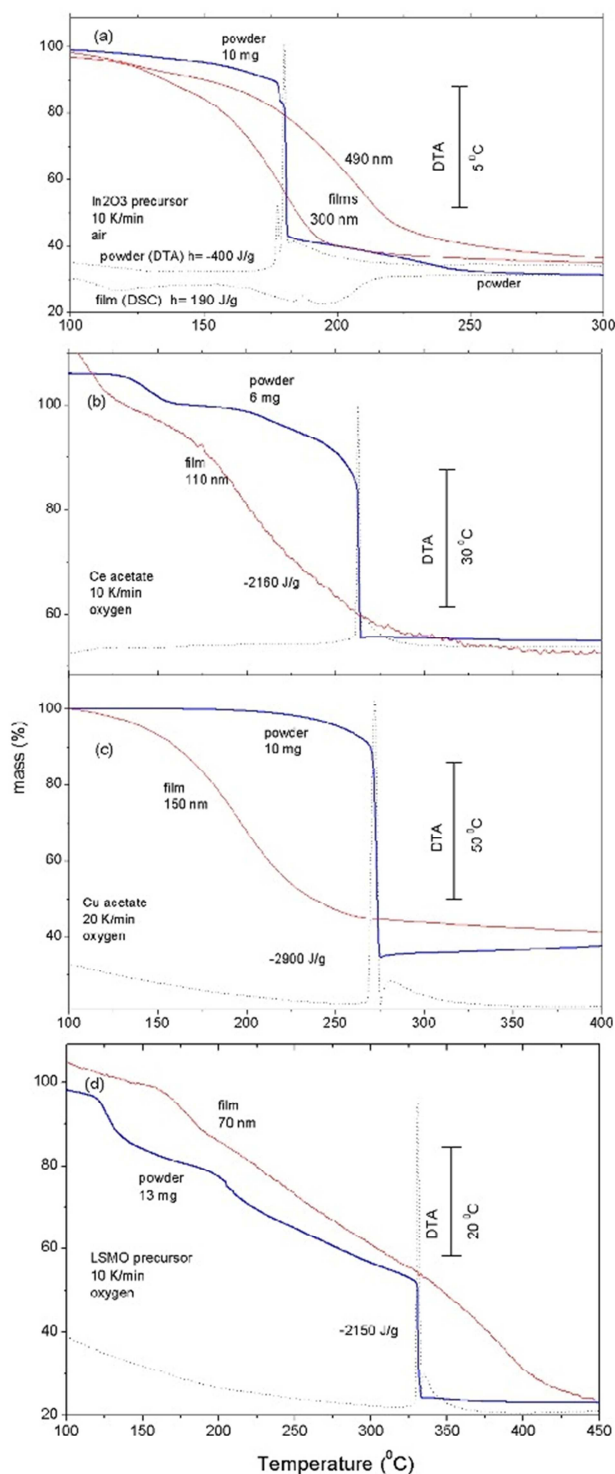


Figure III-1. TG and DTA (or DSC) curves of the thermal decomposition of several metal oxide precursors. (a) In_2O_3 oxide made from nitrate precursors and acetylacetone; (b) cerium acetate for CeO_2 oxide; (c) copper acetate for CuO oxide; (d) LSMO oxides made from nitrate precursors and PVA. For powders, the abrupt mass loss observed in their TG curves and the sharp exothermic DTA peaks constitute a clear signature of combustion. For films these features are absent (DTA signal too weak to be measured). For the In_2O_3 precursor (upper figure) the decomposition changes from exothermic (DTA) in powders to slightly endothermic in films (DSC signal),

Figure III-1. continued

indicating a change in the decomposition mechanism. The heat of decomposition, h , has been obtained from the area of the DTA/DSC peaks.

Although this correction is essential for films, it can be skipped for powders because of the large masses used (>10 mg). High purity oxygen and synthetic air at a flow rate around 50 mL/min were used to control the furnace atmosphere. Complementary experiments were carried out with a differential scanning calorimeter (DSC) from TA Instruments (Q2000 apparatus).

The decomposition products were analyzed by X-ray diffraction (XRD; D8 ADVANCE diffractometer from Bruker AXS collecting the diffracted photons on a CCD detector). The expected metal oxides were obtained for all the precursors with the exception of $Y(TFA)_3$. In this case, YF_3 was obtained instead.²⁸ It must also be said that $CuAc_2$ films led to 100% CuO , whereas, according to the literature,²⁹ $CuAc_2$ decomposition of powders resulted in variable amounts of CuO and Cu_2O . This means that, with the exception of $CuAc_2$, one would expect identical mass losses for films and powders. The discrepancies in the TG curves (Figure III-1) can be generally be ascribed to (a) the small initial mass of films and (b) the difficulty of determining the mass of the dried precursor (that is used for normalization) because of the partial superposition of evaporation and decomposition steps (Figure III-1b).

RESULTS AND DISCUSSION

Thermal Analyses on Powders and Films. Our research on thermal decomposition of metal organic powders has evidenced that, in general, films and powders have different decomposition kinetics. This is especially true for highly exothermic processes such as those occurring with the precursors of Figures III-1 and 2: cerium and copper acetates, $Y(TFA)_3$, and nitrate-based precursors of LSMO and In_2O_3 . The latter case, being the same precursor as in ref 11, has been especially designed to undergo combustion through the mixing of fuel (acetylacetonate) and oxidizer (nitrate) components. The abrupt mass loss step observed in the TG curves of powders is a characteristic feature of a thermal runaway process. Decomposition reaches completion within a few seconds. In addition, DTA curves exhibit a sharp exothermic peak revealing sample overheating. Although we have not done a systematic analysis, we have verified that powders can experience combustion at heating rates lower than those used (10 and 20 K/min). After integration, this peak delivers the heat of decomposition. It must be emphasized that the sample temperature is much higher than the value deduced from the DTA peak due to the finite time response of the apparatus.

In contrast, the TG curves of films are very smooth, indicating that the decomposition rate is lower than in powders and suggesting that combustion does not occur. The DTA curves of films are not shown here because, typically, the heat evolved is too low to be detected. In the particular case of In_2O_3 precursor films, the heat of decomposition has been measured by DSC and an endothermic signal has been recorded (Figures III-1a). This unexpected result could be attributed to evaporation of some of the precursor components during the heating ramp before decomposition¹⁹ (for instance, acetylacetonate boiling point, 140 °C). In fact, we have verified (Figure III-1a) that decomposition of pure indium nitrate in air is

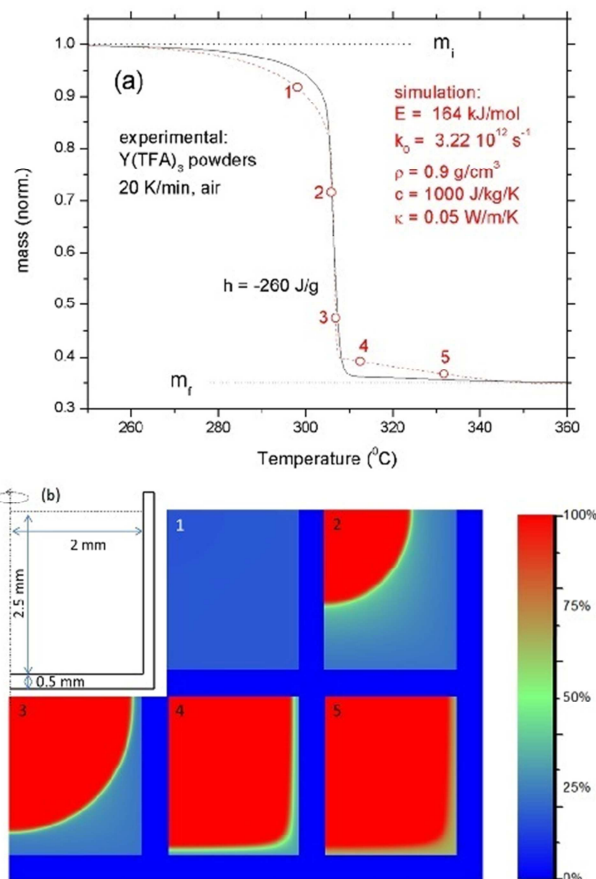


Figure III-2. (a) TG curves for the decomposition of $Y(TFA)_3$ powders when heated at 20 K/min (solid line, experiment; dashed line, simulation). Significant stages of the decomposition course are indicated by open symbols. (b) Geometry of the simulated sample and crucible, and frames showing the local conversion degree inside the powder at the corresponding points indicated in part a. Notice that the combustion front, already visible in frame 2, propagates freely inside the powder (frame 3) but stops at a finite distance from the crucible walls (frames 4 and 5). This “cool zone” is 90 μm thick.

endothermic and the heat exchanged (approximately 300 J/g) is similar to that of thin films (190 J/g). Nevertheless, since combustion is only possible for exothermic reactions, these DSC results constitute solid proof that the decomposition process occurring in these films is without combustion. In fact, we have never observed the characteristic TG/DTA features related to combustion in any film obtained from precursors that do experience combustion when they are in the form of powders.

Numerical Simulation Model. Combustion requires high local overheating that, in turn, increases exponentially the reaction rate and the velocity of the combustion front. Consequently, the absence of an abrupt mass-loss step during film decomposition could be taken as proof of the absence of combustion. This qualitative argument will be substantiated with accurate numerical simulations in this subsection.

To understand the observed differences between films and powders, calculations have been done that simulate the spatial evolution of the transformed fraction inside the material when it is heated at constant rate, β , from the bottom of the crucible

(powders) or substrate (films). We have assumed first order decomposition kinetics, i.e.

$$\frac{\partial \alpha}{\partial t} = k_0 e^{-E/RT} (1 - \alpha) \quad (1)$$

where k_0 , E , and R are the preexponential constant, activation energy of the rate constant, and the Boltzmann constant (or gas constant), respectively, and $\alpha(x,t)$ is the transformed fraction ($\alpha = 0$ before decomposition, $\alpha = 1$ after decomposition).

The heat evolved per unit time and volume, \dot{q} , depends on the decomposition enthalpy per unit mass, h , and the reaction rate according to

$$\dot{q} = \rho(-h) \frac{\partial \alpha}{\partial t} \quad (2)$$

We have verified that heat conduction to the substrate or crucible accounts for most of the heat dissipated. Therefore, conduction through the atmosphere and radiation has been neglected and the heat transport equation

$$\rho c \frac{\partial^2 T}{\partial t^2} = \kappa \left(\frac{\partial^2 T}{\partial x^2} + \frac{\partial^2 T}{\partial y^2} + \frac{\partial^2 T}{\partial z^2} \right) + \dot{q} \quad (3)$$

(κ is the thermal conductivity; ρ , the mass density; c , the specific heat) has been solved inside the material and crucible walls or substrate. Axial symmetry has been assumed for powders (Figure III-2b), whereas for films the problem can be reduced to one dimension (the distance to the substrate). Numerical calculations have been performed by using the dimensionless form of eq 3,³⁰ and it has been solved following an alternating-direction implicit integration method.³¹ The imposed relative error between each time iteration was less than 10^{-14} .

We have chosen $Y(TFA)_3$ for the calculations because its decomposition kinetics and enthalpy are independent of the furnace atmosphere (reactive or inert),²⁸ making it unnecessary to consider any reactive gas transport process into the sample. However, the assumption of our model that decomposition occurs in the solid state is not completely exact even for this particular precursor because volatile species produced during the reaction will carry away part of the reaction heat.

In this particular case, the exothermic reaction needed for combustion to occur is simply the decomposition of the $Y(TFA)_3$ molecule into YF_3 . This is to say that, according to our general definition of combustion, the chemical reaction must not necessarily involve an internal oxidizer (as in the In_2O_3 and LSMO precursors) or an oxidant atmosphere (as in copper and cerium acetates). Our model (eqs 1–3) can be applied with the same degree of accuracy to precursors with internal oxidizers. However, when applied to those precursors reacting with the surrounding atmosphere, it would predict a range of conditions leading to combustion wider than in experiment because gas transport into the sample could be the rate-limiting step of the reaction and, consequently, it could make combustion more difficult to occur. Consequently, we can be sure that combustion will not occur if our model predicts so.

Results of the Numerical Simulations. For $Y(TFA)_3$, the numerical values of k_0 and E have been obtained through the kinetic analysis of TG experiments³² whereas h was directly measured by DSC.²⁸ The value of ρ has been measured, c comes from reasonable assumptions, and κ has been left as a fitting parameter.

The results are plotted in Figures III-2 and 3 for powders and films, respectively. For powders, decomposition is homoge-

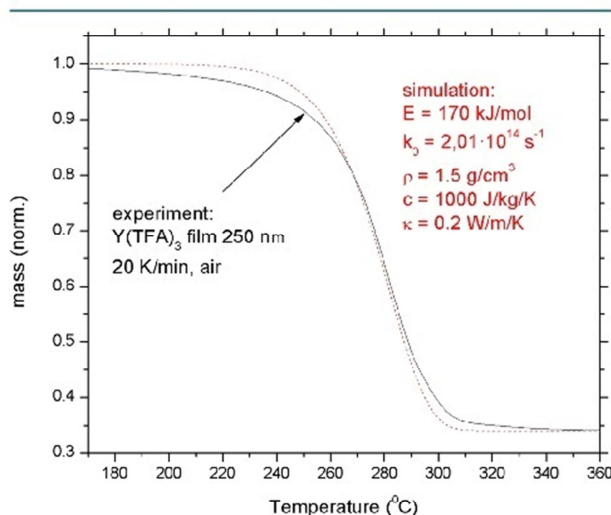


Figure III-3. TG curves of the decomposition of a $Y(TFA)_3$ 250 nm film. In this case, frames of the conversion degree are not shown because decomposition is completely homogeneous.

neous, until the slope of the TG curve increases abruptly (Figure III-2a). In other words, in this initial step, α does not depend on the position and can be calculated as

$$\alpha(t) = \frac{m_i - m(t)}{m_i - m_f} \quad (4)$$

where the masses on the right-hand side are taken from the TG curve. This behavior is confirmed by the first frame of Figure III-2b where we see that the transformed fraction is the same at any point of the sample. Then decomposition accelerates because a combustion front appears (second frame of Figure III-2b) that propagates through the powder (third frame) at 1.0 mm/s. The local transformed fraction of a given region changes abruptly from a small value to 1 when the front sweeps it. Since the local overheating at the combustion front is high (230 K, near the adiabatic overheating temperature of 260 K), decomposition is completed in less than 0.2 s. When the front approaches the crucible wall, it stops and extinguishes itself, leaving a “cool zone” 90 μ m thick (frames 4 and 5) that does not experience any significant overheating. This means that this zone decomposes at a much lower rate, which is given by eq 1 with T equal to the furnace temperature. Consequently, the TG curve becomes smooth again and exhibits a last step extending over 40 °C (Figure III-2a).

Good agreement between the calculated and experimental TG curves of $Y(TFA)_3$ has been achieved with a realistic value of κ (about 1/4 of the value for a dense film), giving us confidence in the process description obtained from the theoretical simulation. In particular, the existence of a “cool zone” near the crucible walls is especially important. Although less pronounced, the characteristic step is observed in the experimental curve (Figure III-2a). The experimental TG curves in Figure III-1 reveal that this zone also appears during the decomposition of the In_2O_3 and LSMO precursors (Figure III-1a,d), suggesting that it is a general feature of CS of oxide precursor powders. The case of the copper acetate is clearly different. The mass gain observed after the abrupt mass loss is

due to the oxidation of Cu and Cu_2O to CuO ²⁹ and hides the probable existence of a cool zone. A similar effect can occur with cerium acetate.

After the success of the simulations with powders, we can apply the same procedure to films. For films, calculations show that decomposition is always homogeneous through their whole thickness (i.e., at any time the transformed fraction α is essentially the same irrespective of the distance to the substrate—variations are below 10^{-7}) and, consequently, the calculated TG curve lacks the characteristic sharp step of combustion (Figure III-3). Again, like powders, the agreement between the simulated and experimental TG curves is very good. In view of the results obtained with powders, the lack of combustion in films can be easily understood. For combustion to occur, the film should be thicker than a “cool zone” similar to that identified in the case of powders.

We have undertaken a thorough numerical and analytical study of the conditions needed for combustion to occur in films, based on eqs 1–3, that generalizes the results obtained for $\text{Y}(\text{TFA})_3$ films. From this study we have concluded that, within realistic values of the heating rate and the kinetic and thermal constants, CS of metal oxides is very unlikely (or impossible) to occur for submicrometric films.

Low-Temperature Decomposition of Films. The good news is that, for many precursors, films decompose at a lower temperature than powders (see Figure III-1a–c and notice also that the preexponential constant, k_0 , is much higher for the $\text{Y}(\text{TFA})_3$ film than for powders—Figures III-2a and 3). This general property is related to the nature of the decomposition reactions, because they involve gas transport into or out of the sample and, owing to their higher surface to volume ratio, transport is easier in films, and, consequently, decomposition is faster. This property should allow oxide films to be synthesized at low temperature, even without combustion. We have verified this prediction with the particular precursor of In_2O_3 used in ref 11. The XRD curves of Figure III-4 correspond to the product of powders and a 450 nm thick film heated to 250 and 200 °C for 1 h, respectively. Peak width analysis with Scherrer's formula indicates that, due to combustion, powders have larger

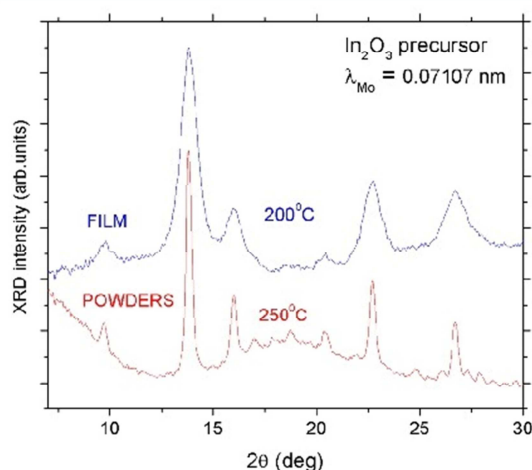


Figure III-4. XRD curves of In_2O_3 synthesized from precursor powders and from a 450 nm thin film annealed at 250 and 200 °C, respectively. It is shown that, either with (powders) or without (film) combustion, the product obtained at low temperature is highly crystalline (the peak width of the powder curve is the instrumental line width).

crystallites ($>13 \text{ nm}$) than the film ($4.5 \pm 0.3 \text{ nm}$). This last size is actually similar to that obtained in ref 11 at 200–250 °C (around 6 nm) in films tens of nanometers thick, giving additional proof that high crystallinity is obtained in films at rather low temperatures without combustion.

While the present results clearly contradict the claim that CS could be a general route for thin film production, it must be emphasized that, owing to their higher surface to volume ratio, thin films tend to decompose at a lower temperature than powders do (in addition to the examples given here, look at ref 33), with this effect being more pronounced for very thin films. This property has allowed us to obtain ceria thin films from cerium propionate at a temperature as low as 160 °C,³⁴ and it also applies to the In_2O_3 precursors analyzed here. Remarkably, the decomposition temperature during constant heating at 10 K/min of the 300 nm thick film was 30 °C lower than that of the 490 nm film (Figure III-1a).

Finally, we wish to stress that our work elicits that, as a general rule, thermal analyses carried out on precursor powders cannot be simply extrapolated to predict the behavior of thin films and that thermal analysis measurements on films are required to elucidate the actual decomposition mechanism and to explore the possibility to obtain oxide films at a lower synthesis temperature.³⁵ Although thermal analyses on films are harder to conduct, the extra effort is worthwhile.

CONCLUSION

In conclusion, thermal analysis experiments done on metal oxide precursors reveals that, when their decomposition is moderately or highly exothermic, powders often decompose via combustion. In contrast, no evidence of combustion is observed in films. In fact, numerical simulations show that the combustion front extinguishes before reaching the precursor–substrate interface and leaves a “cool zone” where heat dissipation is so efficient that no overheating occurs and, consequently, decomposition proceeds much more slowly. Since films are thinner than the typical thickness of this “cool zone” (hundreds of micrometers), combustion of submicrometric precursor films is very improbable if not impossible. Although these experiments and simulations leave the question open as to why precursor solutions containing oxidizer/fuel pairs are suitable for oxide thin film synthesis at low temperature, it has been argued that many oxide precursors decompose at a much lower temperature when they are in the form of films due to the transport enhancement of volatiles during the course of solid–gas reactions.

AUTHOR INFORMATION

Corresponding Author

*E-mail: pere.roura@udg.cat. Tel.: 34 972418383.

Notes

The authors declare no competing financial interest.

ACKNOWLEDGMENTS

This work was partially funded by the Spanish Programa Nacional de Materiales through Projects MAT2011-28874-C02-01 and MAT2011-28874-C02-02, by the Consolider program Nanoselect, CSD2007-00041, and by the Generalitat de Catalunya Contract Nos. 2009SGR-185 and 2009SGR-770. The GRMT group thanks Dr. Joan Pere López of SGR, UdG, for his technical support.

REFERENCES

- (1) Jeong, S.; Moon, J. Low-Temperature, Solution-Processed Metal Oxide Thin Film Transistors. *J. Mater. Chem.* **2012**, *22*, 1243–1250.
- (2) Fortunato, E.; Barquinha, P.; Martins, R. Oxide Semiconductor Thin-Film Transistors: A Review of Recent Advances. *Adv. Mater.* **2012**, *24*, 2945–2986.
- (3) Gutiérrez, J.; Llordés, A.; Gázquez, J.; Gibert, M.; Romà, N.; Ricart, S.; Pomar, A.; Sandiumenge, F.; Mestres, N.; Puig, T.; Obradors, X. Strong Isotropic Flux Pinning in YBa₂Cu₃O_{7-x}-BaZrO₃ Nanocomposite Superconductor Films Derived from Chemical Solutions. *Nat. Mater.* **2007**, *6*, 367–373.
- (4) Moreno, C.; Abellán, P.; Hassini, A.; Ruyter, A.; Pérez del Pino, A.; Sandiumenge, F.; Casanove, M. J.; Santiso, J.; Puig, T.; Obradors, X. Spontaneous Outcropping of Self-Assembled Insulating Nanodots in Solution-Derived Metallic Ferromagnetic La_{0.7}Sr_{0.3}MnO₃ Films. *Adv. Funct. Mater.* **2009**, *19*, 2139–2146.
- (5) Cavallaro, A.; Sandiumenge, F.; Gázquez, J.; Puig, T.; Obradors, X.; Arbiol, J.; Freyhardt, H. C. Growth Mechanism, Microstructure and Surface Modification of Nanostructured CeO₂ Films by Chemical Solution Deposition. *Adv. Funct. Mater.* **2006**, *16*, 1363–1372.
- (6) Peña-Rodríguez, O.; Sánchez-Valdés, C. F.; Garriga, M.; Alonso, M. L.; Obradors, X.; Puig, T. Optical Properties of Ceria-Zirconia Epitaxial Films Grown From Chemical Solutions. *Mater. Chem. Phys.* **2013**, *138*, 462–467.
- (7) Banger, K. K.; Yamashita, Y.; Mori, K.; Peterson, R. L.; Leedham, T.; Rickard, J.; Siringhaus, H. Low-Temperature, High-Performance Solution-Processed Metal Oxide Thin-Film Transistors Formed by a 'Sol-Gel on Chip' Process. *Nat. Mater.* **2011**, *10*, 45–50.
- (8) Han, S.-Y.; Herman, G. S.; Chang, C.-H. Low-Temperature, High-Performance, Solution-Processed Indium Oxide Thin-Film Transistors. *J. Am. Chem. Soc.* **2011**, *133*, 5166–5169.
- (9) Jun, T.; Song, K.; Yeong, Y.; Woo, K.; Kim, D.; Bae, C.; Moon, J. High-Performance Low-Temperature Solution-Processable ZnO Thin Film Transistors by Microwave-Assisted Annealing. *J. Mater. Chem.* **2011**, *21*, 1102–1108.
- (10) Smith, R. D. L.; Prévot, M. S.; Fagan, R. D.; Zhang, Z.; Sedach, P. A.; Siu, M. K. J.; Trudel, S.; Berlinguette, C. P. Photochemical Route for Accessing Amorphous Metal Oxide Materials for Water Oxidation Catalysis. *Science* **2013**, *340*, 60–63.
- (11) Kim, M.-G.; Kanatzidis, M. G.; Facchetti, A.; Marks, T. J. Low-Temperature Fabrication of High-Performance Metal Oxide Thin-Film Electronics Via Combustion Processing. *Nat. Mater.* **2011**, *10*, 382–388.
- (12) Moore, J. J.; Feng, H. J. Combustion Synthesis of Advanced Materials. 1. Reaction Parameters. *Prog. Mater. Sci.* **1995**, *39*, 243–273.
- (13) Patil, K. C.; Aruna, S. T.; Mimani, T. Combustion Synthesis: An Update. *Curr. Opin. Solid State Mater. Sci.* **2002**, *6*, 507–512.
- (14) Morsi, K. The Diversity of Combustion Synthesis Processing: A Review. *J. Mater. Sci.* **2012**, *47*, 68–92.
- (15) Reeves, R. V.; Rodriguez, M. A.; Jones, E. D., Jr.; Adams, D. P. Condensed-Phase and Oxidation Reaction Behavior of Ti/2B Foils in Varied Gaseous Environments. *J. Phys. Chem. C* **2012**, *116*, 17904–17912.
- (16) Wang, J.; Besnoin, E.; Knio, O. M.; Weihs, T. P. Effects of Physical Properties of Components on Reactive Nanolayer Joining. *J. Appl. Phys.* **2005**, *97*, 114307.
- (17) Rabinovich, O. S.; Grinchuk, P. S.; Andreev, M. A.; Khina, B. B. Conditions for Combustion Synthesis in Nanosized Ni/Al Films on a Substrate. *Physica B: Condens. Matter* **2007**, *392*, 272–280.
- (18) Hennek, J. W.; Kim, M.-G.; Kanatzidis, M. G.; Facchetti, A.; Marks, T. J. Exploratory Combustion Synthesis: Amorphous Indium Yttrium Oxide for Thin-Film Transistors. *J. Am. Chem. Soc.* **2012**, *134*, 9593–96.
- (19) Kim, M.-G.; Hennek, J. W.; Kim, H. S.; Kanatzidis, M. G.; Facchetti, A.; Marks, T. J. Delayed Ignition of Autocatalytic Combustion Precursors: Low-Temperature Nanomaterial Binder Approach to Electronically Functional Oxide Films. *J. Am. Chem. Soc.* **2012**, *134*, 11583–11593.
- (20) Moreno, C.; Munuera, C.; Valencia, S.; Kronast, F.; Obradors, X.; Ocal, C. Reversible Resistive Switching and Multilevel Recording in La_{0.7}Sr_{0.3}MnO₃ Thin Films for Low Cost Nonvolatile Memories. *Nano Lett.* **2010**, *10*, 3828–3835.
- (21) Llordés, A.; Palau, A.; Gázquez, J.; Coll, M.; Vlad, R.; Pomar, A.; Arbiol, J.; Guzmán, R.; Ye, S.; Rouco, V.; Sandiumenge, F.; Ricart, S.; Puig, T.; Varela, M.; Chateigner, D.; Vanacken, J.; Gutiérrez, J.; Moshchalkov, V.; Deutscher, G.; Magen, C.; Obradors, X. Nanoscale Strain-Induced Pair Suppression as a Vortex Pinning Mechanism in High-Temperature Superconductors. *Nat. Mater.* **2012**, *11*, 329–336.
- (22) Yabuki, A.; Tanaka, S. Electrically Conductive Copper Film Prepared at Low Temperature by Thermal Decomposition of Copper Amine Complexes with Various Amines. *Mater. Res. Bull.* **2012**, *47*, 4107–4111.
- (23) Subrahmanyam, J.; Vijayakumar, M. Self-Propagating High-Temperature Synthesis. *J. Mater. Sci.* **1992**, *27*, 6249–6273.
- (24) Yi, H. C.; Moore, J. J. Self-Propagating High-Temperature (Combustion) Synthesis (SHS) of Powder-Compacted Materials. *J. Mater. Sci.* **1990**, *25*, 1159–1168.
- (25) Carretero-Genevri, A.; Gázquez, J.; Puig, T.; Mestres, N.; Sandiumenge, F.; Obradors, X.; Ferain, E. Nanostructural Evolution of Metastable Solution Grown Vertical (La,Sr)MnO₃ Nanorods Assisted by Polymeric Templates. *Adv. Funct. Mater.* **2010**, *20*, 892–897.
- (26) Malowney, J.; Mestres, N.; Borrise, X.; Calleja, A.; Guzman, R.; Llobet, J.; Arbiol, J.; Puig, T.; Obradors, X.; Bausells, J. Functional Oxide Nanostructures Written by EBL on Insulating Single Crystal Substrates. *Microelectron. Eng.* **2013**, *110*, 94–99.
- (27) Roura, P.; Farjas, J. Analysis of the Sensitivity and Sample-Furnace Thermal-Lag of a Differential Thermal Analyzer. *Thermochim. Acta* **2005**, *430*, 115–122.
- (28) Eloussifi, H.; Farjas, J.; Roura, P.; Camps, J.; Dammak, M.; Ricart, S.; Puig, T.; Obradors, X. Evolution of Yttrium Trifluoroacetate during Thermal Decomposition. *J. Therm. Anal. Calorim.* **2012**, *108*, 589–596.
- (29) Kondrat, S. A.; Davies, T. E.; Zu, Z.; Boldrin, P.; Bartley, J. K.; Carley, A. F.; Taylor, S. H.; Rosseinsky, M. J.; Hutchings, G. J. The Effect of Heat Treatment on Phase Formation of Copper Manganese Oxide: Influence on Catalytic Activity for Ambient Temperature Carbon Monoxide Oxidation. *J. Catal.* **2011**, *281*, 279–289.
- (30) Fort, J.; Campos, D.; González, J. R.; Velayos, J. Bounds for the Propagation Speed of Combustion Flames. *J. Phys. A: Math. Gen.* **2004**, *37*, 7185–7198.
- (31) Press, W.; Teukolsky, S. A.; Vetterling, W. T.; Flannery, B. P. *Numerical Recipes*, 3rd ed.; Cambridge University Press: New York, 2007; Chapter 20.
- (32) Eloussifi, H.; Farjas, J.; Roura, P.; Dammak, M. Non-Isothermal Model-Free Predictions. *J. Therm. Anal. Calorim.* **2012**, *108*, 597–603.
- (33) Eloussifi, H.; Farjas, J.; Roura, P.; Ricart, S.; Puig, T.; Obradors, X.; Dammak, M. Thermal Decomposition of Barium Trifluoroacetate Thin Films. *Thermochim. Acta* **2013**, *556*, 58–62.
- (34) Roura, P.; Farjas, J.; Ricart, S.; Aklalouch, M.; Guzman, R.; Arbiol, J.; Puig, T.; Calleja, A.; Peña-Rodríguez, O.; Garriga, M.; Obradors, X. Synthesis of Nanocrystalline Ceria Thin Films by Low-Temperature Thermal Decomposition of Ce-Propionate. *Thin Solid Films* **2012**, *520*, 1949–1953.
- (35) Farjas, J.; Sanchez-Rodríguez, D.; Eloussifi, H.; Cruz Hidalgo, R.; Roura, P.; Ricart, S.; Puig, T.; Obradors, X. Can We Trust on the Thermal Analysis of Metal Organic Powders for Thin Film Preparation? *Mater. Res. Soc. Symp. Proc.* **2012**, *1449*, 13–18.

IV. Thermal gradients in thermal analysis experiments: Criteria to prevent inaccuracies when determining sample temperature and kinetic parameters



Thermal gradients in thermal analysis experiments: Criteria to prevent inaccuracies when determining sample temperature and kinetic parameters



D. Sánchez-Rodríguez^a, H. Eloussifi^{a,b}, J. Farjas^{a,*}, P. Roura^a, M. Dammak^b

^a GRMT, Department of Physics, University of Girona, Campus Montilivi, E17071 Girona, Catalonia, Spain

^b Laboratoire de Chimie Inorganique, Faculté des Sciences de Sfax, Université de Sfax, BP 1171, 3000 Sfax, Tunisia

ARTICLE INFO

Article history:

Received 11 March 2014

Received in revised form 30 April 2014

Accepted 2 May 2014

Available online 14 May 2014

Keywords:

Thermal analysis
Thermogravimetry
Sample thermal lag
Exothermic reactions
Heat transport

ABSTRACT

Thermal analysis methods are customarily used to analyze the evolution of solid-state transformations when samples are submitted to a controlled temperature program. Thermal analysis results are generally interpreted under the assumption that no temperature gradients take place inside the sample, so that, under proper calibration the sample temperature can be determined and controlled. Two phenomena may contribute to the formation of temperature gradients within the sample: heat transport through the sample and heat evolved during an exothermic or endothermic transformation. We will provide two analytical relationships that relate the sample mass with the temperature gradient within the sample and that will provide a straightforward criterion for checking the reliability of the sample temperature. We will show that, because of their very low thermal conductivity, significant thermal gradients may occur in those samples in the form of powders. Besides, in the case of exothermic reactions and for typical experimental conditions, the heat released by the reaction significantly affects the determination of the sample temperature. Finally, we analyze how sample overheating affects the observed reaction kinetics.

© 2014 Elsevier B.V. All rights reserved.

1. Introduction

Thermal analysis techniques, such as differential scanning calorimetry (DSC) and thermogravimetry (TG), are routinely used to analyze the evolution of solid-state transformations. Thermal analysis instruments are designed to monitor a given temperature dependent property as a function of time or temperature when a sample is submitted to a controlled temperature program, usually a constant temperature (isothermal) or a constant temperature rise (constant heating rate). In these apparatus, the sample temperature sensor does not have perfect thermal contact with the sample, i.e., samples are placed inside a crucible which, in turn, is placed over a sample holder which is in thermal contact with the temperature sensor. Moreover, in general the temperature program is controlled by measuring the temperature in the furnace. Under proper calibration, a reference temperature is determined from the furnace temperature which ideally would correspond to the sample temperature provided that there is no temperature delay between the sample and its holder.

Although isothermal experiments may be easier to interpret [1], constant heating rate measurements are preferred [2] because they not only allow for a larger temperature range to be analyzed, but they are faster, and they avoid the problem of non-zero initial degree of transformation [3]. However, in constant heating rate measurements, the separation between the sample and the temperature sensors results in noticeable deviations in the sample and reference temperatures from the programmed temperature [4–9]. Deviations of the reference temperature with the heating rate are approximately proportional to an apparatus characteristic time called “tau lag” [10–12]. Most calibration procedures allow a tau lag correction, so that, commercial apparatus are able to deliver an accurate and almost heating rate-independent reference temperature.

In addition, there is also a temperature delay for the sample temperature called “sample thermal lag”, which depends on sample and crucible properties and results in the formation of temperature gradients within the material, meaning it cannot be systematically corrected with an apparatus calibration.

Two different effects contribute to deviations of the actual sample temperature with the sample temperature determined from the sample holder or furnace sensor [9,13,14]: the thermal gradients related to heat transport through the sample [4,15–18] and heat evolved due to endothermic or exothermic reactions of the

* Corresponding author. Tel.: +34 972418490; fax: +34 972418098.

E-mail addresses: jordi.farjas@udg.cat, farjas@gmail.com, jordi.farjas@gmail.com (J. Farjas).

<http://dx.doi.org/10.1016/j.tca.2014.05.001>

0040-6031/© 2014 Elsevier B.V. All rights reserved.

sample. Temperature gradients are known to increase with heating rate and sample mass. Excessive sample masses may result in a sample temperature shift to higher temperatures [19]. As a rule of thumb, for DSC a mass of around 1 mg is recommended, while for TG masses between 1 to 10 mg are commonly used. In fact, to confirm that sample temperature is sufficiently accurate, a check of its independence on the sample mass has been proposed [3,20], i.e., the sample mass needs to be reduced until no dependence of the evolution of the transformation on the sample mass is observed.

As for the second cause, heat evolved during transformation may result in noticeable deviations of the sample's temperature due to either self-heating or self-cooling as the reaction develops [14,20–22]. These deviations are more noticeable for larger sample masses and high enthalpy transformations [23]. As a rule of thumb, it has been proposed that the rate of heat generation must not exceed 8 mW [4].

The effect of heat transfer within the sample has been thoroughly analyzed and modeled [12,18,24,25]. The thermal inertia of the sample is responsible for a temperature delay between the sample and the sample temperature sensor, as well as a thermal gradient occurring within the sample. However, no analytical relationship between the temperature difference within the sample and the sample mass has been reported. In addition, few works are devoted to analyzing the effect of the heat evolved. Neft et al. [20], have developed a numerical model that accounts for heat and gas transport within the sample. This model is successfully applied to the analysis of soot oxidation. Merzhanov et al. [2] shows that non-isothermal kinetic methods can fail in the case of exothermic reactions. Finally, Holba et al. [18] analyze the temperature profile in a sample that exhibits a first order-phase transition. However, as far as we know, a general description of the effect of the heat evolved during exothermic reactions on the measurement is still lacking.

In this paper we numerically and experimentally analyze the artifacts induced by heat transport and the heat released by exothermic reactions. In Section 2 we provide the experiment details. In Section 3 we introduce the numerical model used in the simulations. In Section 4 we analyze the effect of the heat transport through the sample, while in Section 5 we study the effect of the heat released during the transformation. Finally, in Section 6 we analyze the effect of local overheating on the kinetic analysis of the reaction.

2. Experimental

The synthesis of barium trifluoroacetate $\text{Ba}(\text{CF}_3\text{COO})_2$ ($\text{Ba}(\text{TFA})_2$) and yttrium trifluoroacetate $\text{Y}(\text{CF}_3\text{COO})_3$ ($\text{Y}(\text{TFA})_3$) powders is described in refs. [26] and [27]. The preparation of $\text{Ba}(\text{TFA})_2$ and $\text{Y}(\text{TFA})_3$ films is described in refs. [28] and [29]. TG analysis was performed with a Mettler Toledo TG model TG851e. Simultaneous TG and DTA analysis was performed with a Setaram model SETSYS Evolution 16 thermobalance. TG curves were corrected by subtracting a consecutive identical second measurement and by measuring the final sample mass at room temperature. Powders were placed inside alumina crucibles. To facilitate gas exchange between the sample and the furnace atmosphere crucible lids were not used. Gas flow was controlled by mass flow meters. High purity gases at a flow rate of around 50 ml/min were used to control the furnace atmosphere. Water-saturated gases were obtained by bubbling the carrier gas in water at standard temperature and pressure (25 °C, 1 atm). DSC analysis was performed with a Mettler Toledo DSC model 822. Powders were placed inside aluminum crucibles and perforated lids were used to facilitate the gas exchange.

Table IV-1

Physical parameters of the two metalorganic powders analyzed.

	$\text{Ba}(\text{TFA})_2$	$\text{Y}(\text{TFA})_3$
Thermal conductivity, λ , W/(mK)	0.08	0.06
Specific heat capacity, c , J/(kgK)	2230	875
Density, ρ , kg/m ³	1463	1114
Thermal diffusivity, m ² /s	2.45×10^{-8}	6.15×10^{-8}
Specific heat of reaction, q , J/kg	1.0×10^6	2.75×10^5
Activation energy, E_a , J/mol	1.77×10^5	1.70×10^5
Pre-exponential constant, A , s ⁻¹	4.5×10^{13}	3.4×10^{13}
Dimensionless η	47.5	65.0

The parameters used to simulate the thermal evolution of $\text{Y}(\text{TFA})_3$ and $\text{Ba}(\text{TFA})_2$ were determined experimentally and are summarized in Table IV-1. Density is determined from the sample weight when it is placed in a container with well-known volume. Heat capacity, thermal conductivity and the heat of the reaction were measured by DSC. The heat of the reaction is given in refs. [26,27], heat capacity was measured at 150 °C using the method described in [30] and thermal conductivity was determined at the indium melting point (156 °C) by adapting the method described in ref. [31] to powders. Finally, determining the activation energy and pre-exponential constant is described in detail in Section 6.

3. Numerical model

Our numerical model is based on the heat conduction through the sample and crucible. Thermal losses by radiation or convection are neglected. We assume that the sample holder acts as a heat sink whose temperature is fully controlled by the temperature program and we neglect any contact resistance between the holder and the crucible. In general, crucibles are hollow cylinders, therefore, due to their symmetry (see Fig. IV-1), the temperature evolution may be described by a two-dimensional (2D) model [2,20,32].

$$\rho c \frac{\partial T}{\partial t} = \lambda \left(\frac{1}{r} \frac{\partial}{\partial r} r \frac{\partial T}{\partial r} + \frac{\partial^2 T}{\partial z^2} \right) + \rho q \frac{\partial \alpha}{\partial t}, \quad (1)$$

where ρ is the density, c is the specific heat capacity, T is the temperature, t is the time, λ is the thermal conductivity, r and z are the radial and axial coordinates (see Fig. IV-1), q is the specific heat of reaction (positive for exothermic reactions) and $\alpha(r, z, t)$ is the degree of transformation ($\alpha = 0$ untransformed, $\alpha = 1$ totally transformed). We also assume that the reaction kinetics is governed by a single mechanism (single-step reaction [33]) and that it is

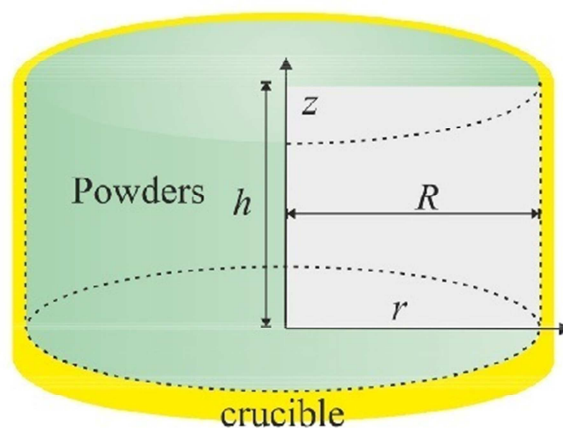


Fig. IV-1. Schematic representation of the geometry analyzed, Eq. (1).

thermally activated (the reaction rate follows an Arrhenius temperature dependence):

$$\frac{\partial \alpha}{\partial t} = A e^{-E_A/R_G T} f(\alpha), \quad (2)$$

where A is the pre-exponential constant, E_A is the activation energy, R_G is the universal gas constant and $f(\alpha)$ the function describing the reaction mechanism. For the sake of simplicity, in the numerical simulations we assume a first-order reaction kinetics, i.e., $f(\alpha) = 1 - \alpha$.

The boundary conditions for $T(r, z)$ are:

$$\left. \frac{\partial T}{\partial r} \right|_{r=0} = 0, \quad T(R, z) = T_f, \quad \left. \frac{\partial T}{\partial z} \right|_{z=h} = 0, \quad T(r, 0) = T_f$$

and $T_f = T_{f,0} + bt$ (3)

where R is the inner crucible radius, h is the sample thickness (see Fig. IV-1), T_f is the furnace temperature, $T_{f,0}$ is the initial furnace temperature and b the programmed constant temperature rise.

The model analysis is significantly simplified after rewriting Eqs. (1), (2) and (3) in a dimensionless form [34]:

$$\frac{\partial \theta}{\partial \tau} = \left(\frac{1}{\zeta} \frac{\partial}{\partial \zeta} \zeta \frac{\partial \theta}{\partial \zeta} + \frac{\partial^2 \theta}{\partial \zeta^2} \right) + \frac{1}{\eta} \frac{\partial \alpha}{\partial \tau} \quad (4)$$

$$\frac{\partial \alpha}{\partial \tau} = \eta e^{-1/\theta} (1 - \alpha) \quad (5)$$

$$\left. \frac{\partial \theta}{\partial \zeta} \right|_{\zeta=0} = 0, \quad \theta(\varepsilon, \zeta) = \theta_f, \quad \left. \frac{\partial \theta}{\partial \zeta} \right|_{\zeta=\delta} = 0, \quad \theta(\zeta, 0) = \theta_f$$

and $\theta_f = \theta_{f,0} + \beta \tau$ (6)

The dimensionless temperature θ , time τ and space coordinates ζ and ε , are defined as follows:

$$\theta \equiv T \frac{R_G}{E_A} \quad (7)$$

$$\tau \equiv t \frac{R_G q A}{c E_A} \quad (8)$$

$$\zeta \equiv r \sqrt{\frac{R_G q A \rho}{\lambda E_A}}, \quad \varepsilon \equiv z \sqrt{\frac{R_G q A \rho}{\lambda E_A}} \quad (9)$$

The dimensionless reciprocal adiabatic temperature rise η is defined as,

$$\eta \equiv c \frac{E_A}{R_G q} \quad (10)$$

The same temperature, time and length scale factors of Eqs. (7)–(9) have been used to calculate the dimensionless inner crucible radius ε , sample height δ , furnace temperature θ_f and heating rate β . The dimensionless model is fully described by four parameters, namely η , ε , δ and β . An alternating-direction semi-implicit integration method has been used to solve of Eqs. (4)–(6) [35]. The numerical code has been written in visual C++.

Finally, it is worth recalling that all the parameters used in the simulations have been determined experimentally (Section 2), thus no free parameters are left to adjust the numerical results to the observed evolutions. Therefore, the agreement between numerical simulations and measured evolutions is a test of the goodness of the model.

4. Temperature delay related to heat conduction within the sample

In this section we will analyze the temperature gradient within the sample due to heat conduction as the furnace temperature is raised at a constant rate, $b = \partial T / \partial t$. We will consider an inert sample, i.e., there is no heat evolution, ($q = 0$ and $\eta = \infty$). After a transient period, any point in the sample will achieve the same heating rate b (see Appendix). Under these circumstances Eq. (1) transforms into:

$$b = a \left(\frac{1}{r} \frac{\partial}{\partial r} r \frac{\partial T}{\partial r} + \frac{\partial^2 T}{\partial z^2} \right), \quad (11)$$

where a is the thermal diffusivity ($a = \lambda / \rho c$). In general, the thermal diffusivity of powders is much smaller than that of the crucible material; therefore, one can assume that the crucible temperature is nearly homogeneous and that the temperature delay takes place exclusively within the sample.

In the limit case $h \gg R$ (according to some authors [32], h should be at least three times R), the partial derivative with respect z can be neglected in Eq. (11), so the system is reduced to a one dimensional (1D) model. Under this simplification, the stabilized temperature profile within the sample has been analytically calculated [2,18] and the temperature difference through the sample is given by:

$$\Delta T \equiv T(R) - T(0) = \frac{1}{4} \frac{b}{a} R^2. \quad (12)$$

Similarly, when $R \gg h$ the partial derivative with respect r can be neglected and the temperature difference through the sample is given by:

$$\Delta T \equiv T(0) - T(h) = \frac{1}{2} \frac{b}{a} h^2. \quad (13)$$

Note that in Eqs. (12) and (13), the temperature difference is defined in such a way that it is positive, i.e., the temperature is at its maximum next to the crucible walls and steadily diminishes as we approach the top center region of the sample.

Unfortunately, in practical situations h and R are similar and so none of the above approximations are realistic. From Eq. (11) it is clear that the temperature gradient is proportional to b/a . Besides, Eq. (11) contains two space yardstick, h and R , consequently the temperature can be described as a function of a dimensionless position and one dimensionless parameter h/R . This parameter h/R accounts for the aspect ratio of the sample, i.e., for thin films $h/R \rightarrow 0$ while an infinite length cylinder corresponds to $h/R \rightarrow \infty$. Finally, if the length used to normalize the space coordinates in Eq. (11) is the volume to the 1/3 power, $V^{1/3}$, ($V = \pi R^2 h$), then the temperature difference is described by,

$$\Delta T \equiv T(R, 0) - T(0, h) = C \frac{b}{a} V^{2/3}, \quad (14)$$

where C is a parameter that depends on the ratio h/R . From Eqs. (12) and (13) it is immediate that $C = 1/4((1/\pi)(R/h))^{2/3}$ and $C = 1/2((1/\pi)(h/R)^2)^{2/3}$ for the limiting cases $h/R \rightarrow \infty$ and $h/R \rightarrow 0$, respectively.

In Fig. IV-2 we have plotted the value of parameter C determined from the numerical integration of Eqs. (4) and (6) and for different values of the ratio h/R , together with the values of the limiting cases $h/R \rightarrow 0$ and $h/R \rightarrow \infty$. When h is larger than three times R the relative error in the calculation of ΔT from Eq. 12 is below 3%, and when R is larger than three times h the relative error in the calculation of ΔT from Eq. (13) is below 5%. However, when R and h are similar, Eqs. (12) and (13) provide a poor determination of ΔT , for instance when $h/R = 0.71$ the relative error of Eqs. (12) and (13) coincides and is equal to 64%, therefore, with the closest approximation, the inaccuracies related to the 1D model are below 64%.

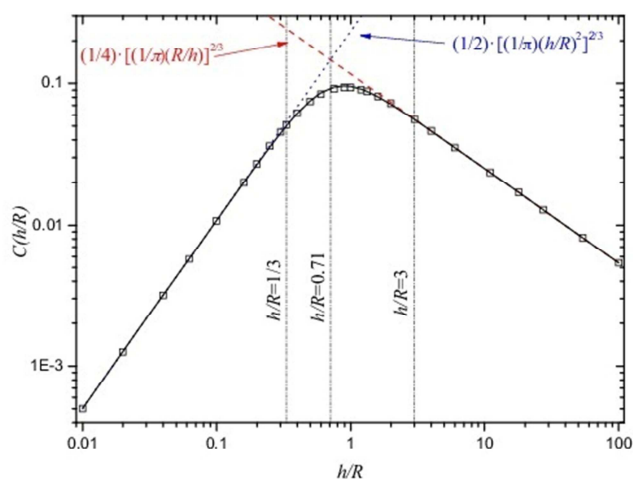


Fig. IV-2. Squares: parameter $C(h/R)$, Eq. (14), calculated from the numerical integration of Eqs. (4) and (6). The solid line corresponds to the analytical solution, Eq. (15). Dotted and dashed lines are the limit cases when h/R tends to 0 and ∞ , respectively.

ΔT can be more accurately approximated by (see solid line in Fig IV-2):

$$C = \frac{1}{2} \left(\frac{(h/R)^2}{\pi + 2\pi\sqrt{2}(h/R)^3} \right)^{2/3} \quad (15)$$

The discrepancies between Eq. (15) and the numerical results are below 3%.

Once we know ΔT (Eqs. (14) and (15)), we can establish a criterion for the maximum sample mass, m_{crit} , to prevent a significant temperature gradient within the sample:

$$m_{crit} = \rho \left(\frac{1}{C} \frac{a}{b} \Delta T \right)^{3/2} \quad (16)$$

Thermocouples and thermistors have accuracies well below 1 K, but temperature calibration methods, thermal contacts and tau lag corrections result in typical apparatus inaccuracies of around 1 K when determining the temperature. Therefore, for practical purposes, it is of no use to look for inaccuracies below 1 K, so in all our determinations we have chosen as a reference value $\Delta T = 1$ K.

To get a feeling for the numbers given by Eq. (16), we have calculated m_{crit} for the two metalorganic precursors analyzed, $\text{Ba}(\text{TFA})_2$ and $\text{Y}(\text{TFA})_3$ (see Table IV-1), two metals, indium and aluminum, whose melting point is commonly used in temperature calibrations and alumina which, together with aluminum, are typical materials for crucibles (see Table IV-2). As for b , we have taken a typical value of 10 K/min and for C we have taken the average value, 0.078, between $h/R = 1/3$ and 3.

In the case of $\text{Ba}(\text{TFA})_2$ and $\text{Y}(\text{TFA})_3$ in the form of powders, the critical masses are 3.8 and 11.5 mg, respectively. These are in a fair agreement with the general criterion that sample masses should be below 10 mg [19]. In contrast, the critical masses for indium, aluminum and alumina are 1.5, 1.7 and 0.12 kg. Such huge differences between powders and bulk materials are mainly related to the differences in the thermal conductivity, i.e., for most solids $\rho c \approx 3 \times 10^6 \text{ J/m}^3 \text{ K}$ so $a \approx \lambda / (3 \times 10^6)$ [36]. The thermal conductivity

Table IV-2
Thermal parameters of different substrates.

	In	Al	Al_2O_3
Thermal conductivity, λ , W/(m K)	82	237	39
Specific heat capacity, c , J/(kg K)	243	917	775
Density, ρ , kg/m ³	7310	2700	3980
Thermal diffusivity, m ² /s	4.6×10^{-5}	9.6×10^{-5}	1.3×10^{-5}

of $\text{Ba}(\text{TFA})_2$ and $\text{Y}(\text{TFA})_3$ is about three orders of magnitude lower than that of indium, aluminum and alumina. This is because of the lower conductivity of metalorganic precursors but, much more importantly, because of the presence of voids between particles. The critical mass, Eq. (16), can vary significantly from sample to sample because of its dependency on thermal conductivity. Accordingly, the rule of thumb that the mass should be below 10 mg is too crude to be taken as a general criterion.

From the different thermal behavior of powders and bulk materials, it is clear that the temperature delay through the crucible is negligible when samples are in the form of powders. One may also conclude that there is no need to be concerned about thermalization in the case of bulk samples. However, the latter conclusion is not always correct. In our calculation we have assumed a perfect thermal contact between sample and crucible. This holds approximately in the case of powders but, in general, is unrealistic in the case of bulk materials. For instance, before calibration, metals are usually melted to ensure good thermal contact.

Finally, unlike tau lag, the thermal lag related to heat conduction through the sample cannot be corrected. The reason being that a temperature gradient inside the sample is formed, i.e., the sample temperature is ill defined with an uncertainty equal to ΔT . This thermal lag results in an apparent shift to higher temperatures of the peak temperature (the temperature at which the transformation rate is maximum) as the sample mass is increased, i.e., the temperature interval at which the transformation takes place is artificially enlarged. This is because the temperature steadily diminishes as we move away from the crucible walls, so the evolution of the transformation is delayed in time. This time delay is translated into an apparent shift to higher temperatures of the sample temperature.

5. Temperature delay related to heat evolved from the sample

In this section we will analyze the sample thermal lag related to the heat evolved in an exothermic transformation, thus $q > 0$ ($\eta > 0$). In this case, due to the heat released by the transformation, the actual sample temperature is higher than the measured sample temperature. Therefore, the process shifts to an apparent lower temperature and the duration of the process is reduced as the sample mass is increased. This evolution of the sample mass is quite the opposite of what we have just described in the previous section. This odd behavior is apparently in contradiction with common experience that is based on the earlier described temperature shift related to heat conduction.

The shift to lower temperatures when the mass is increased has been reported for two exothermic reactions: combustion of soot [20] and thermal degradation of $\text{Ba}(\text{TFA})_2$ [26]. The temperature rise, due to the exothermic reaction, may eventually induce a runaway process provided that the sample thickness is beyond a critical value [23]. In this case, a combustion front is formed and the transformation happens in a very short time interval which results in a characteristic sharp and abrupt evolution [20,23,37]. Conversely, in the case of endothermic process the behavior is just the opposite, the reaction shifts to higher temperatures when the sample mass is increased [22].

The particular behavior of exothermic reactions is shown in Fig. IV-3 where we have plotted the experimental evolution together with the numerical simulation, Eqs. (4)–(6), (parameters indicated in Table IV-1) of thermal decomposition of $\text{Ba}(\text{TFA})_2$ into BaF_2 for different sample masses. One can observe that the numerical model fails to provide an accurate description of the evolution because in Eq. (5) we assumed that the process is controlled by a first-order reaction, whereas it is shown that the kinetics is controlled by two

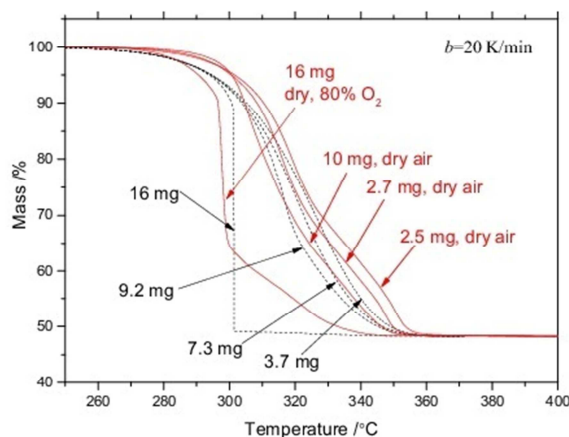


Fig. IV-3. Evolution of the thermal decomposition of Ba(TFA)₂ for different sample masses; solid (red) lines correspond to experimental data while dashed (black) lines are the numerical solution of Eqs (4)–(6). Samples were placed inside an alumina crucible of an internal and external radius of 2 and 2.5 mm, respectively. The sample and crucible thermal parameters are detailed in Table IV-1 and 2. The reaction kinetics depends on the oxygen partial pressure [26], to simulate the case of a $p(\text{O}_2) = 80\%$ we have taken $E_A = 1.75 \times 10^5 \text{ J/mol}$ and $A = 3.0 \times 10^{13} \text{ s}^{-1}$. (For interpretation of the references to color in this figure legend, the reader is referred to the web version of this article.)

competing mechanisms [26]. Moreover, all simulation parameters have been determined experimentally, thus inaccuracies in their determination may result also in noticeable deviations. Nevertheless, the numerical model correctly describes the shift to lower temperatures as the sample mass is increased. In addition, for the largest mass both experimental and numerical data show an abrupt evolution related to the formation of a combustion front [23].

In Movie 1 we show the evolution of the temperature as a function of space and time for the sample of 3.7 mg in Fig. IV-3 (the evolution of the degree of transformation as well as two cases undergoing combustion are given in the supplementary material). Initially, due to heat transport, the temperature next to the crucible is higher than that of the center of the sample, but as the reaction rate increases the temperature gradient flips over and the hottest part is located at the top center of the sample. So, it is clear that after a while the reaction progresses faster at the top center of the sample. The reason being the crucible walls are a thermal sink that allows rapid heat dissipation thus preventing local overheating and, consequently, the maximum temperature is at the top center of the sample while the minimum is next to the crucible walls. Since the reaction is thermally activated, the farther from the crucible walls a given location is, the sooner the reaction is completed.

To establish a relationship between the ΔT within the sample and the system parameters we will consider the 1D model, this assumption greatly simplifies the analysis. In fact, near the stationary solution, Eq. (11), the 1D and 2D models qualitatively exhibit the same behavior, their significant difference being the quantitative value of ΔT . This discrepancy may be corrected by taking advantage of the analysis of the coefficient C (introduced in the previous section), so that we are able to determine the equivalent sample thickness for a 1D system that quantitatively exhibits the same behavior as a given 2D system and vice versa (the procedure is described in the following). To check this assumption, in Fig. IV-4 we plotted the 2D numerical simulations of Fig. IV-3 together with the equivalent 1D simulations. We also added a 2D case where $h/R = 0.71$, in this instance the larger deviations between the 1D and 2D models are to be expected (see Fig. IV-2). For $h/R = 0.71$ and the lowest mass ($m = 3.7 \text{ mg}$), we observe a perfect quantitative agreement between the 1D and 2D simulations. In the first case there is no local overheating while for $m = 3.7 \text{ mg}$, the local overheating is

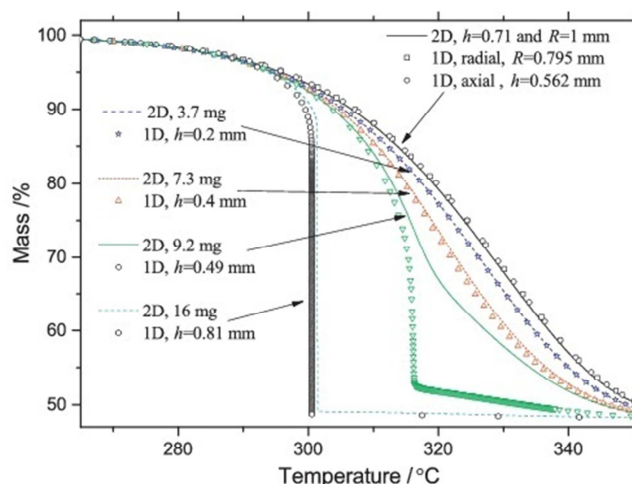


Fig. IV-4. Comparative between 2D model (lines) and the equivalent 1D model (symbols) for the simulations that are shown in Fig. IV-3 and for a case where $h/R = 0.71$. For the latter, we have taken $q = 0$ to simulate the stationary case and no substrate is considered.

relatively low ($\Delta T \leq 2.7 \text{ K}$). Therefore, this assumption holds when we approach the stationary case, in our case this is not a limitation because we are looking for a criterion to avoid overheating so that, as described in the previous section, we are going to consider that $\Delta T \leq 1 \text{ K}$. However, for $m = 7.3 \text{ mg}$, the local overheating reaches a maximum value of 6.3 K and one can observe a slight deviation of the 1D model from the 2D model. Conversely, our assumption fails in the occurrence of a significant overheating or a thermal runaway, in the latter case, the dynamic behavior of the 2D case is much more complex than that of the 1D model. For instance, for $m = 9.2 \text{ mg}$ the 1D simulation undergoes a thermal runaway while the 2D simulation exhibits a significant overheating but no thermal runaway takes place.

The system is ruled by two timescales related to heat dissipation through conduction and heat evolved from the exothermic reaction. For the 1D case, the diffusion time scale, t_D , is related to sample thickness, h , for a plane sheet ($h < R$) or the radius R for an infinite length cylinder, ($h \gg R$) and thermal diffusivity, a ,

$$t_{D,axial}^{(1D)} = \frac{h^2}{a} = h^2 \frac{\rho C}{\lambda}, \quad t_{D,radial}^{(1D)} = \frac{1}{2} \frac{R^2}{a} \quad (17)$$

The reaction time, t_R , can be defined as the full width at half maximum (FWHM) of the transformation rate peak [1]. When there are no significant temperature gradients, the evolution is controlled by the reaction kinetics, Eq. (2), and t_R is given by [1,38]:

$$t_R = \frac{c_R}{A e^{-E_A/R_C T_{Max}}} \quad (18)$$

where T_{Max} is the temperature at which the reaction rate is maximum and c_R is a constant that depends on the reaction model. For instance, for a first-order reaction $c_R = 2.44639$ (values of c_R for various reaction models are given in [1]). It is worth recalling that Eq. (18) holds for any reaction model provided that the reaction rate may be described by a single-step reaction with a rate constant that follows an Arrhenius temperature dependence [38]. In addition, T_{Max} is given by Kissinger's relationship [39]:

$$\frac{E_A}{R_C T_{Max}^2} = \frac{A}{b} e^{-E_A/R_C T_{Max}} \quad (19)$$

T_{Max} can easily be calculated with high accuracy by iteratively applying the analytical approximate solution given in ref. [40].

When $t_R \gg t_D$, heat removal is faster than heat generation, and therefore no significant ΔT is to be expected. So, thermal gradients

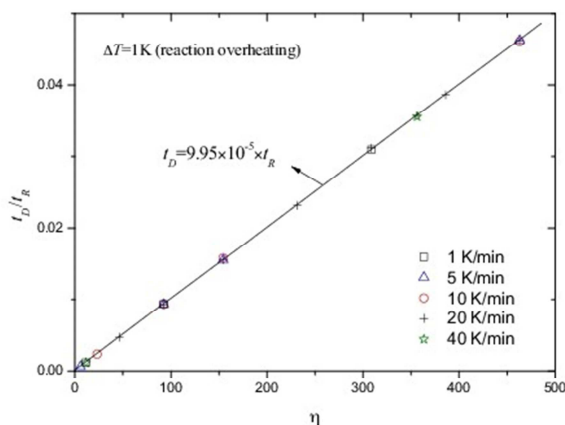


Fig. IV-5. Symbols: rate of the diffusion and reaction times at which the maximum temperature difference within the sample related to the heat of the exothermic reaction is equal to 1 K. The solid line is a linear fit.

may occur when t_R is similar to t_D . In Fig. IV-5, and for different values of the parameters η and β , we have numerically determined the value of the dimensionless sample thickness δ that results in a temperature difference $\Delta T = 1$ K. Once we know the value of δ we are able to calculate τ_D ($\tau_D = \delta^2$ according to Eq. 17 and using the space and time scales from Eqs. (8) and (9)). From the FWHM of the reaction rate peak, we determine τ_R so that we can calculate the ratio t_D/t_R which is τ_D/τ_R . Therefore, we have plotted the ratio t_D/t_R at which $\Delta T = 1$ K as a function of all system free parameters, namely η and β . Fig. IV-5 covers most practical situations; taking the parameters of Ba(TFA)₂ powders as reference (see Table IV-1), b ranges from 1 to 40 K/min and the enthalpy q goes from 1×10^5 to 1×10^7 J/kg (η from 500 to 5). As we will see in the following, higher values of q typically result in critical masses well below 1 mg, thus local overheating is virtually impossible to prevent in a TA apparatus. Conversely, for lower values of q , temperature gradients related to the heat of the reaction are, in general, much smaller than those related to heat diffusion, so the criterion provided in the previous section prevails.

From Fig. IV-5 it is worth noting that the criterion is independent of the dimensionless heating rate and that it is simply proportional to coefficient η . This result indicates that the ratio between a fixed ΔT and the maximum possible overheating is equal to a fixed ratio between the diffusion and reaction times (as the maximum overheating is the adiabatic temperature rise, which in turn is the reciprocal of coefficient η , we obtain a time ratio which is proportional to η for a fixed ΔT). Now, from the linear fitting of Fig. IV-5 and by combining Eqs. (10) and (18), the diffusion time is given by,

$$t_D = \frac{cE_A}{R_G q} \frac{C_R}{Ae^{-E_A/R_G T_{Max}}} \times 10^{-4}. \quad (20)$$

For the 1D case the diffusion time is given by Eq. (17). To deal with the general 2D case, the diffusion time should be corrected according to our analysis of heat conduction in the previous section,

$$t_D^{(2D)} = \frac{2C}{a} V^{2/3}. \quad (21)$$

Note that the equivalent thickness for a 1D model is simply obtained by equating Eqs. (17) and (21).

Finally, by combining Eqs. (20) and (21) we can establish a criterion for the maximum sample mass, m_{Crit} , to prevent a temperature gradient larger than 1 K within the sample:

$$m_{Crit} = \rho \left(\frac{5 \times 10^{-5} caE_A}{C} \frac{C_R}{R_G q Ae^{-E_A/R_G T_{Max}}} \right)^{3/2}. \quad (22)$$

This criterion not only depends explicitly on the thermal parameters of the system (c , a , q), the reaction model (C_R) and the kinetic parameters in the rate constant (A , E_A) but it also depends implicitly on the heating rate, b , through T_{Max} (Eq. (19)).

We have analyzed the critical masses for the cases of Ba(TFA)₂ and Y(TFA)₃ for a heating rate of 20 K/min, assuming a first order reaction ($C_R = 2.44639$) and taking for C an average value of 0.078, and we have obtained 0.041 and 0.020 mg, respectively. In other words, due to the heat released by the reaction for these two precursors at 20 K/min, it is virtually impossible to prevent the formation of a significant temperature gradient within the sample.

From Eq. (22), it is clear that the kinetic parameters (i.e., the reaction time) play a key role in the criterion. For instance, if we reduce the heating rate from 20 to 1 K/min the critical masses for Ba(TFA)₂ and Y(TFA)₃ become 3.0 and 14 mg, respectively; so at this heating rate local overheating may be prevented. Also a relevant parameter is the reaction enthalpy, the larger the enthalpy is, the lower the critical mass is. For instance, if we increase the enthalpy by a factor 10, the critical mass is reduced by a factor 30.

Besides, the average heat flow released during the reaction can be calculated as,

$$\frac{\langle m(dq/dt) \rangle}{(C_R/Ae^{-E_A/R_G T_{Max}}) = (q/t_R)m} \approx (q \times m) \quad (23)$$

where m is the sample mass. By substituting m_{Crit} in Eq. (23) we can estimate the maximum heat flow allowed to prevent overheating. Using the results of Ba(TFA)₂ and Y(TFA)₃ for $b = 1$ K/min we obtain maximum heat flows of 1.4 and 1.8 mW, respectively. These results are fairly consistent with the unproved criterion that heat generation must not exceed 8 mW [4]. However, if we combine Eqs. (22) and (23), the critical heat flow is given by,

$$\langle m \frac{dq}{dt} \rangle_{Crit} = \rho \left(\frac{5 \times 10^{-5} caE_A}{C} \frac{C_R}{R_G} \right)^{3/2} \left(\frac{C_R}{qAe^{-E_A/R_G T_{Max}}} \right)^{1/2} \quad (24)$$

From this equation it is clear that the critical heat flow is not nearly constant at all. For instance the critical heat flow for Ba(TFA)₂ and Y(TFA)₃ when $b = 20$ K/min is 0.33 and 0.44 mW, respectively. Thus, the maximum value of 8 mW [4] is too rough a criterion to be considered seriously.

Another relevant parameter is the geometrical aspect ratio h/R . In Fig. IV-2, note that the parameter C exhibits a strong dependence on h/R . In the case of films, h/R is very small so the critical mass may be significantly larger. For instance, we analyzed the thermal degradation of Ba(TFA)₂ films of thicknesses of the order of 8 μ m deposited on circular substrates of radius 12 mm [28]. The mass of such films is 1.32 mg, so when heated at 20 K/min they are well above the previous value of the critical mass, but for these films the coefficient C is 3.42×10^{-5} , thus the critical mass becomes significantly larger, $m_{Crit} = 6.3 \times 10^3$ mg, i.e., the radius to thickness ratio in films ensures a near perfect thermalization through the substrate that prevents local overheating [37,41].

In Fig. IV-6 we have plotted the evolution of the thermal degradation of Ba(TFA)₂ in the form of powders and films and at different heating rates. One can observe that, due to overheating, at the beginning of the decomposition (Fig. IV-6b) the transformation rate is higher in powders than in films. Finally, to exclude any overheating in films, we numerically simulated the thermal decomposition of Y(TFA)₃ [37]. We obtained perfect agreement with the experiment, and simulation shows that temperature differences within the sample are negligible (below 10^{-5} K).

6. Kinetic analysis

As we mentioned above, thermal gradients within the sample alter the expected reaction course. This effect affects the

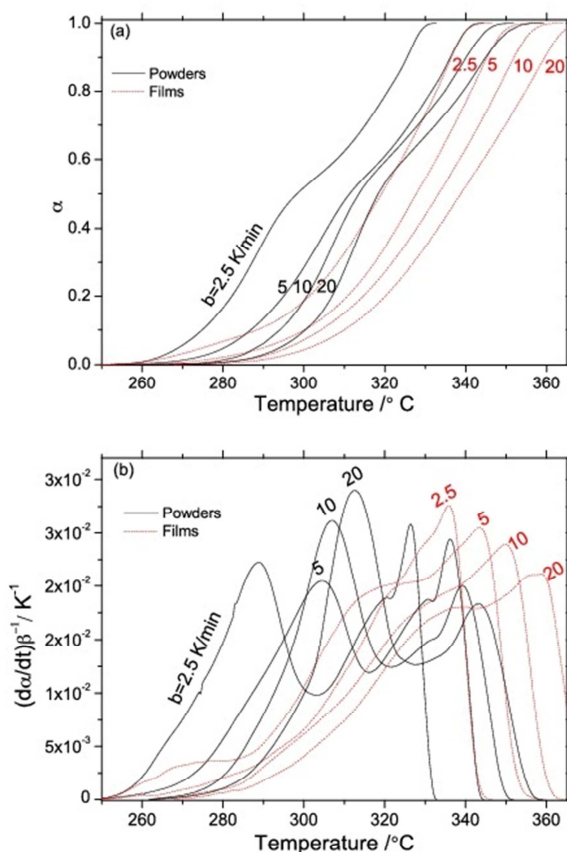


Fig IV-6. Evolution of the thermal decomposition of $\text{Ba}(\text{TFA})_2$ in the form of powders (solid lines) and films (dashed lines) obtained from TG experiments performed at different heating rates. Initial masses for powders are 10.0 mg while four films with an initial total mass between 1.0 and 1.5 mg where heated simultaneously to have a good TG signal.

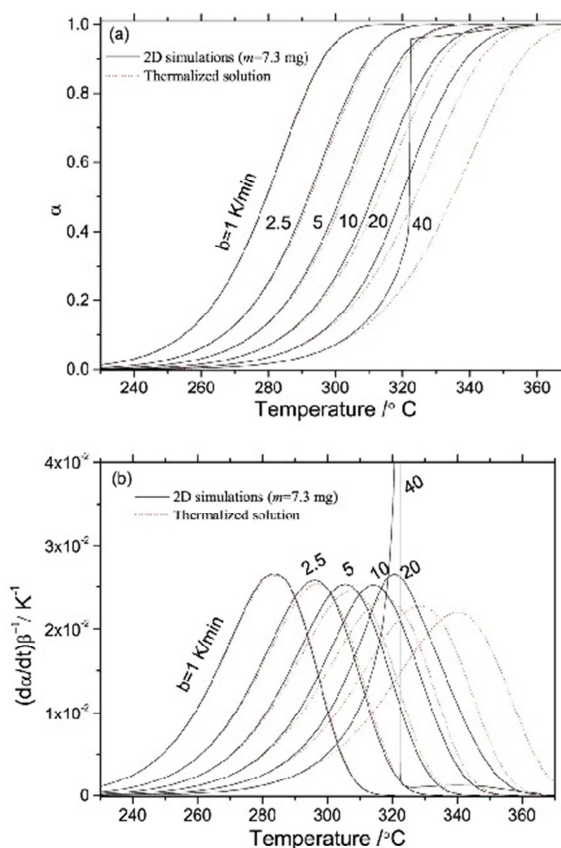


Fig. IV-7. Solid line: 2D simulations of the evolution of thermal decomposition of $\text{Ba}(\text{TFA})_2$ for a fixed mass of 7.3 mg and inner crucible radius of 2 mm, and for different heating rates. The dotted lines correspond to the expected evolution if thermalization were perfect, i.e., no thermal gradients occur within the sample.

determination of the activation energy. In the case of thermal gradients induced by the heat of the reaction, this effect is even more dramatic because the temperature gradients change during the reaction course. Taking a constant sample mass to prevent this artifact is pointless because the temperature gradients also depend on the heating rate (Eqs. (19) and (22)) and in the case of a non-isothermal kinetic analysis it is compulsory to measure the evolution at different heating rates [3,42].

In Fig. IV-7 we have plotted the simulated evolution of $\text{Ba}(\text{TFA})_2$ for a fixed mass and for different heating rates together with the expected evolution in the case of perfect thermalization. From Fig. IV-7 it is apparent that the heat released by the reaction results in a diminution of the reaction time, whereas in the transformation rate plot (Fig. IV-7b) the peaks are narrower and sharper. As we have discussed in the previous section, the higher the transformation rate, the more pronounced the effect is, e.g., for a heating rate of 1 K/min the critical mass is 3 mg, so the thermal gradient is still relatively small and the simulated and thermalized curves are very similar; conversely, for a heating rate of 20 K/min the critical mass is 0.041 mg and large deviations are observed. The more dramatic case corresponds to a heating rate of 40 K/min where a thermal runaway takes place (Fig. IV-7b).

The artifact induced by the local overheating also affects quantitatively and qualitatively the determination of the kinetic parameters. In Fig. IV-8 we have determined the activation energy of curves in Fig. IV-7 using the modified Ortega's isoconversional method [43–45]. One can observe that we obtain an apparent activation

energy which depends on the degree of transformation; which may be interpreted in terms of a complex reaction kinetics [33,46–48] despite the fact that a single first order reaction model was used in the simulations. Accordingly, in the occurrence of local overheating it seems impossible to derive the kinetic parameters. However, at

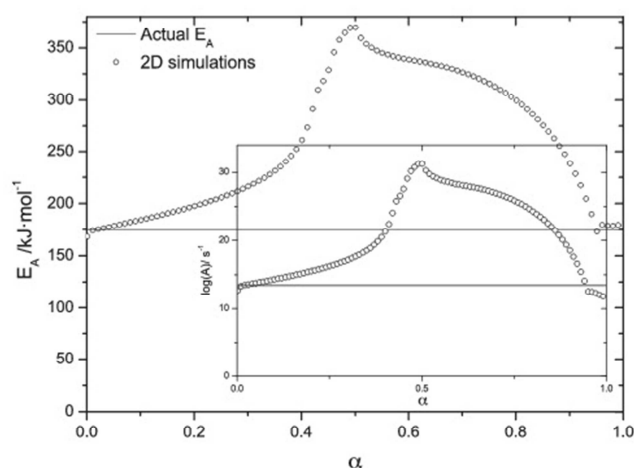


Fig. IV-8. Determination of the activation energy of the simulations shown in Fig. IV-7 using the modified Ortega's isoconversional method [44]. The solid line corresponds to the value of the activation energy and pre-exponential term used in the simulations.

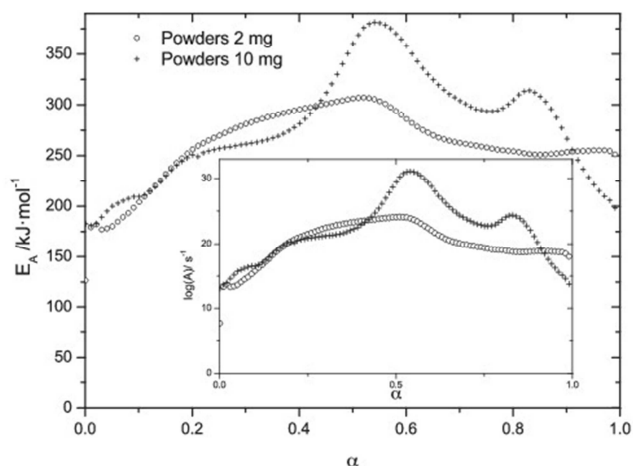


Fig. IV-9. Experimental activation energy of the thermal degradation of $\text{Ba}(\text{TFA})_2$ powders determined with the modified Ortega's isoconversional method [44]. The evolutions at different heating rates used in the determination of the activation energy for powders with a constant mass of 10 mg are shown in Fig. IV-6.

the very early stages of the reaction, the heat released is negligible and the observed kinetics approaches that of the thermalized regime. This is apparent from Fig. IV-7, where even in the most unfavorable case ($b = 40 \text{ K/min}$), the evolution at the very early stages virtually coincides with that of the thermalized regime. Also, in Fig. IV-8, one can observe that when $\alpha \rightarrow 0$ the apparent activation energy approaches the actual activation energy of the reaction. In Fig IV-9 we have used this strategy to determine the kinetic parameters (see Table IV-1) of the thermal degradation of $\text{Ba}(\text{TFA})_2$. Note that, when $\alpha < 0.2$ the values of the activation energy determined for powders of different masses almost coincide.

The particular case of combustion, which corresponds to the decomposition of $\text{Y}(\text{TFA})_3$ in the form of powders shown in Fig. IV-10 and 11, is interesting in itself. In the case of powders, the masses are so large that thermal runaway takes place resulting in an abrupt mass change (Fig. IV-11a) and in a sharp peak in the transformation rate plot (Fig. IV-11b), whereas no combustion takes place in films (no abrupt evolution is observed). When a combustion front appears, it rapidly propagates. From Fig. IV-11 one can observe that the

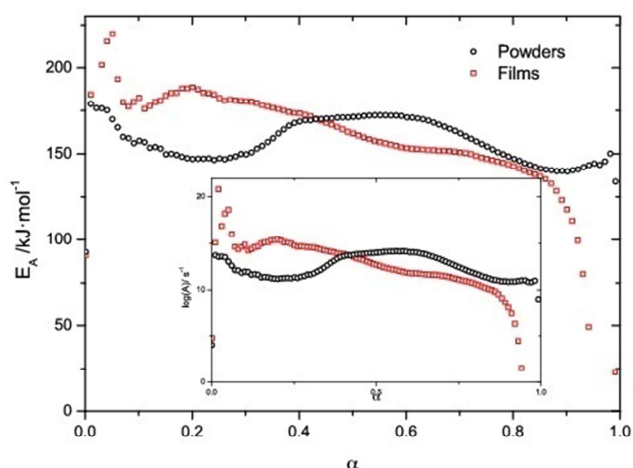


Fig. IV-10. Experimental activation energy of the thermal decomposition of $\text{Y}(\text{TFA})_3$ determined with the modified Ortega's isoconversional method [44]. The evolution at different heating rates used in the determination of the activation energy for films (squares) and powders (circles) are shown in Fig. IV-11.

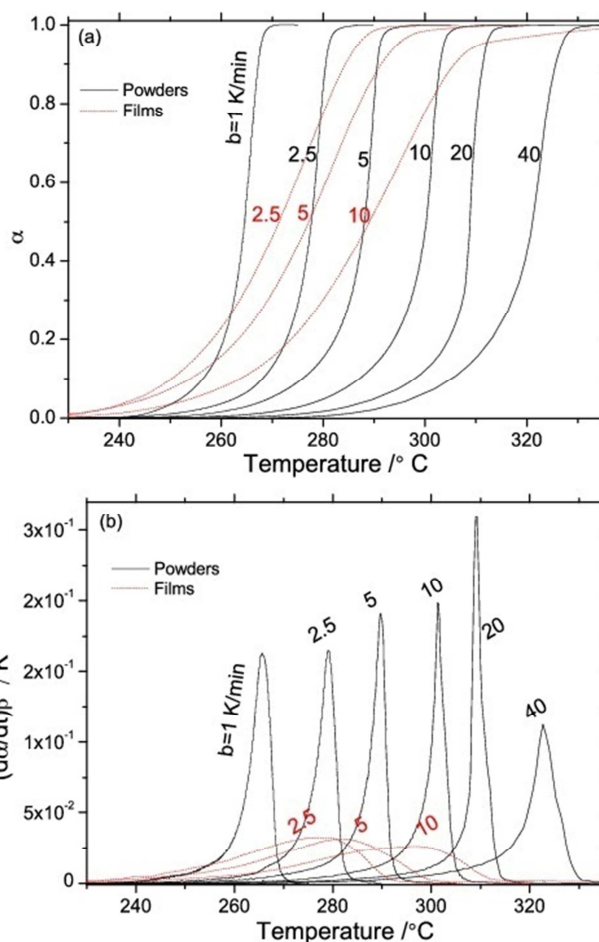


Fig. IV-11. Evolution of the thermal degradation of $\text{Y}(\text{TFA})_3$ in the form of powders (solid lines) and films (dashed lines) obtained from TG experiments performed at different heating rates. Initial masses for powders range from 17.6 mg (1 K/min) to 2.4 mg (40 K/min), while four films were measured simultaneously which resulted in an initial total mass of between 2.1 and 2.7 mg.

speed of the propagation of the combustion front is nearly independent of the sample mass and heating rate (i.e., the reaction time is nearly constant). Therefore, the kinetics is basically controlled by the onset of the reaction which is governed by the activation energy. Thus, the kinetic analysis results in a nearly constant activation energy that coincides with the actual activation energy of the reaction (see Fig. IV-10). The position of the maximum is even governed by the activation energy, so that the Kissinger method can be applied to determine the activation energy. In fact, we applied the Kissinger method (not shown) and we obtained activation energy of 165 kJ/mol, which is consistent with the isoconversional analysis shown in Fig. IV-10. Besides, contrary to $\text{Ba}(\text{TFA})_2$, $\text{Y}(\text{TFA})_3$ decomposition is governed by a single mechanisms [29], thus the isoconversional analysis of thin films, shown in Fig. IV-10, also delivers a rather constant value of the activation energy. As a result in the case of $\text{Y}(\text{TFA})_3$, the activation energy obtained from films is very similar to that of powders (Fig. IV-10) despite the fact that the actual kinetics is quite different: in films the decomposition is smooth while powders exhibit an abrupt evolution (Fig. IV-11). Thus, the occurrence of combustion does not allow the reaction mechanism to be obtained because the peak shape is totally distorted, but it does provide a rather constant activation energy that corresponds to the actual activation energy for single-step reactions. Finally, in Fig. IV-12 we have simulated the experimental cases of powders

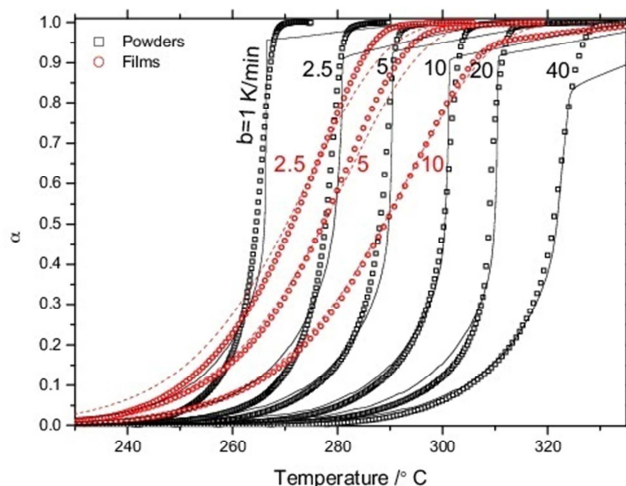


Fig. IV-12. Comparison between the experimental results plotted in Fig. IV-11 (squares correspond to powders and circles to films) and the related numerical simulations (solid lines correspond to powders and dashed lines to films). For powders the sample and crucible thermal parameters are detailed in Table IV-1 and 2. For films we have taken a thickness of $1 \mu\text{m}$ and a glass substrate 0.5 mm thick. All thermal and kinetic parameters for film coincide with those of powders except for $\lambda = 0.2 \text{ W/(mK)}$ and $A = 5.0 \times 10^{13} \text{ s}^{-1}$.

and films shown in Fig. IV-11. We wish to confirm that the different behavior is not related to the kinetic parameters but to the different geometry of powders and films. The fair agreement between numerical and experimental results supports the latter statement.

7. Conclusions

We have determined two relationships, related to heat propagation and to heat released by an exothermic reaction, that provide a criterion to establish the conditions required to prevent the formation of significant temperature gradients within a sample.

Our analysis allows a critical mass that depends on the system parameters (thermal parameters, kinetic parameters and aspect ratio) to be calculated. When the sample mass exceeds this critical mass, a temperature difference larger than 1 K appears within the sample.

Our analysis takes into account the aspect ratio; in the case of films, it is shown that the critical sample mass is several orders of magnitude larger due to the very small thickness to surface size ratio. This result evidences the fact that heat in films is very efficiently dissipated through the substrate.

We have analyzed the effect of the heat released by the reaction of the observed kinetics. We have shown that, when the sample mass exceeds the critical mass, the kinetic analysis may lead to quantitatively and qualitatively incorrect results and interpretations. However, the activation energy and pre-exponential term can still be determined at the early stages of the reaction (e.g., $\alpha < 0.1$).

Finally, in the particular case of combustion and for single-step reactions, a nearly constant activation energy and pre-exponential term are obtained from the kinetic analysis. In this case both isoconversional and Kissinger methods deliver reliable kinetic parameters.

Acknowledgements

This work was partially funded by the Spanish Programa Nacional de Materiales through projects MAT2011-28874-C02-02 and by the Generalitat de Catalunya contract No. 2009SGR-185. H. Eloussifi acknowledges the financial support of the Tunisian Ministry of Higher Education and Scientific Research.

Appendix: Conditions for heating a sample at constant rate from its surface.

Consider a sample limited by an external surface:

$$S = S_{iso} + S_{ad}, \quad (\text{A.1})$$

where subscripts "iso" and "ad" mean isothermal and adiabatic boundary conditions:

$$\begin{aligned} T(\vec{r}, t) &= T_{iso} \text{ at } S_{iso} \\ \vec{\nabla} T(\vec{r}, t) &= 0 \text{ at } S_{ad} \end{aligned} \quad (\text{A.2})$$

The sample itself is characterized by a distribution of mass density, $\rho(\vec{r})$, specific heat, $c(\vec{r})$, and thermal conductivity, $\lambda(\vec{r})$. We will show that, when S_{iso} is heated at constant rate, b :

$$T_{iso} = T_0 + b \cdot t, \quad (\text{A.3})$$

after a transient period, the whole system will acquire the same heating rate, i.e.:

$$T(\vec{r}, t) = T_0 + b[t - \tau(\vec{r})], \quad (\text{A.4})$$

where $\tau(\vec{r})$ is the time constant (tau lag) that quantifies the thermal lag between the surface and point \vec{r} . The temperature distribution, $T(\vec{r}, t)$, will be real only if it satisfies the transport equation:

$$\lambda \nabla^2 T + \text{div} \lambda \cdot \vec{\nabla} T = \rho c \frac{\partial T}{\partial t}, \quad (\text{A.5})$$

and the boundary conditions, Eq. (2). The boundary may be rewrite in terms of the tau lag:

$$\begin{aligned} \tau(\vec{r}) &= 0 \text{ at } S_{iso} \\ \vec{\nabla} \tau(\vec{r}) &= 0 \text{ at } S_{ad} \end{aligned} \quad (\text{A.6})$$

After substitution of Eq. (4) in Eq. (5), and with little calculus, we obtain the equation that $\tau(\vec{r})$ must fulfill:

$$-(\lambda \nabla^2 \tau + \text{div} \lambda \cdot \vec{\nabla} \tau) = \rho c \quad (\text{A.7})$$

The existence of a field of thermal lag values characterized by function $\tau(\vec{r})$ independent of time (and temperature and b) is only ensured if: (a) the thermal constants are temperature independent and (b) S_{ad} is really an adiabatic surface. If this surface is the free surface of the sample contained in a metallic crucible, the latter condition means that heat transport through the gas or by radiation must be zero. If this surface were not adiabatic, then it would not be possible to establish a time independent boundary condition at S_{ad} .

Appendix B. Supplementary data

Supplementary data associated with this article can be found, in the online version, at <http://dx.doi.org/10.1016/j.tca.2014.05.001>.

References

- [1] J. Farjas, N. Butchosa, P. Roura, A simple kinetic method for the determination of the reaction model from non-isothermal experiments, *J. Therm. Anal. Calorim.* 102 (2010) 615–625.
- [2] A.G. Merzhanov, V.V. Barzykin, A.S. Shteinberg, V.T. Gontkovskaya, Methodological principles in studying chemical reaction kinetics under conditions of programmed heating, *Thermochim. Acta* 21 (1977) 301–332.
- [3] S. Vyazovkin, A.K. Burnham, J.M. Criado, L.A. Pérez-maqueda, C. Popescu, N. Sbirrazzuoli, ICTAC kinetics committee recommendations for performing kinetic computations on thermal analysis data, *Thermochim. Acta* 520 (2011) 1–19.
- [4] American Society for Testing and Materials (ASTM International), Test method E698, Method for Arrhenius kinetic constants for thermally unstable materials using differential scanning calorimetry and the Flynn/Wall/Ozawa method, in: B. Annu (Ed.), *ASTM Stand.*, vol. 14.02, ASTM International, West Conshohocken PA, 2005.

- [5] S. Neuenfeld, C. Schick, Verifying the symmetry of differential scanning calorimeters concerning heating and cooling using liquid crystal secondary temperature standards, *Thermochim. Acta* 446 (2006) 55–65.
- [6] G. Höhne, W.F. Hemminger, H.J. Flammersheim, *Differential Scanning Calorimetry*, Springer, Berlin, 1996.
- [7] Y. Saito, K. Saito, T. Ataké, Theoretical analysis of peak height in classical DTA, power-compensated DSC and heat-flux DSC, *Thermochim. Acta* 107 (1986) 277–282.
- [8] M.J. Richardson, N.G. Savill, Temperatures in differential scanning calorimetry, *Thermochim. Acta* 12 (1975) 213–220.
- [9] R.L. Blaine, H.E. Kissinger, Homer Kissinger and the Kissinger equation, *Thermochim. Acta* 540 (2012) 1–6.
- [10] M.E. Patt, B.E. White, B. Stein, E.J. Cotts, Thermal time constants in differential scanning calorimetry, *Thermochim. Acta* 197 (1992) 413–424.
- [11] P. Roura, J. Farjas, Analysis of the sensitivity and sample–furnace thermal-lag of a differential thermal analyzer, *Thermochim. Acta* 430 (2005) 115–122.
- [12] M. Siniti, F. Schiets, K. Alouani, P. Claudy, Heat transfer in a disc-type DSC apparatus, *J. Therm. Anal. Calorim.* 89 (2007) 45–50.
- [13] A.W. Coats, J.P. Redfern, Thermogravimetric analysis, *Analyst* 88 (1963) 906–924.
- [14] M.E. Brown, *Introduction to Thermal Analysis*, Kluwer Academic Publishers, New York, 2004.
- [15] J. Šesták, V. Šatava, W.W. Wendlandt, The study of heterogeneous processes by thermal analysis, *Thermochim. Acta* 7 (1973) 333–334.
- [16] J.S. Crighton, F.W. Wilburn, The role of heat transfer in the production of DSC curves, *Thermochim. Acta* 203 (1992) 1–5.
- [17] S.C. Mraw, Mathematical treatment of heat flow in differential scanning calorimetry and differential thermal analysis instruments, *Rev. Sci. Instrum.* 53 (1982) 228–231.
- [18] P. Holba, J. Šesták, D. Sedmidubský, Heat transfer and phase transition in DTA experiments, in: J. Šesták, P. Šimon (Eds.), *Thermal Analysis of Micro, Nano-Non-Crystalline Materials*, Springer, Netherlands, 2013, pp. 99–133.
- [19] W.W. Wendlandt, *Thermal Analysis*, Wiley, New York, 1986.
- [20] J.P.A. Neeft, F. Hoornaert, M. Makkee, J.A. Moulijn, The effects of heat and mass transfer in thermogravimetric analysis. a case study towards the catalytic oxidation of soot, *Thermochim. Acta* 287 (1996) 261–278.
- [21] S. Vyazovkin, Evaluation of activation energy of thermally stimulated solid-state reactions under arbitrary variation of temperature, *J. Comput. Chem.* 18 (1997) 393–402.
- [22] R. Keuleers, J. Janssens, H. Desseyn, Instrument dependence and influence of heating rate, mass, ΔH , purge gas and flow rate on the difference between the experimental and programmed temperature of the instrument, *Thermochim. Acta* 333 (1999) 67–71.
- [23] T. Boddington, F. Hongtu, P.G. Laye, M. Nawaz, D.C. Nelson, Thermal runaway by thermal analysis, *Thermochim. Acta* 170 (1990) 81–87.
- [24] F.U. Buehler, J.C. Seferis, Heat diffusion analysis of the temperature distribution and phase lag build-up in TMDSC specimens, *Thermochim. Acta* 334 (1999) 49–55.
- [25] J. Šesták, P. Holba, Heat inertia and temperature gradient in the treatment of DTA peaks, *J. Therm. Anal. Calorim.* 113 (2013) 1633–1643.
- [26] J. Farjas, J. Camps, P. Roura, S. Ricart, T. Puig, X. Obradors, The thermal decomposition of barium trifluoroacetate, *Thermochim. Acta* 544 (2012) 77–83.
- [27] H. Eloussifi, J. Farjas, P. Roura, J. Camps, M. Dammak, S. Ricart, et al., Evolution of yttrium trifluoroacetate during thermal decomposition, *J. Therm. Anal. Calorim.* 108 (2012) 589–596.
- [28] H. Eloussifi, J. Farjas, P. Roura, S. Ricart, T. Puig, X. Obradors, et al., Thermal decomposition of barium trifluoroacetate thin films, *Thermochim. Acta* 556 (2013) 58–62.
- [29] H. Eloussifi, J. Farjas, P. Roura, S. Ricart, T. Puig, X. Obradors, et al., Thermoanalytical study of the decomposition of yttrium trifluoroacetate thin films, *Thin Solid Films* 545 (2013) 200–204.
- [30] P. Roura, D. Sanchez-Rodríguez, J. Farjas, Measurement by differential scanning calorimetry of specific heat capacity variation due to crystallization: application to amorphous silicon, *Thermochim. Acta* 522 (2011) 161–165.
- [31] M. Hu, D. Yu, J. Wei, Thermal conductivity determination of small polymer samples by differential scanning calorimetry, *Polym. Test.* 26 (2007) 333–337.
- [32] R. Melling, F.W. Wilburn, R.M. McIntosh, Study of thermal effects observed by differential thermal analysis. Theory and its application to influence of sample parameters on a typical DTA curve, *Anal. Chem.* 41 (1969) 1275–1286.
- [33] S. Vyazovkin, Kinetic concepts of thermally stimulated reactions in solids: a view from a historical perspective, *Int. Rev. Phys. Chem.* 19 (2000) 45–60.
- [34] J. Fort, D. Campos, J.R. González, J. Velayos, Bounds for the propagation speed of combustion flames, *J. Phys. A: Math. Gen.* 37 (2004) 7185.
- [35] W.H. Press, B.P. Flannery, S.A. Teukolsky, W.T. Vetterling, *Numerical Recipes in C: The Art of Scientific Computing*, Cambridge University Press, Cambridge, 1994.
- [36] M.F. Ashby, *Materials Selection in Mechanical Design*, Butterworth-Heinemann Limited, Oxford, 1999.
- [37] D. Sanchez-Rodríguez, J. Farjas, P. Roura, S. Ricart, N. Mestres, X. Obradors, et al., Thermal analysis for low temperature synthesis of oxide thin films from chemical solutions, *J. Phys. Chem. C* 117 (2013) 20133–20138.
- [38] J. Farjas, P. Roura, Simple approximate analytical solution for nonisothermal single-step transformations: kinetic analysis, *AIChE J.* 54 (2008) 2145–2154.
- [39] H.E. Kissinger, Reaction kinetics in differential thermal analysis, *Anal. Chem.* 29 (1957) 1702–1706.
- [40] P. Roura, J. Farjas, Analytical solution for the Kissinger equation, *J. Mater. Res.* 24 (2009) 3095–3098.
- [41] J. Farjas, D. Sanchez-Rodríguez, H. Eloussifi, R.C. Hidalgo, P. Roura, S. Ricart, et al., Can we trust on the thermal analysis of metal organic powders for thin film preparation? *MRS Proc.* 1449 (2012) 13–18.
- [42] M.E. Brown, M. Maciejewski, S. Vyazovkin, R. Nomen, J. Sempere, A. Burnham, et al., Computational aspects of kinetic analysis: Part A: The ICTAC kinetics project-data, methods and results, *Thermochim. Acta* 355 (2000) 125–143.
- [43] A. Ortega, A simple and precise linear integral method for isoconversional data, *Thermochim. Acta* 474 (2008) 81–86.
- [44] J. Farjas, P. Roura, Isoconversional analysis of solid state transformations. A critical review. Part I. Single step transformations with constant activation energy, *J. Therm. Anal. Calorim.* 105 (2011) 757–766.
- [45] H. Eloussifi, J. Farjas, P. Roura, M. Dammak, Non-isothermal model-free predictions, *J. Therm. Anal. Calorim.* 108 (2012) 597–603.
- [46] S. Vyazovkin, C.A. Wight, Kinetics in solids, *Annu. Rev. Phys. Chem.* 48 (1997) 125–149.
- [47] J.P. Elder, Multiple reaction scheme modeling. I. Independent and competitive 1st order reactions, *J. Therm. Anal. Calorim.* 29 (1984) 1327–1342.
- [48] J. Farjas, P. Roura, Isoconversional analysis of solid state transformations. A critical review. Part II. Complex transformations, *J. Therm. Anal. Calorim.* 105 (2011) 767–773.

V. Determination of thermal conductivity of powders in different atmospheres by differential scanning calorimetry

Determination of thermal conductivity of powders in different atmospheres by differential scanning calorimetry

Daniel Sánchez-Rodríguez · Joan Pere López-Olmedo ·
Jordi Farjas · Pere Roura

Received: 17 September 2014 / Accepted: 11 January 2015
© Akadémiai Kiadó, Budapest, Hungary 2015

Abstract We have developed a new method to measure the thermal conductivity of powders by differential scanning calorimetry that works with masses in amounts as low as tens of mg. The method is based on that used by Camirand to determine the thermal conductivity of materials in the form of thin sheets but introducing a hemispherical pan to contain powders in such a way that the issue of heat transfer is reduced to a one-dimensional problem. The modification of the method was successfully validated on obtaining identical results in determining the thermal conductivity of a commercial silicone with both Camirand's method and the modified method. We have also tested our method with materials that, in bulk, cover a wide range of thermal conductivities and have performed the experiments with several atmospheres and reference metals. The results are consistent with already published general trends in that they confirm that thermal conductivity of powders is mainly governed by thermal conduction through the surrounding gas.

Keywords Thermal conductivity · Powders · DSC

Introduction

At present, the thermal conductivity of powders is commonly determined from measurements of their thermal diffusivity with the modified transient plane source method (MTPS) [1]

D. Sánchez-Rodríguez (✉) · J. Farjas · P. Roura
GRMT, Department of Physics, University of Girona,
Campus Montilivi, Edif. PII, 17071 Girona, Catalonia, Spain
e-mail: daniel.sanchez@udg.edu

J. P. López-Olmedo
UAT, Serveis Tècnics de Recerca, University of Girona,
Campus Montilivi, Edif. PII, 17071 Girona, Catalonia, Spain

where powders are bound inside a cylinder and heated by an axial heat source. This method, used in commercial apparatuses, requires an independent measurement of the material's heat capacity and works with a large number of powders.

Differential scanning calorimetry (DSC) is probably the most widely used thermoanalytical technique. Among many other applications, it is used for the measurement of the heat capacity of solid or liquid substances [2] and the thermal conductivity of solids. There are various established methods to measure thermal conductivity with DSC using either the modulated temperature mode [3, 4] or the standard mode [5–8], but none are suitable when the sample is in the form of uncompressed powders.

Camirand [5] and, before him, Flynn and Levin [6] developed a simple method to measure the thermal conductivity of flat materials with conventional DSC, which, in this paper, we will show can be modified to measure the thermal conductivity of powders. Our method (and Camirand's method), unlike the one based on the modulated temperature mode, determines the thermal conductivity at discrete temperature values that can only correspond to the melting points of the reference metals. On the other hand, there are no limitations on the temperature range beyond those of the DSC apparatus itself, although an upper limit could be set by the crucible. Our contribution is to use a crucible containing powders in such a way that heat transfer is reduced to a one-dimensional problem. In so doing, we are able to obtain the thermal resistance of powders, using just tens of milligrams of a sample, by melting a reference metal as Camirand does with sheet materials.

Experimental

All thermal conductivity experiments were performed with a Mettler Toledo DSC822 and high purity spherical

reference metals (radii in the 1–2 mm range) were used. A non-commercial cylindrical aluminum crucible with a hemispherical cavity (Fig. V-1) with an inner radius of 2.5 mm was made by plastic deformation. The outer radius and height were reduced by machining until the diameter was equal to that of a standard crucible in order to avoid thermal bridges between the crucible and the apparatus. No reference pan was used. The gas flow rate was set at 40 mL min^{-1} , and nitrogen, argon and helium, all of high purity, were selected because of their differences in thermal conductivity. A constant heating rate of $10 \text{ }^\circ\text{C min}^{-1}$ was maintained for the systematic experiments although we modified the heating rate from 5 to $20 \text{ }^\circ\text{C min}^{-1}$ for method validations. The DSC signal was calibrated for the three gases by measuring the area of the melting peaks.

High purity (above 99 %) commercially available alumina, iron, tin oxide and Ba trifluoroacetate powders were used. Particles morphology and size were very different as shown in the scanning electrons micrographs (SEM) of Fig. V-2. The thermal conductivity of these materials in bulk form is set out in Table V-1. The powders were gently pressed inside the crucible.

Method description

The hemispherical crucible was completely filled with the powder being tested, and a small reference metal sphere was sunk inside the powder until its center was concentric to the crucible cavity (Fig. V-1). The filled crucible was heated in the DSC apparatus at a constant heating rate until the metal melted. The slope of the melting peak, depicted in Fig. V-3, corresponds to the following formula:

$$s_p = \frac{1}{R + R_c + R_p}, \quad (1)$$

where R , R_c and R_p are the sensor resistance, the contact resistance between the crucible and the DSC sensor disk

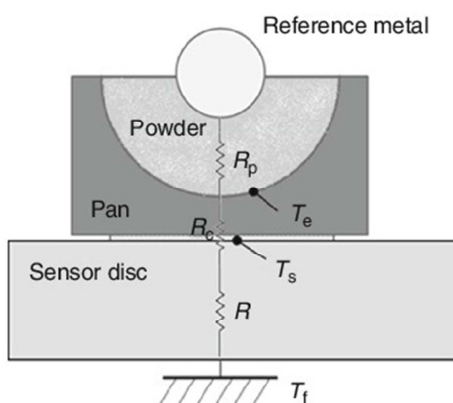


Fig. V-1 Geometric appearance of the hemispherical pan placed on the sensor disk. The thermal resistances of the system are indicated (R : sensor, R_c : contact resistance, R_p : powder)

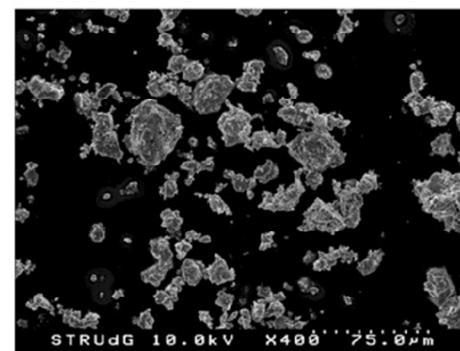
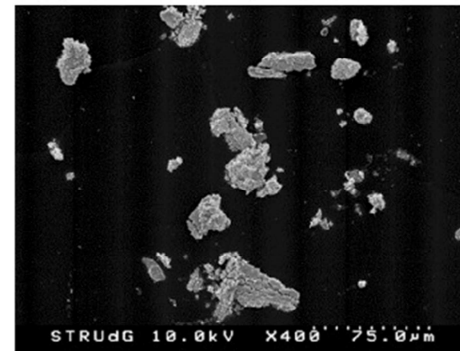
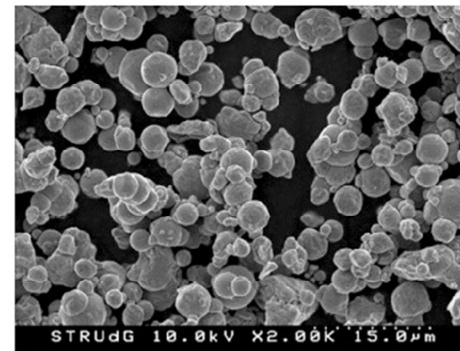
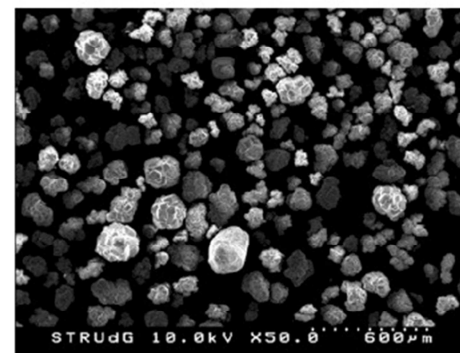


Fig. V-2 From top to bottom: SEM micrographs of the alumina, iron, tin oxide and Ba(TFA)₂ powders studied in this paper

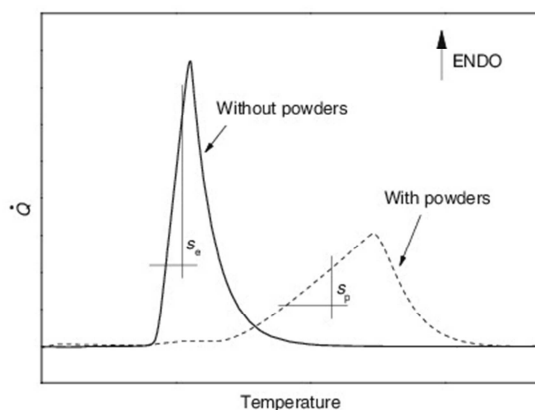
and the powder's resistance, respectively (see "Appendix").

A second DSC curve was then recorded at the same heating rate without the powder in the crucible. The metal was flattened on the bottom of the crucible cavity to optimize the thermal contact between the metal and the

Table V-1 Thermal conductivity of the powders measured in this paper at the melting point of In (156.6 °C) in N₂

Material	Thermal conductivity/W °C ⁻¹ m ⁻¹	
	Bulk	Powders
Al ₂ O ₃	30	0.126
Fe	80.4	0.1
SnO ₂	40	0.059
Ba(CF ₃ CO ₂) ₃	0.3	0.08

The bulk conductivities (at 25 °C) are taken from public sources


Fig. V-3 Typical DSC melting curves with and without powders. The thermal resistance of the powders is obtained from the S_e and S_p slopes

crucible. Similarly to the previous case, the slope of the melting peak (S_e) (Fig. V-3) corresponds to the formula:

$$S_e = \frac{1}{R + R_c} \quad (2)$$

Equations (1) and (2) allow the powder's thermal resistance to be obtained and the spherical symmetry makes it possible to calculate the thermal conductivity:

$$\kappa = \frac{1}{2\pi R_p} \cdot \left(\frac{1}{r_i} - \frac{1}{r_e} \right), \quad (3)$$

where r_i is the radius of the reference metal sphere and r_e is the radius of the hemispherical cavity.

Results

Method validation

Several experiments have been performed to check the correctness and reproducibility of the method. In Table V-2, we summarize the heating rates and indium sphere radii used to validate the method on tin oxide powders. We observe, as expected, that all of these experiments gave thermal conductivity values that were almost identical when the experimental conditions were identical except for the heating rate. The 10 % deviation observed when a larger radius was tested, can be explained by an increase in the density of the powder used. Despite the independence of the heating rate, low heating rates are preferred as DSC curves usually have better defined melting slopes in these conditions.

Finally, the thermal conductivity of a commercial silicone that can be cast from a viscous state and cured at a moderate temperature of 80 °C was measured. Once cured, this silicone remained stable beyond the melting point of indium and so was suitable to validate our method through comparison with Camirand's. A 2-mm-thick and 5-mm-diameter flat disk was made for that purpose. Within experimental accuracy, which was essentially limited by the thickness measurement (± 0.05 mm), we obtained the same thermal conductivity for the two methods ($0.103 \text{ W } ^\circ\text{C}^{-1} \text{ m}^{-1}$). It is also worth noting that the conductivity of the silicone was similar to that of the powders (see "Conductivity of powders" section). This means that we have validated our method just at the conductivity values of interest.

Conductivity of powders

The thermal conductivity of several powders was measured in N₂ at the melting point of In (156.6 °C), and the results

Table V-2 Parameters and results of experiments carried out with powders in N₂ at the melting point of In (β is the heating rate)

	$\beta/^\circ\text{C min}^{-1}$	Metal sphere radius/mm	Melting slope/mW °C ⁻¹	Thermal conductivity/W °C ⁻¹ m ⁻¹	Relative density/%
SnO ₂	5	1.19	0.9	0.06	9
SnO ₂	10	1.19	0.89	0.059	9
SnO ₂	20	1.19	0.89	0.059	9
SnO ₂	10	1.75	2.34	0.066	12.5
Al ₂ O ₃	10	1.21	1.85	0.126	29.5
Fe	10	1.04	0.71	0.1	50.1
Ba(CF ₃ CO ₂) ₃	10	1.04	0.8	0.08	42 ^a

^a Assuming a theoretical density of 3.5 g/cm³

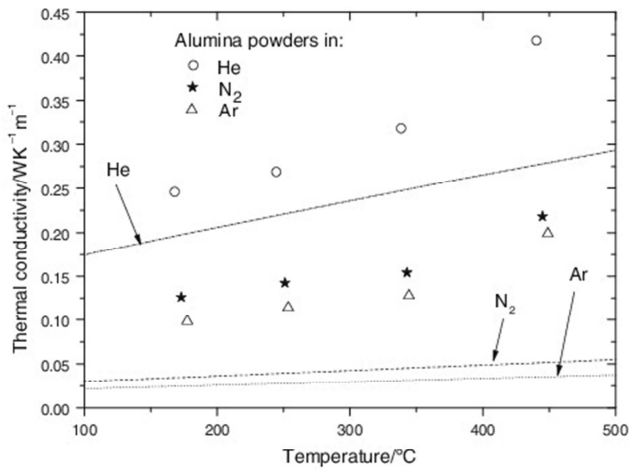


Fig. V-4 Temperature dependence of the thermal conductivity of alumina powders in several gases (*points*). The thermal conductivity of He, N₂ and Ar are shown for comparison (*lines*)

are summarized in Table V-1. It is worth noting that, in contrast with their bulk counterparts, powders have very similar conductivities ($\pm 30\%$ variation between powders) and that these are much lower than in bulk (values at 25 °C).

In Fig. V-4, we have plotted the thermal conductivity of alumina powders for three different atmospheres at the melting points of indium, tin, lead and zinc and have also plotted the thermal conductivity of nitrogen, argon and helium for purposes of comparison. A relative density value was maintained between 27 and 30 % for all experiments. It is important to highlight, as is seen in the figure, that there is a clear and direct relationship between the thermal conductivity of the alumina powders and the surrounding gas. The conductivity of powders increases with increased gas conductivity and temperature. In addition, the absolute values of powders are higher but similar to those of the surrounding atmosphere.

Finally, it is interesting to note that there are significant differences in the melting temperature when the reference metal is melted with and without powders contained in the crucible (Fig. V-3). The relationship between this delay and the thermal conductivity of the powders will be studied in future work.

Discussion

Since Klemensiewicz [9] reported the unexpectedly low thermal conductivities of powders, this surprising behavior has been confirmed by many other authors [10–13]. All

these authors have found thermal conductivities of powders that are similar to those of the surrounding gas, irrespectively of their bulk conductivity. These general trends agree with our own results as presented in Fig. V.4 and Table V-2.

In view of the very low thermal conductivity of powders when compared to their values in bulk (Table V-1), one must conclude that the network of solid particles is very inefficient for heat transport. In the absence of any gas, the thermal resistance between particles at the points of contact must be very high. So, heat transport through the gas in the interstices between the particles is essential to understand the measured values. We can take the ratio $\kappa_{\text{GAS}}/\kappa$ to qualitatively evaluate the gas contribution to heat transport. At any temperature, this ratio reaches its maximum value for He (Fig. V-4) as expected because its conductivity is the highest among the gases we have tested.

Conclusions

It has been demonstrated that it is possible to determine the thermal conductivity of all kinds of powders with a DSC apparatus by modifying Camirand's method. In our method, a reference metal sphere is sunk up to its equator in a hemispherical crucible completely filled with the desired powders. This method is particularly attractive as DSC is widely available and has the advantage of only requiring a small amount of mass.

We have tested our method with materials that, in bulk, cover a wide range of thermal conductivities and have performed the experiments with several gases and reference metals to evaluate the contribution of the gas. The results are consistent with the general trends already published in the literature in that they confirm that the thermal conductivity of powders is mainly governed by thermal conduction through the surrounding gas.

Acknowledgements This work was partially funded by the Spanish Programa Nacional de Materiales through projects MAT2011-28874-C02-02 and by the Generalitat de Catalunya contract No. 2009SGR-185. The authors wish to thank the University of Girona for the PhD fellowship granted to Daniel Sánchez-Rodríguez and for the use of the thermal analysis facilities (Serveis Tècnics de Recerca).

Appendix: Slope of the DSC signal during melting

During melting, the metal reference remains at the melting temperature, T_M , whereas the DSC furnace is heated at a constant heating rate, β . Let us first demonstrate that any point r of the powder contained in the hemispherical holder

(Fig.V-1) will experience a constant heating rate according to the formula:

$$T(r, t) = f(R) + \frac{\beta_c}{R_c} R t, \tag{4}$$

where t is time, f is a time-independent function and R is the thermal resistance of the powder inside the radius r , i.e.:

$$R = \frac{1}{2\pi\kappa} \left(\frac{1}{r_i} - \frac{1}{r} \right), \tag{5}$$

where κ is the powder thermal conductivity. Notice that the heating rate of the powder varies from zero at r_i to its maximum value β_c at r_e .

We must simply verify that $T(r,t)$ of Eq. (4) satisfies the heat transport equation that, given the spherical symmetry of the system, can be written as:

$$\frac{2}{r} \frac{\partial T}{\partial r} + \frac{\partial^2 T}{\partial r^2} = \frac{\rho c}{\kappa} \frac{\partial T}{\partial t}, \tag{6}$$

or, substituting r by R in the partial derivatives:

$$\frac{1}{2\pi r^4} \frac{\partial^2 T}{\partial R^2} = \rho c \frac{\partial T}{\partial t}, \tag{7}$$

where ρ and c are the density and specific heat of the powder, respectively. This verification is straightforward after the introduction of Eq. (4) into (7), and is left for the reader.

Once demonstrated that the powder in contact with the pan (at $r = r_e$) is heated at a constant rate, the value of β_c will be calculated with the assumption that we can neglect both the pan resistance and its contact resistance with the DSC sensor (i.e. $T_s = T_e$ —see Fig.V-1). We must simply impose a power measured by the DSC, \dot{Q}_{DSC} equal to the heat that enters into the powder through the pan’s inner surface, \dot{Q}_c . \dot{Q}_{DSC} can be easily calculated through the formula:

$$\dot{Q}_{DSC} = \frac{T_{REF} - T_e}{R}, \tag{8}$$

where R is the thermal resistance of the DSC sensor, T_{REF} is the reference temperature that changes at the programmed heating rate:

$$T_{REF} = T_0 + \beta t, \tag{9}$$

and T_e is given by Eq. (4) at $r = r_e$. We obtain:

$$\dot{Q}_{DSC} = A + \frac{\beta - \beta_c}{R} t, \tag{10}$$

where A is time-independent. On the other hand, \dot{Q}_c is proportional to the temperature gradient at r_e :

$$\dot{Q}_c = 2\pi r_e^2 \kappa \left. \frac{\partial T}{\partial r} \right|_{r_e}. \tag{11}$$

Introduction of Eqs. (4) and (5) into Eq. (11) gives:

$$\dot{Q}_c = B + \frac{\beta_c}{R_c} t, \tag{12}$$

where B is time-independent. Now, the condition $\dot{Q}_{DSC} = \dot{Q}_c$ delivers the value of β_c :

$$\beta_c = \frac{R_c}{R + R_c} \beta. \tag{13}$$

And, finally, the slope of the DSC signal can be obtained after the substitution of β_c in Eq. (10):

$$\frac{d\dot{Q}_{DSC}}{dT_{REF}} = \frac{d\dot{Q}_{DSC}}{d(\beta t)} = \frac{1}{R_{DSC} + R_c}. \tag{14}$$

If the contact resistance between the pan and the DSC sensor were not negligible, the result would be $1/(R + R_c + R_e)$.

References

- Novichenok LN, Ovchinniko SM, Marshak VA. Thermal conductivity probe e.g. for complex liquids and powders—has cylinder wound alternately with heater and resistance thermometer turns. 1986; Patent n.SU1264053-A.
- Roura P, Sanchez-Rodriguez D, Farjas J. Measurement by differential scanning calorimetry of specific heat capacity variation due to crystallization: application to amorphous silicon. *Thermochim Acta.* 2011;522:161–5.
- Marcus SM, Blaine RL. Thermal-conductivity of polymers, glasses and ceramics by modulated DSC. *J Therm Anal Calorim.* 1994;243:231–9.
- Kalogiannakis G, Van Hemelrijck D, van Assche G. Measurements of thermal properties of carbon/epoxy and glass/epoxy using modulated temperature differential scanning calorimetry. *J Compos Mater.* 2004;38:163–75.
- Camirand CP. Measurement of thermal conductivity by differential scanning calorimetry. *Thermochim Acta.* 2004;417:1–4.
- Flynn JH, Levin DM. A method for the determination of thermal conductivity of sheet materials by differential scanning calorimetry. *Thermochim Acta.* 1988;126:93–100.
- Tavman I, Aydogdu Y, Kök M, Turgut A, Ezan A. Measurement of heat capacity and thermal conductivity of HDPE/expanded graphite nanocomposites by differential scanning calorimetry. *Arch Mater Sci Eng.* 2011;50:56–60.
- Hakvoort G, Vanreijen LL, Aartsen AJ. Measurement of the thermal conductivity of solid substances by DSC. *Thermochim Acta.* 1985;93:317–20.
- Klemensiewicz Z. Thermal conductivity of powders. *Nature.* 1949;164:589.
- Huang L, El-Genk MS. Thermal conductivity measurements of alumina powders and molded Min-K in vacuum. *Energy Convers Manag.* 2001;42:599–612.
- Ming Y, Purewal J, Liu D, Sudik A, Xu Ch, Yang J, Veenstra M, Rhodes K, Soltis R, Warner J, Gaab M, Müller U, Siegel DJ. Thermophysical properties of MOF-5 powders. *Microporous Mesoporous Mater.* 2014;185:235–244.
- Huang BL, Ni Z, Millward A, McGaughey AJH, Uher C, Kaviani M, Yaghi O. Thermal conductivity of a metal-organic framework (MOF-5): part II. Measurement. *Int J Heat Mass Transf.* 2007;50:405–11.
- Mullokanov RL. *J Tech Phys. U.S.S.R.,* 1947; 17:1149 (Phys. Abstr., 1432 (1947)).

VI. Thermal explosion: When is a solid-state self-sustained reaction front formed? The Frank-Kamenetskii criterion revisited

Thermal explosion: When is a solid-state self-sustained reaction front formed? The Frank-Kamenetskii criterion revisited.

D. Sánchez-Rodríguez, J. Farjas*, P. Roura.

GRMT, Department of Physics, University of Girona, Campus Montilivi, Edif.PII, E17071 Girona, Catalonia, Spain

VI.1. Abstract

Knowing the conditions for a system to experience combustion is of utmost importance for several applications. We analyzed the condition needed for a thermal explosion to occur in a solid sample reacting without any gas exchange with its surroundings. We have developed a simple modification that allows us to extend the Frank-Kamenetskii relationship to include continuous heating systems and cylindrical reactors without limiting its dimensions and at the same time significantly improving its accuracy. This modification consists on replacing the Frank-Kamenetskii constant parameter by a parameter that depends on the enthalpy, temperature program and geometrical aspect ratio. This new analytical solution is validated with numerical simulations and experiments. The parameter range explored numerically covers most practical situations. The relationship obtained provides a straightforward calculation of the critical mass for a thermal explosion to occur as a function of the system parameters: density, thermal diffusivity, activation energy, temperature and geometry. Finally, in the supplementary material we include a description of the source code and the numerical method developed.

**VII. Self-propagating high-temperature synthesis
of LaMO_3 perovskite-type oxide using
heteronuclear cyano metal complex precursors**

Self-propagating high-temperature synthesis of LaMO₃ perovskite-type oxide using heteronuclear cyano metal complex precursors.

Daniel Sánchez-Rodríguez,^{1*} Hiroki Wada,² Syuhei Yamaguchi,² Jordi Farjas,¹ and Hidenori Yahiro^{2*}

¹*GRMT, Department of Physics, University of Girona, Campus Montilivi, Edif. PII, E17071 Girona, Catalonia, Spain*

²*Department of Materials Science and Biotechnology, Graduate School of Science and Engineering, Ehime University, Matsuyama 790-8577, Japan*

VII.1. Abstract

The decomposition of La[Fe(CN)₆] and La[Co(CN)₆] under different atmospheres has been analyzed by thermogravimetry (TG) and differential thermal analysis (DTA). In addition, the decomposition temperature at different sample locations was monitored for sample masses around 2 g of La[Fe(CN)₆] and La[Co(CN)₆], when they were calcined for 1 h at temperatures ranging from 200 to 400 °C in a controlled gas-flow system. Results showed that, for sample large enough of these cyano complex precursors undergo combustion when are decomposed under oxygen atmosphere. X-ray diffraction revealed that perovskite-type oxides crystallize due to the overheating of the process. As a result, it has been possible to produce LaFeO₃ and LaCoO₃ perovskite-type oxide powders by SHS under oxygen atmosphere using La[Fe(CN)₆] and La[Co(CN)₆] as a precursor. The effect of the ignition temperature has been investigated. The specific surface area of the perovskite-type oxides produced via SHS using heteronuclear cyano metal complex as a precursor is up to 2 orders of magnitude higher than that of other LaMO₃ produced using the same technique but obtained from other type of precursors.

Keywords: Combustion synthesis, SHS, heteronuclear cyano complex precursor, Perovskite-type oxide, LaMO₃

VII.2. Introduction

Perovskite-type oxide, ABO_3 , has attracted much attention in the environmental-friendly catalytic systems. Up to date, the perovskite-type oxides have been reported to exhibit high catalytic activity for oxidations of hydrocarbon^{1,2} and chlorinated volatile organic compounds³, and decomposition of NO ⁴⁻⁶. In addition, the perovskite-type oxides have been widely investigated to be employed as electrode materials⁷⁻¹⁰ and sensing materials¹¹⁻²¹.

The preparation method of perovskite-type oxide catalyst has been progressively improved. Traditionally, perovskite-type oxides were prepared by solid state reaction of oxides and/or carbonates²²⁻²⁴. However, such a traditional method possesses the disadvantages of long processing time, low surface area, large particle size, and limited degree of chemical homogeneity. In 1967, Merzhanov et al.²⁵ reported the self-propagating high temperature synthesis (SHS) method which takes advantage of a combustion reaction in order to synthesize advanced materials. Most of the heat required for the synthesis is provided by the reaction itself. Therefore, its treatment temperature and the processing time are significantly lower than those of conventional preparation routes. One can also expect to produce very fine and crystalline perovskite-type oxide powders by using this SHS method²⁶⁻²⁸. Other combustion techniques are widely used to synthesize solid catalyst²⁹⁻³⁰. Among them, the solution combustion synthesis (SCS) method is used to synthesize perovskite-type oxides³¹. In this technique, the liquid solution of a metal salt with a solvent as a fuel is heated until combustion occurs. Additionally, it is pertinent to remark that the SHS method differs substantially from the SCS method including the use of an ignition mechanism which heats locally the sample instead of heating the sample uniformly until volumetric combustion occurs³².

The thermal decomposition of heteronuclear cyano metal complex (CN method) is also used to prepare perovskite-type oxides because of their similar structure. It was introduced in 1968 by Gallager but it must be emphasized the extensive study carried out by Sadaoka and co-workers in the 1990s^{19,33-39}. In these papers, the preparation of perovskite-type oxides $LaFeO_3$ and $LaCoO_3$ from coordination polymer precursors, $La[Fe(CN)_6] \cdot 5H_2O$, and $La[Co(CN)_6] \cdot 5H_2O$ calcined in a gas-flow system at several conditions, such as temperature, time, and atmosphere, has been investigated. These studies revealed that under oxygen atmosphere, both precursors decompose by a combustion process in which a solid-state self-sustained reaction transforms progressively the sample into the desired perovskite-type oxide. Reaction is not homogenous over the sample but it is confined in a combustion front. This result opens

the door to the decomposition of heteronuclearcyano metal complex for the synthesis of perovskite-type oxides via SHS.

In this paper we analyze the synthesis of LaFeO_3 and LaCoO_3 perovskite-type oxides via SHS using heteronuclear cyano metal complex as a precursor. Results will be compared with those of similar perovskite-type oxides obtained via SHS using a mixture of different powders as a precursor^{26,27}.

VII.3. Experimental details

Commercial compounds, $\text{La}(\text{NO}_3)_3 \cdot 6\text{H}_2\text{O}$ (Wako, 99.5%), $\text{K}_3[\text{Fe}(\text{CN})_6]$ (Hayashi, 99%) and $\text{K}_3[\text{Co}(\text{CN})_6]$ (Sigma-Aldrich, 99%), were used without further purification. $\text{La}[\text{Fe}(\text{CN})_6] \cdot 5\text{H}_2\text{O}$ as a precursor of perovskite-type oxide, LaFeO_3 , was precipitated immediately after mixing the appropriate amounts of $\text{La}(\text{NO}_3)_3 \cdot 6\text{H}_2\text{O}$ and $\text{K}_3\text{Fe}(\text{CN})_6$ aqueous solution at room temperature under continuous stirring. By a similar way, $\text{La}[\text{Co}(\text{CN})_6] \cdot 5\text{H}_2\text{O}$ precursor was obtained from $\text{La}(\text{NO}_3)_3 \cdot 6\text{H}_2\text{O}$ and $\text{K}_3\text{Co}(\text{CN})_6$ mixed solutions. According to the method previously reported by Traversa et al.³⁷, the resulting precipitates were collected by suction filtration, washed with deionized water, ethanol and diethyl ether, and then finally dried in air at 50°C.

For systematic analysis, cyano complex precursors were calcined for 1 h at several treatment temperatures ranging from 200 to 400 °C in a gas-flow system using an electric furnace and alumina pipe (Fig. 1a); the samples were exposed to several gas atmospheres such as oxygen, air and nitrogen atmospheres. The flow rate of each gas was set at 50 mL·min⁻¹.

Perovskite-type oxides were obtained by SHS after preheating the prepared cyano complex precursor at several treatment temperatures from room temperature up to 150 °C using the same gas-flow system. The schematic view of the system is depicted in Fig.1b. A nichrome wire connected to a voltage slider was placed on the top of one of the extremes of the samples as combustion ignitor. After the samples were heated to desired temperature, 10 V was applied to ignitor for several seconds until a combustion front was set. In this experiments, oxygen was introduced with 50 mL·min⁻¹ of gas flow rate.

Thermogravimetric (TG) and differential thermal analysis (DTA) experiments were performed simultaneously with a Shimadzu DTG-60E. Powder XRD patterns were obtained by a Rigaku MiniFlex II diffractometer using $\text{CuK}\alpha$ radiation. BET analysis (Belsorp-mini, BEL JAPAN)

was performed to determine the specific surface area by measuring the adsorption-desorption capacity using N_2 adsorbent at $-196^\circ C$.

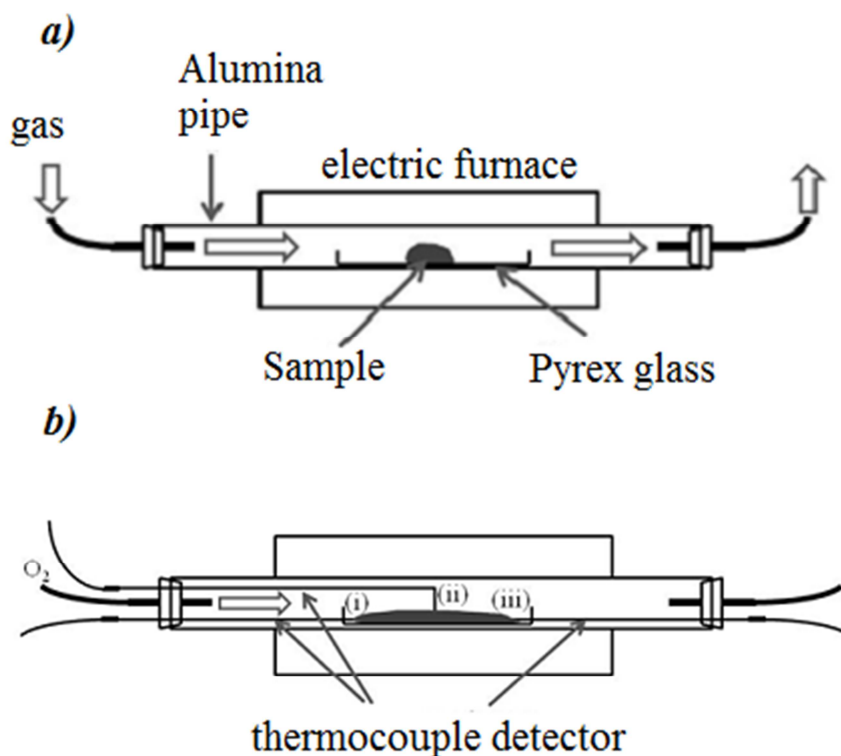


Figure VII-1. The apparatus of gas-flow system (a) and the locations of thermocouple detectors at on the sample, such as entrance (i), middle (ii), and exit sites (iii) (b).

VII.4. Results and discussion

VII.4.1. Thermal analysis of the decomposition of $La[Fe(CN)_6]$ and $La[Co(CN)_6]$

Figure VII-2 and Figure VII-3 show TG curves of $La[Fe(CN)_6]$ and $La[Co(CN)_6]$ with different sample masses, respectively. These TG experiments were carried out in flowing oxygen (a), air (b), and nitrogen (c). The decomposition process of $La[Fe(CN)_6]$ and $La[Co(CN)_6]$ was faster when the sample mass was increased under oxidant atmosphere (see Figure VII-2(a,b) and Figure VII-2(a,b), respectively). Later on it is shown that this behavior is associated to a sample overheating due to an exothermic reaction for oxidation of cyano groups in samples. A similar behavior has been reported before in the decompositions of other metalorganic powders^{40,41}. In the particular case of pure oxygen atmosphere, the extremely abrupt decomposition curve associated with higher sample masses is due to the sample local overheating leads to a thermal runaway, as it will be shown in the following. In the presence of oxygen, all

La[Co(CN)₆] samples but with the lowest mass (0.72 mg) exhibit the abrupt mass loss characteristic of the occurrence of a thermal runaway. This behavior is related to the fact that the critical mass for combustion is lower in the case of La[Co(CN)₆] and it is too small to be accurately analyzed with our TG. Besides, although the reaction is also exothermic under nitrogen atmosphere, no overheating is possible because heat removal through diffusion prevails over the heat evolved from the reaction. By increasing the thickness of sample powder, heat removal is slowed down. Although extremely large, theoretically⁴² it must be a critical mass in which thermal explosion is possible even in the case of nitrogen atmosphere.

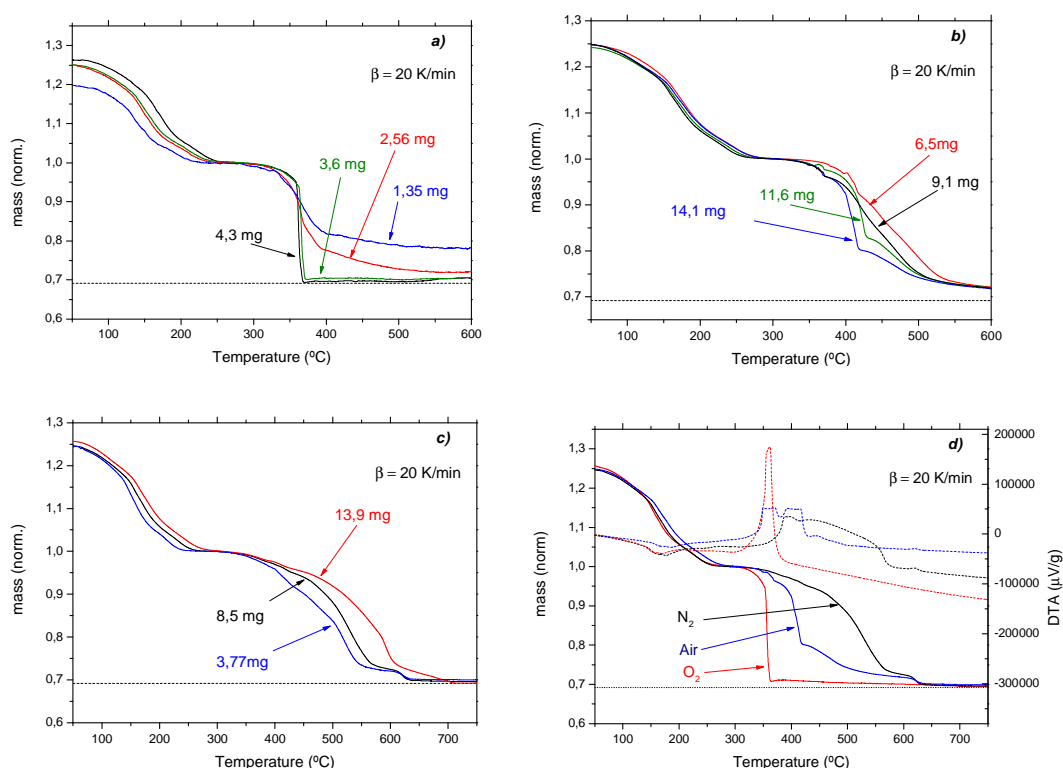


Figure VII-2. Evolution of the thermal decomposition of La[Fe(CN)₆] under O₂ (a), air (b) and N₂ (c) for different sample masses. Plot (d) shows a comparison of the characteristic thermal decomposition for high sample masses under different atmospheres. Horizontal dotted line indicates the mass of pure LaFeO₃.

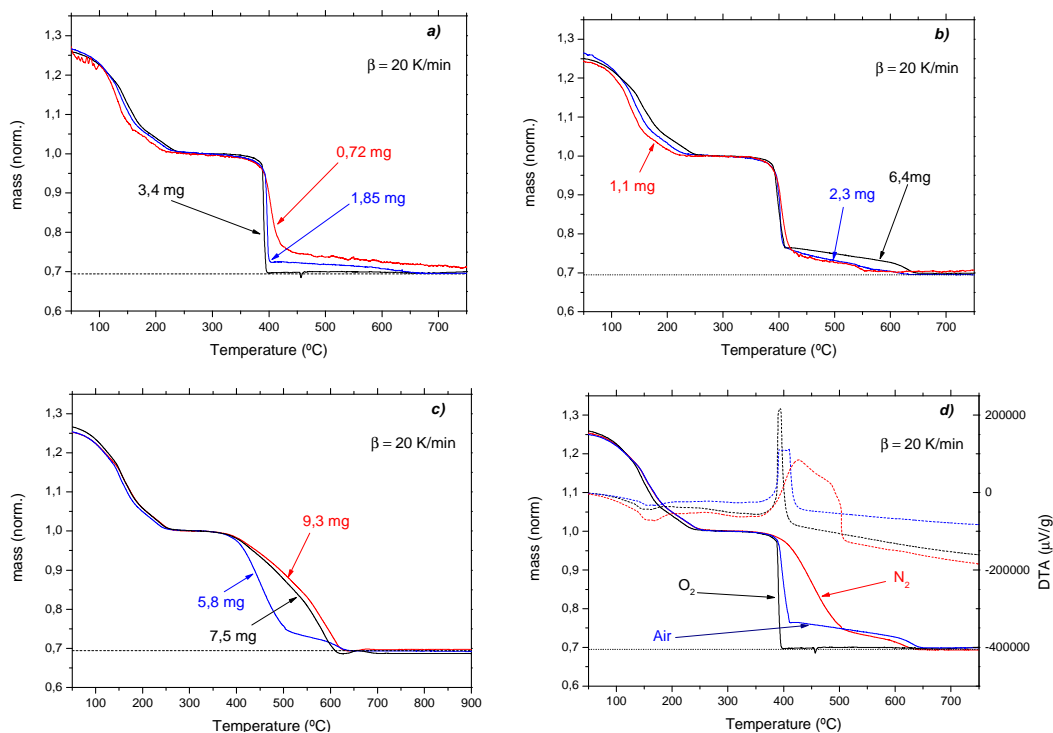


Figure VII-3. Evolution of the thermal decomposition of La[Co(CN)₆] under O₂ (a), air (b) and N₂ (c) for different sample masses. Plot (d) shows a comparison of the characteristic thermal decomposition for high sample masses under different atmospheres including DTA measurement. Horizontal dotted line indicates the mass of pure LaCoO₃.

Significantly larger samples of La[Fe(CN)₆] and La[Co(CN)₆] precursors (~ 2 g) were treated during 1h in a gas-flow system composed by an electric furnace and alumina tube under several atmospheres and treatment temperatures (See Table VII-1). The evolution of the temperature during the most characteristic thermal treatments at different locations of the samples has been plotted for La[Fe(CN)₆] and for La[Co(CN)₆] in Figure VII-4 and Figure VII-5, respectively. When the furnace temperature is high enough, *i.e.*, 250°C for La[Fe(CN)₆] and 350°C for La[Co(CN)₆], a local overheating is clearly observed for both, oxygen and air atmospheres, although, it is significantly larger in the case of oxygen. Even so, TG curves showed that under air atmosphere reaction is slightly delayed (Figure VII-2 and Figure VII-3) with respect to oxygen. Therefore, we have plotted the temperature at different locations of a sample decomposed under air atmosphere for a treatment temperature 50°C higher, *i.e.* 300 °C for La[Fe(CN)₆] and 400°C for La[Co(CN)₆]. We have observed no significant difference under these temperatures with respect to experiments performed at 50°C less. While under air atmosphere the overheating is of the order of tens of degree, under oxygen thermocouples register a rise of hundreds. As expected, when nitrogen was used as the surrounding gas, the sample temperature closely followed the furnace temperature during the whole treatment. In addition, under oxygen atmosphere, we observed a local overheating that propagates through

the sample, *i.e.*, a combustion front is set. Moreover, if the furnace power is turned off when the thermal runaway starts, the reaction is self-sustained, *i.e.*, further heating is not necessary for the reaction to progress (Figure VII-4c and Figure VII-5c). Therefore, one can assume that $\text{La}[\text{Fe}(\text{CN})_6]$ and $\text{La}[\text{Co}(\text{CN})_6]$ under oxygen atmosphere decompose via combustion provided that the sample is large enough. The minimum thickness above which these precursors decompose via combustion process is determined by several experimental settings such as the sample geometry, the thermal conductivity or the ignition mode. Thus, critical thickness of the experiments carried out in the gas flow system cannot be directly extrapolated from the TG curves. The whole decomposition process of both heteronuclear cyano complex precursors lasted about 20 min. Taking into account that the sample was 5 cm long, it means that the front propagates at a velocity of $2.5 \text{ mm}\cdot\text{min}^{-1}$, which is an extremely slow speed for a combustion process⁴³.

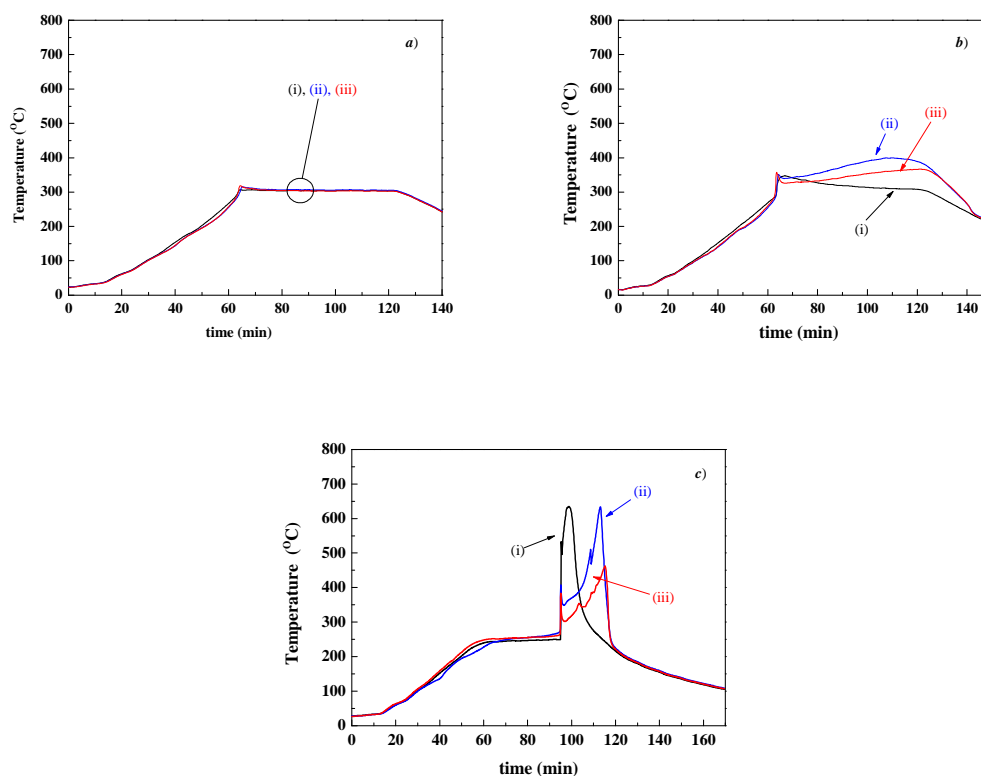


Figure VII-4. Evolution of the temperature at different positions of the sample: the extreme closer to the gas entrance(i), in the middle (ii) and at the extreme opposite to the gas entrance(iii). $\text{La}[\text{Fe}(\text{CN})_6]$ treated under different atmospheres and during different times: (a) N_2 -300°C-1h , (b) Air-300°C-1h (c) O_2 -250°C. The furnace is powered off after combustion starts (approximately 40min. at 250°C).

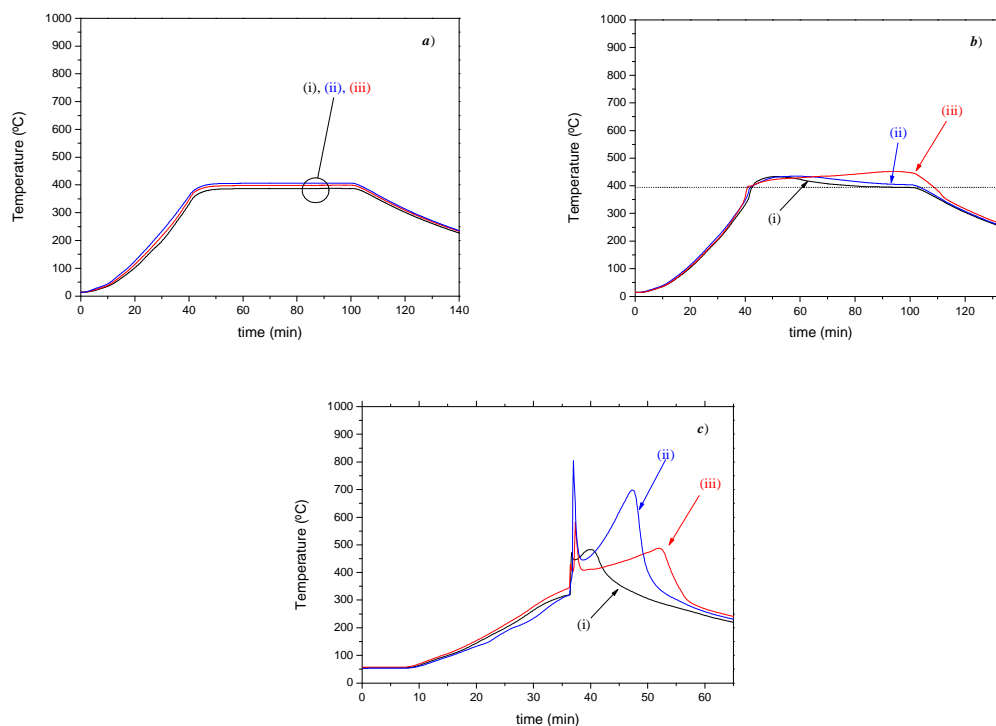


Figure VII-5. Evolution of the temperature at different positions of the sample: the extreme closer to the gas entrance (i), in the middle (ii) and at the extreme opposite to the gas entrance(iii). La[Co(CN)₆] treated under different atmospheres and during different times: (a) N₂-400°C-1h , (b) Air-400°C-1h, (c) O₂-350°C. The furnace is powered off after combustion starts (approximately 2 min. at 350°C).

The XRD patterns related to the experiments listed in Table VII-1 are plotted in Figure VII-6 and Figure VII-7. It can be noted that only in those experiments that undergo a combustion process the desired perovskite oxide crystallizes. This is consistent with the TG experiments. XRD patterns b and c of Figure 7 reveals the presence of carbonates and/or nitrates derived from oxidation of cyano group when La[Co(CN)₆] is decomposed at 350°C, i.e. under volumetric combustion. Therefore, combustion does not guarantee the complete removal of carbon and/or nitrogen. As can be seen in Figure VII-3a, sample mass lost during decomposition corresponds with the expected one if reaction product is pure LaCoO₃. This means either carbonate or nitrate species is formed. This contradiction could be explained by the assumption that by increasing the thickness, the oxygen diffusion through the sample is reduced. This makes more difficult to remove the carbon and the nitrogen of the precursor. Then, it is logical to expect that the amounts of carbonates and nitrates could be controlled by controlling the oxygen diffusion. As the other possibility, the amounts of carbonates and nitrates may be affected by the thickness, particle size or gas flux rate. Under nitrogen atmosphere, La[Fe(CN)₆] and La[Co(CN)₆] precursors are not completely decomposed even at 300 and 400°C, respectively. Under air, LaCoO₃ starts to crystallize at 400°C. However, sample

temperature is too low so that it would be necessary to make the treatment duration significantly longer to achieve a product as crystalline as the obtained under oxygen atmosphere at 350°C.

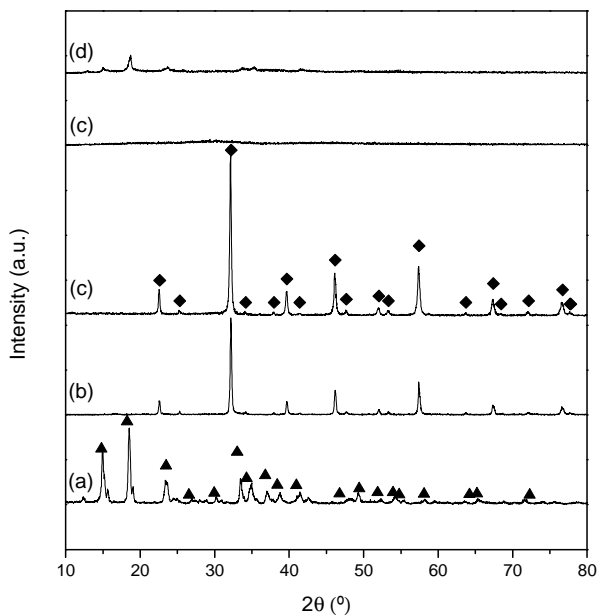


Figure VII-6. XRD patterns of $\text{La}[\text{Fe}(\text{CN})_6] \cdot 5\text{H}_2\text{O}$ treated under different atmospheres and during different times: (a) O_2 -200°C-1h, (b) O_2 -250°C-1h (c) O_2 -250°C-Furnace powered off once combustion starts (approximately 40 min at 250°C), (d) N_2 -300°C-1h, (e) Air-300°C-1h. \blacklozenge : LaFeO_3 , \blacktriangle : $\text{La}[\text{Fe}(\text{CN})_6]$.

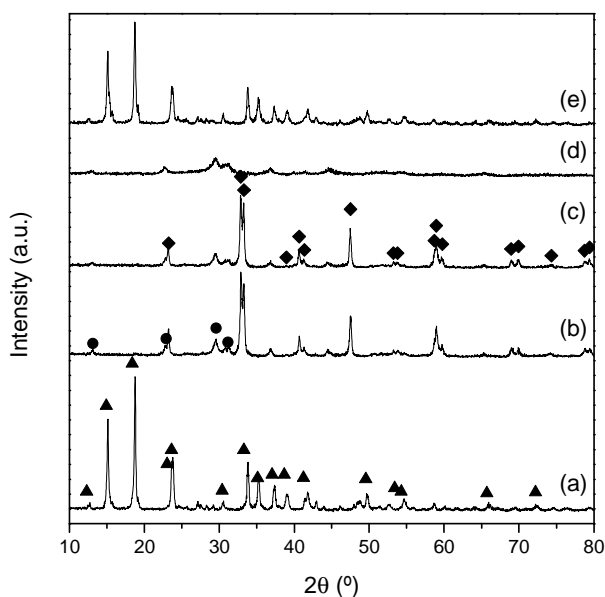


Figure VII-7. XRD patterns of $\text{La}[\text{Co}(\text{CN})_6] \cdot 5\text{H}_2\text{O}$ treated under different atmospheres and during different times: (a) O_2 -300°C-1h, (b) O_2 -350°C-1h (c) O_2 -350°C-Furnace powered off once combustion starts (approximately 2 min. at 350°C), (d) N_2 -400°C-1h, (e) Air-400°C-1h. \blacklozenge : LaCoO_3 , \bullet : La_2CO_5 , \blacktriangle : $\text{La}[\text{Co}(\text{CN})_6]$.

Table VII-1. Experiments performed with the gas flow system.

Precursor	Atmosphere	Treatment temperature (°C)	Treatment duration (h)
La[Fe(CN) ₆]	O ₂	200	1
La[Fe(CN) ₆]	O ₂	250	1
La[Fe(CN) ₆]	O ₂	250	Furnace power off once combustion starts
La[Fe(CN) ₆]	Air	250	1
La[Fe(CN) ₆]	Air	300	1
La[Fe(CN) ₆]	N ₂	250	1
La[Fe(CN) ₆]	N ₂	300	1
La[Co(CN) ₆]	O ₂	300	1
La[Co(CN) ₆]	O ₂	350	1
La[Co(CN) ₆]	O ₂	350	Furnace power off once combustion starts
La[Co(CN) ₆]	Air	350	1
La[Co(CN) ₆]	Air	400	1
La[Co(CN) ₆]	N ₂	350	1
La[Co(CN) ₆]	N ₂	400	1

VII.4.2. Production of LaFeO₃ and LaCoO₃ perovskite-type oxides via. SHS

In view of the previous results, the possibility of producing LaMO₃ perovskite oxides by SHS has been considered. In this section, we report the effect of preheating the sample up to a specific temperature before the combustion front is set by ignition.

In Figure VII-8 and Figure VII-9, XRD patterns of La[Fe(CN)₆] and La[Co(CN)₆] decomposed by solid state combustion via electric ignition are shown. It can be seen that perovskite-type oxides are formed even at room temperature. In addition, it should be noted in Figure VII-9 that the XRD peaks corresponding to La₂CO₅ carbonate were observed after the combustion of La[Co(CN)₆], although the amount of carbonate seems to decrease when the sample is preheated at higher temperatures. A low intensity peak appears at 18.7° in the La[Fe(CN)₆] sample preheated at 50°C and in the La[Fe(CN)₆] sample preheated at 100°C, indicating that in

some cases the small amounts of precursor left unreacted. The high concentration of defects such as unreacted precursor or intermediate compounds is characteristic of this technique and usually improve the catalytic activity of the final product by increasing the specific surface area.

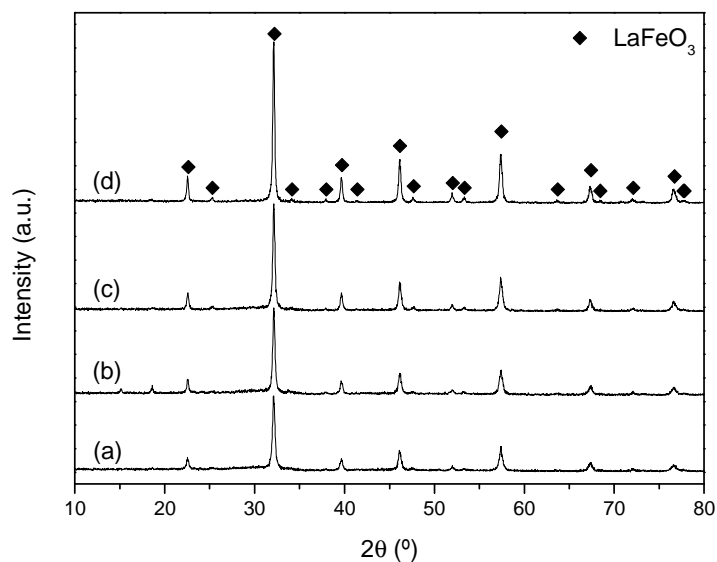


Figure VII-8. XRD patterns of LaFeO₃ produced by SHS. Electric ignition at room temperature (a), 50°C (b), 100°C(c), and 150°C (d). ◆:LaFeO₃.

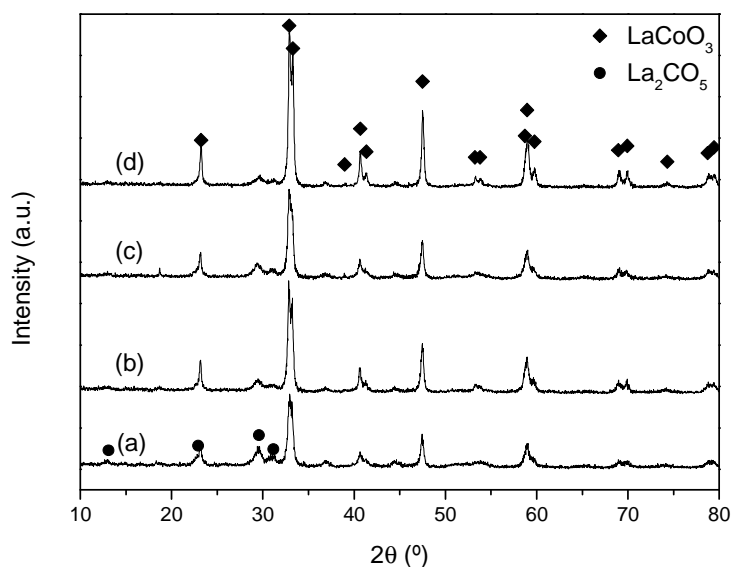


Figure VII-9. XRD patterns of LaCoO₃ produced by SHS. Electric ignition at room temperature (a), 50°C (b), 100°C(c), and 150°C (d). ●: La₂CO₅, ◆:LaCoO₃.

Figure VII-10 shows the photographs of $\text{La}[\text{Fe}(\text{CN})_6]$ and $\text{La}[\text{Co}(\text{CN})_6]$ samples and their corresponding perovskite-type oxides produced after the SHS treatment. It is clearly observed that those samples are not homogeneous. The product obtained by the decomposition of $\text{La}[\text{Fe}(\text{CN})_6]$ presents different shades with brown color. Although the product of decomposing $\text{La}[\text{Co}(\text{CN})_6]$ is all black, some white unreacted precursors remain in the vicinity of the supporting glass tube. It is important to emphasize that these precursors do not decompose by an explosive reaction but by a slow combustion process. This is particularly suited to the synthesis of films because all the reacted sample remains on the support. Independently of the preheating temperature, particle morphology and size are very similar as shown in the scanning electrons micrographs (SEM) of Figure VII-11 and Figure VII-12. The intensity peaks of X-ray diffraction appear to be higher when the sample is preheated at a higher temperature.

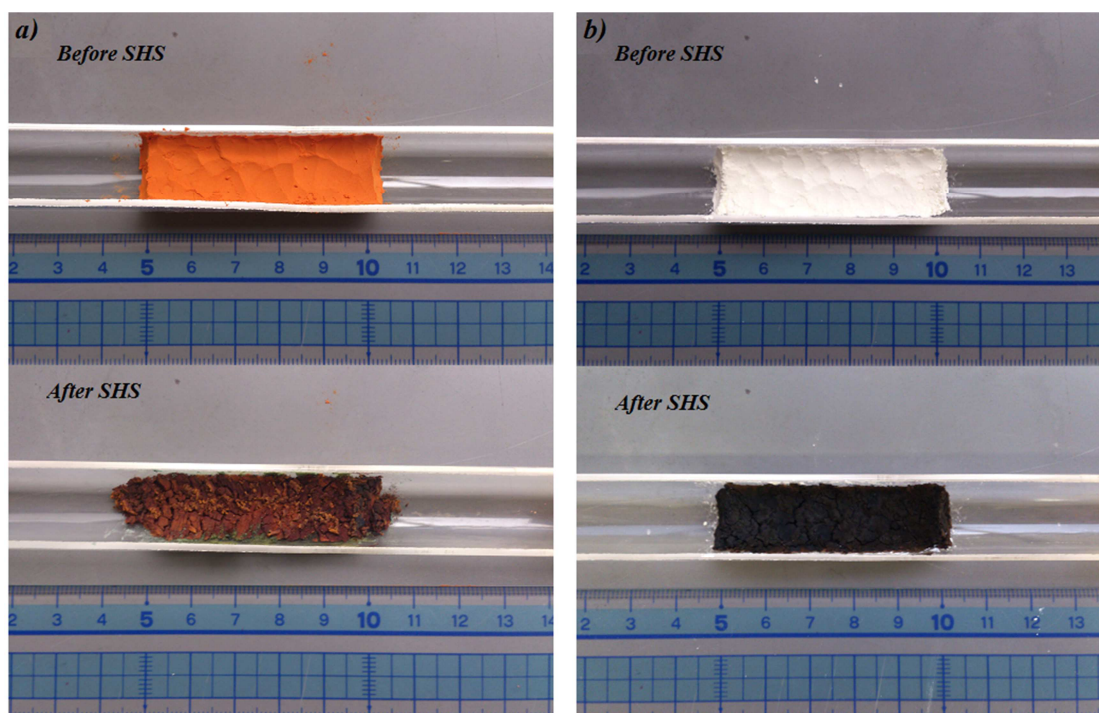


Figure VII-10. Photographs of LaFeO_3 (a) and LaCoO_3 (b)samples and its respectively perovskite-type oxides produced by SHS.

The specific surface areas (SSA)of the previous samples are summarized in Table VII-2. The SSA of LaFeO_3 produced by the decomposition of $\text{La}[\text{Fe}(\text{CN})_6]$ via solid state combustion decreased with increasing preheating temperature: $30 \text{ m}^2 \cdot \text{g}^{-1}$ at 50°C of preheating temperature and $15 \text{ m}^2 \cdot \text{g}^{-1}$ at 150°C . The LaCoO_3 counterparts range from 12 to $8 \text{ m}^2 \cdot \text{g}^{-1}$. It could be expected that the combustion front temperature will increase by increasing the preheating furnace

temperature. Consequently the crystallinity of the sample will also increase. However, there is a low correlation between SSA and the ignition temperature. This is probably related to the variations in the combustion front temperature while crossing the sample (Figure VII-4c and Figure VII-5c). Therefore, it is difficult to obtain a homogeneous product (Figure VII-10). However, it is significant that the SSAs of LaFeO₃ and LaCoO₃ synthesized by the present method are much larger than those of LaMO₃ perovskite oxides synthesized by SHS (0.116-0758 m²/g)^{26,27}.

Table VII-2. Specific surface area of perovskite-type oxides obtained by SHS

Precursor	Ignition temperature (°C)	SSA (m²·g⁻¹)
La[Fe(CN) ₆]	Room temperature	17.8
La[Fe(CN) ₆]	50	25.6
La[Fe(CN) ₆]	100	28.6
La[Fe(CN) ₆]	150	17.2
La[Co(CN) ₆]	Room temperature	11.3
La[Co(CN) ₆]	50	10.2
La[Co(CN) ₆]	100	12.3
La[Co(CN) ₆]	150	8.4

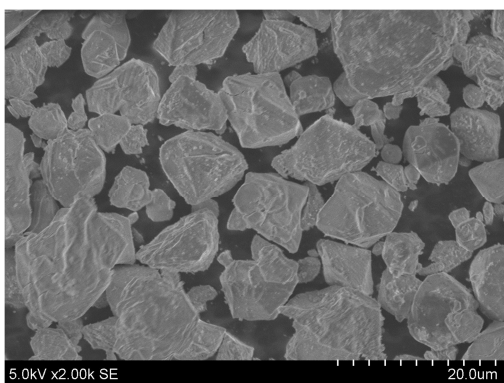
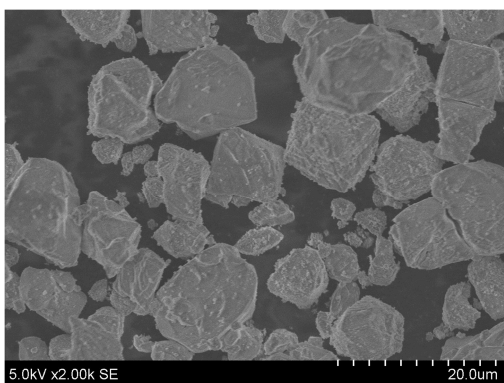
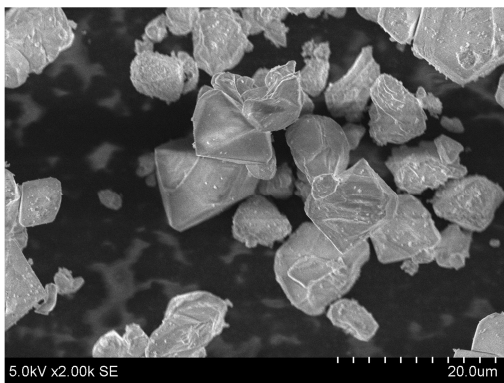
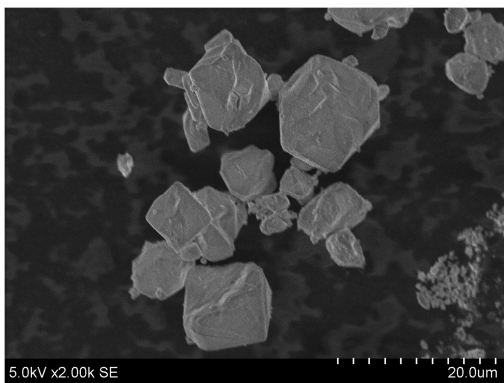


Figure VII-11. From top to bottom: SEM micrographs of LaFeO_3 produced by SHS at an ignition temperature of 150°C, 100°C, 50°C, and room temperature.

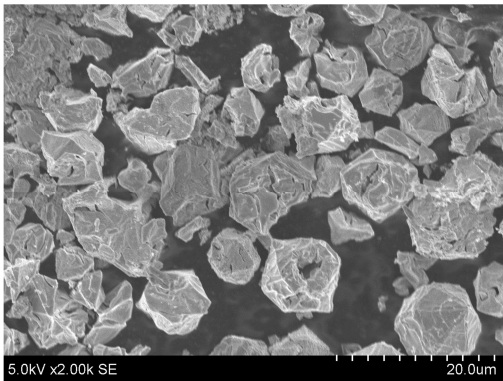
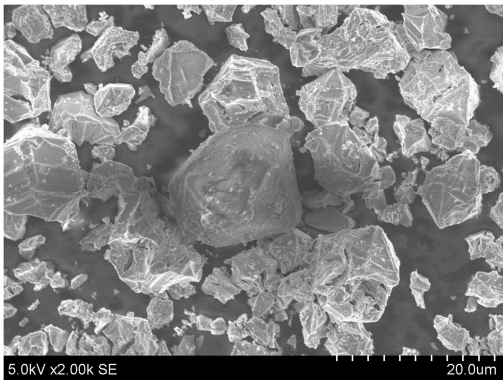
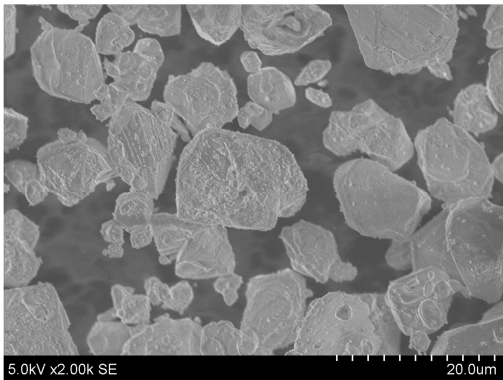
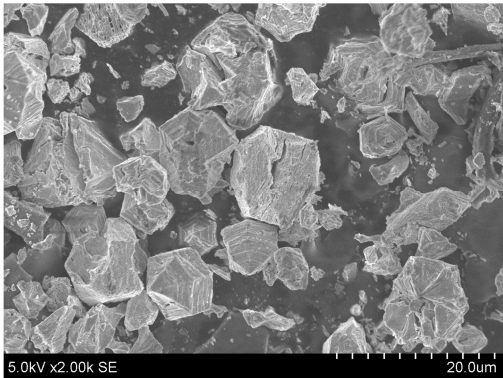


Figure VII-12. From top to bottom: SEM micrographs of LaCoO_3 produced by SHS at an ignition temperature of 150°C, 100°C, 50°C, and room temperature.

VII.5. Conclusions

(1) $\text{La}[\text{Fe}(\text{CN})_6]$ and $\text{La}[\text{Co}(\text{CN})_6]$ decompose via a combustion process under oxygen atmosphere when sample is large enough. This fact allows the synthesis of perovskite-type oxides at temperatures that otherwise would be significantly higher.

(2) LaFeO_3 and LaCoO_3 perovskite-type oxide were successfully produced by the SHS method even at room temperature. However, we have not been able to obtain carbon free LaCoO_3 even if the cyano complex precursor is preheated up to 150°C .

(3) The specific surface area of LaFeO_3 and LaCoO_3 perovskite-type oxides produced via SHS using heteronuclear cyano metal complex as precursors was higher than that of LaMO_3 obtained with the same technique but using other precursors.

VII.6. Acknowledgment

This work was partially funded by the KAKENHI Grant Number 24560948. D. S.-R. thanks the University of Girona and the NESSIE program for the PhD fellowships.

VII.7. References

1. Jr., D. W. J., Gallagher, P. K., Wertheim, G. K. & Vogel, E. M. The nature and effects of platinum in perovskite catalysts. *J. Catal.* **48**, 87–97 (1977).
2. Yasuda, H., Fujiwara, Y., Mizuno, N. & Misono, M. Oxidation of carbon monoxide on $\text{LaMn}_{1-x}\text{Cu}_x\text{O}_3$ perovskite-type mixed oxides. *J. Chem. Soc., Faraday Trans.* **90**, 1183–1189 (1994).
3. Barbero, B. P., Gamboa, J. A. & Cadús, L. E. Synthesis and characterisation of $\text{La}_{1-x}\text{Ca}_x\text{FeO}_3$ perovskite-type oxide catalysts for total oxidation of volatile organic compounds. *Appl. Catal. B Environ.* **65**, 21–30 (2006).
4. Teraoka, Y., Fukuda, H. & Kagawa, S. Catalytic Activity of Perovskite-Type Oxides for the Direct Decomposition of Nitrogen Monoxide. *Chem. Lett.* **19**, 1–4 (1990).

5. Teraoka, Y., Nakano, K., Shangguan, W. & Kagawa, S. Simultaneous catalytic removal of nitrogen oxides and diesel soot particulate over perovskite-related oxides. *Catal. Today* **27**, 107–113 (1996).
6. Dai, H., He, H., Li, P., Gao, L. & Au, C.-T. The relationship of structural defect–redox property–catalytic performance of perovskites and their related compounds for {CO} and {NO_x} removal. *Catal. Today* **90**, 231–244 (2004).
7. Minh, N. Q. Ceramic Fuel Cells. *J. Am. Ceram. Soc.* **76**, 563–588 (1993).
8. Inoue, T., Seki, N., Eguchi, K. & Arai, H. Low-Temperature Operation of Solid Electrolyte Oxygen Sensors Using Perovskite-Type Oxide Electrodes and Cathodic Reaction Kinetics. *J. Electrochem. Soc.* **137**, 2523–2527 (1990).
9. Alcock, C. B., Doshi, R. C. & Shen, Y. Perovskite electrodes for sensors. *Solid State Ionics* **51**, 281–289 (1992).
10. Shuk, P. *et al.* Electrodes for oxygen sensors based on rare earth manganites or cobaltites. *Sensors Actuators B Chem.* **16**, 401–405 (1993).
11. Shimizu, Y., Shimabukuro, M., Arai, H. & Seiyama, T. ENHANCEMENT OF HUMIDITY SENSITIVITY FOR PEROVSKITE-TYPE OXIDES HAVING SEMICONDUCTIVITY. *Chem. Lett.* **14**, 917–920 (1985).
12. Lukaszewicz, J. P. Diode-type humidity sensor using perovskite-type oxides operable at room temperature. *Sensors Actuators B Chem.* **4**, 227–232 (1991).
13. OBAYASHI, H. & KUDO, T. Properties of Oxygen Deficient Perovskite Type Compounds and Their Application as Alcohol Sensors. *Nippon KAGAKU KAISHI* **1980**, 1568–1572 (1980).
14. Yu, C., Shimizu, Y. & Arai, H. INVESTIGATION ON A LEAN-BURN OXYGEN SENSOR USING PEROVSKITE-TYPE OXIDES. *Chem. Lett.* **15**, 563–566 (1986).
15. Post, M. L., Sanders, B. W. & Kennepohl, P. Thin films of non-stoichiometric perovskites as potential oxygen sensors. *Sensors Actuators B Chem.* **13**, 272–275 (1993).
16. Li, W. B., YONEYAMA, H. & TAMURA, H. Correlation between Catalytic Activity for CO Oxidation and Sensor Response to CO of LaFeO₃ and Related Perovskite Oxides. *Nippon KAGAKU KAISHI* **1982**, 761–767 (1982).

17. Taguchi, H. & Takahashi, Y. Effect of CO oxidation on electrical properties of $(\text{La}_{0.8}\text{Sr}_{0.2})\text{FeO}_3$. *J. Mater. Sci. Lett.* **3**, 251–252 (1984).
18. Arakawa, T., Takada, K.-I., Tsunemine, Y. & Shiokawa, J. CO gas sensitivities of reduced perovskite oxide LaCoO_{3-x} . *Sensors and Actuators* **14**, 215–221 (1988).
19. Matuura, Y., Matsushima, S., Sakamoto, M. & Sadaoka, Y. NO_2 -sensitive LaFeO_3 film prepared by thermal decomposition of the heteronuclear complex, $\{\text{La}[\text{Fe}(\text{CN})_6] \cdot 5\text{H}_2\text{O}\}_x$. *J. Mater. Chem.* **3**, 767–769 (1993).
20. Traversa, E. *et al.* NO_2 sensitive LaFeO_3 thin films prepared by r.f. sputtering. *Sensors Actuators B Chem.* **25**, 661–664 (1995).
21. Arakawa, T., Kurachi, H. & Shiokawa, J. Physicochemical properties of rare earth perovskite oxides used as gas sensor material. *J. Mater. Sci.* **20**, 1207–1210 (1985).
22. Royer, S., Bérubé, F. & Kaliaguine, S. Effect of the synthesis conditions on the redox and catalytic properties in oxidation reactions of $\text{LaCo}_{1-x}\text{Fe}_x\text{O}_3$. *Appl. Catal. A Gen.* **282**, 273–284 (2005).
23. Bell, R. J., Millar, G. J. & Drennan, J. Influence of synthesis route on the catalytic properties of $\text{La}_{1-x}\text{Sr}_x\text{MnO}_3$. *Solid State Ionics* **131**, 211–220 (2000).
24. Rida, K., Benabbas, A., Bouremmad, F., Peña, M. A. & Martínez-Arias, A. Surface properties and catalytic performance of $\text{La}_{1-x}\text{Sr}_x\text{CrO}_3$ perovskite-type oxides for CO and C_3H_6 combustion. *Catal. Commun.* **7**, 963–968 (2006).
25. Merzhanov, A. G. History and recent developments in SHS. *Ceram. Int.* **21**, 371–379 (1995).
26. Hirano, T., Purwanto, H., Watanabe, T. & Akiyama, T. Self-propagating high-temperature synthesis of Sr-doped LaMnO_3 perovskite as oxidation catalyst. *J. Alloys Compd.* **441**, 263–266 (2007).
27. Hirano, T., Tosho, T., Watanabe, T. & Akiyama, T. Self-propagating high-temperature synthesis with post-heat treatment of $\text{La}_{1-x}\text{Sr}_x\text{FeO}_3$ ($x = 0-1$) perovskite as catalyst for soot combustion. *J. Alloys Compd.* **470**, 245–249 (2009).
28. Ming, Q., Nersesyan, M. D., Richardson, J. T., Luss, D. & Shiryayev, A. A. A new route to synthesize $\text{La}_{1-x}\text{Sr}_x\text{MnO}_3$. *J. Mater. Sci.* **35**, 3599–3606 (2000).

29. Patil, K. C., Aruna, S. T. & Mimani, T. Combustion synthesis: An update. *Curr. Opin. Solid State Mater. Sci.* **6**, 507–512 (2002).
30. Zhu, C., Nobuta, A., Nakatsugawa, I. & Akiyama, T. Solution combustion synthesis of LaMO_3 (M = Fe, Co, Mn) perovskite nanoparticles and the measurement of their electrocatalytic properties for air cathode. *Int. J. Hydrogen Energy* **38**, 13238–13248 (2013).
31. Civera, A., Pavese, M., Saracco, G. & Specchia, V. Combustion synthesis of perovskite-type catalysts for natural gas combustion. *Catal. Today* **83**, 199–211 (2003).
32. González-Cortés, S. L. & Imbert, F. E. Fundamentals, properties and applications of solid catalysts prepared by solution combustion synthesis (SCS). *Appl. Catal. A Gen.* **452**, 117–131 (2013).
33. Sadaoka, Y., Traversa, E. & Sakamoto, M. Preparation and Characterization of Heteronuclear Hexacyano Complexes, $\text{Ln}_x\text{Sm}_{1-x}[\text{Co}(\text{CN})_6] \cdot n\text{H}_2\text{O}$ (Ln = La, Er, and Yb). *Chem. Lett.* **25**, 177–178 (1996).
34. Sadaoka, Y., Traversa, E. & Sakamoto, M. Preparation and structural characterization of perovskite-type $\text{La}_x\text{Ln}_{1-x}\text{CoO}_3$ by the thermal decomposition of heteronuclear complexes, $\text{La}_x\text{Ln}_{1-x}[\text{Co}(\text{CN})_6] \cdot n\text{H}_2\text{O}$ (Ln = Sm and Ho). *J. Alloys Compd.* **240**, 51–59 (1996).
35. SAKAMOTO, M. *et al.* Preparation of Perovskite-Type Oxides by the Thermal Decomposition of Heteronuclear Complexes, $\text{Ln}[\text{Fe}_x\text{Co}_{1-x}(\text{CN})_6] \cdot 4\text{H}_2\text{O}$ (Ln=Pr-Yb). *J. Ceram. Soc. Japan* **105**, 963–969 (1997).
36. Traversa, E. *et al.* Thermal evolution of the microstructure of nanosized LaFeO_3 powders from the thermal decomposition of a heteronuclear complex, $\text{La}[\text{Fe}(\text{CN})_6] \cdot 5\text{H}_2\text{O}$. *J. Mater. Res.* **13**, 1335–1344 (1998).
37. Traversa, E., Nunziante, P., Sakamoto, M., Sadaoka, Y. & Montanari, R. Synthesis and Structural Characterization of Trimetallic Perovskite-Type Oxides, $\text{LaFe}_x\text{Co}_{1-x}\text{O}_3$, by the Thermal Decomposition of Cyano Complexes, $\text{La}[\text{Fe}_x\text{Co}_{1-x}(\text{CN})_6] \cdot n\text{H}_2\text{O}$. *Mater. Res. Bull.* **33**, 673–681 (1998).

- 38 Sadaoka, Y., Aono, H., Traversa, E. & Sakamoto, M. Thermal evolution of nanosized LaFeO₃ powders from a heteronuclear complex, La[Fe(CN)₆]·nH₂O. *J. Alloys Compd.* **278**, 135–141 (1998).
- 39 Aono, H., Sato, M., Traversa, E., Sakamoto, M. & Sadaoka, Y. Design of Ceramic Materials for Chemical Sensors: Effect of SmFeO₃ Processing on Surface and Electrical Properties. *J. Am. Ceram. Soc.* **84**, 341–347 (2001).
- 40 Sánchez-Rodríguez, D., Eloussifi, H., Farjas, J., Roura, P. & Dammak, M. Thermal gradients in thermal analysis experiments: Criteria to prevent inaccuracies when determining sample temperature and kinetic parameters. *Thermochim. Acta* **589**, 37–46 (2014).
- 41 Sanchez-Rodriguez, D. *et al.* Thermal Analysis for Low Temperature Synthesis of Oxide Thin Films from Chemical Solutions. *J. Phys. Chem. C* **117**, 20133–20138 (2013).
- 42 Frank-Kamenetskii. Diffusion and Heat Exchange in Chemical Kinetics. (1955).
- 43 Yeh, C.-L. in *Encyclopedia of Materials: Science and Technology (Second Edition)* 1–8 (Elsevier, 2010)

VIII. GENERAL DISCUSSION

With the aim of obtaining advanced oxide thin films at low temperatures, we have investigated the decomposition kinetics of metal-organic precursors. In particular, our objective was to characterise the transformation rate limiting mechanisms with a view to their optimisation, possibly lowering the temperature at which decomposition takes place. In addition, we also sought the conditions in which combustion occurs, since a combustion front significantly lowers the synthesis temperature. The decomposition evolution was monitored by TG analysis of the precursors in the form of powders and films and for different gas and temperature conditions. Our research shows that films and powders generally exhibit dissimilar decomposition kinetics (see Figure III-1). In the TG curves of powders, we observe a characteristic abrupt mass loss step, which is a feature of a thermal runaway process. In contrast, the TG curves of films of the same precursors show a smooth evolution, indicating that the decomposition rate is much lower than in powders and suggesting that combustion does not occur in films. In addition, we have observed that decomposition begins at lower temperatures.

We have performed calculations in an attempt to simulate the evolution of these reactions in films and powders. The simulations consider heat transport by diffusion through the sample as well as local heat generation resulting from the decomposition reaction. We tested both constant temperature rises and constant temperatures. We developed a numerical procedure to solve the PDE-ODE model described by Eq. 1,2 and 3 (Section I-3) based on an implicit finite difference scheme.

We checked the model's ability to describe real processes by analysing the decomposition of two metalorganic precursors, yttrium trifluoroacetate, $Y(CF_3COO)_3$, $Y(TFA)_3$, and barium trifluoroacetate, $Ba(CF_3COO)_2$, $(Ba(TFA)_2)$, in the form of powders and films. Figure VI-2 confirms that the numerical model successfully describes the evolution of the $Y(TFA)_3$ decomposition. Unlike $Y(TFA)_3$, the reaction of $Ba(TFA)_2$ depends on the composition of the surrounding atmosphere and, in the particular case of $Ba(TFA)_2$, the reaction is enhanced by the presence of O_2 . Moreover, this transformation is governed by the superposition of two different mechanisms and so the working hypothesis of the involvement of a first order reaction is not accurate. Therefore, our numerical model provides a rather poor prediction of the evolution of the $Ba(TFA)_2$ transformation – in Figure VI-12 it can be seen how our model fails to provide an accurate prediction of the whole evolution of $Ba(TFA)_2$ – but does provide a good description of the first stages of the reaction and so permits the analysis of the necessary conditions for a thermal runaway.

Note that the results presented here indicate that thermal analysis may be used to monitor combustion processes in powders, permitting the exploration of the possibility of using combustion to synthesise advanced oxides at low temperatures.

Temperature gradients cannot be formed in thin films since, as is confirmed by our calculations, heat is efficiently dissipated in these samples towards the substrate by means of conduction. In addition to the slight thickness of the samples, their conductivity, which is high in comparison with powders, is also a hindrance in thin films. While films are composed of a single solid block that facilitates heat transport, the network of solid particles that powders form is extremely inefficient. Conductivity is such an important parameter in our model that it must be experimentally determined in order to give consistency to our results. To this end we have developed a new method to determine the thermal conductivity of powders by DSC based on Camiran.¹ Our results confirm that the thermal conductivity of powders is similar to that of the surrounding gas,² irrespective of the conductivity of the bulk counterparts.

This key feature makes it possible to apply the SHS combustion synthesis technique in powders. Powders produced by combustion synthesis have a high concentration of defects,³ such as remnants of the initial precursor or intermediate compounds. This is especially interesting for catalytic purposes since it increases the surface area of the desired oxides. Taking advantage of this, we successfully synthesized perovskite-type oxides, which are widely used in environmental-friendly catalytic systems, by SHS from heteronuclear cyano metal complex precursor powders. Furthermore, the oxide powders obtained from cyano complex precursors were up to two orders of magnitude higher than those of other LaMO_3 produced using the same technique using other precursors.^{4,5}

Although in some instances it is assumed that the occurrence of a thermal runaway is linked to highly exothermic processes, our research, as well as a revision of the literature, lead us to conclude that local overheating can occur in relatively low enthalpy reactions, e.g., such as those of the decomposition of metal-organic precursors analysed in this work. Therefore, in order to analyse the critical condition for combustion to occur, we revisited Frank Kaminestkii's model.⁶ The FK parameter has some limitations associated with the assumptions of its derivation. First, the reactant consumption is neglected and it is assumed that $R_G T_0 / E_A \ll 1$. In addition, the FK model also assumes that the furnace temperature is kept constant (isothermal treatment). Furthermore, the FK analytical solution is restricted to idealised geometries that allow the system to be reduced to a one-dimensional model. In order to make the model applicable to more realistic cases, we have modified the FK

parameter, improving its accuracy by including continuous heating temperature programs and taking into account the dependence on the aspect ratio in cylindrical geometries.

Although the FK model provides an accurate prediction for highly exothermic reactions and low furnace temperatures, there are significant inaccuracies for less exothermic reactions and high furnace temperatures as the FK model neglects the reactant consumption during the induction period. Figure VI-6 shows that the FK model becomes inaccurate when the consumption of the reactant before thermal explosion approaches 0.1.

Deviations from the FK model have been solved by means of a first order correction based on the initial reactant consumption, α_{ind} and numerical simulations show that the value of the FK parameter follows a lineal dependence on α_{ind} :

$$\Lambda_{cr,Iso,0}^{(1D)} = C_0^{(1D)} \times (1 + 10.91 \alpha_{Ind,Iso}) \quad (1)$$

Once the FK parameter has been determined, it is straightforward to determine the critical sample thickness below which thermal explosion is not possible:

$$d_{cr} = \sqrt{\Lambda_{cr} \frac{a}{A} \frac{R_G}{E_A} \frac{T_0^2}{\Delta T_{AD}} \exp\left(\frac{E_A}{R_G T_0}\right)} \quad (2)$$

Thus, a decrease in the activation energy or an increase in the furnace temperature will facilitate the thermal explosion. This conclusion agrees with the qualitative criterion that combustion occurs when reaction rates are strongly temperature dependent.⁷

As mentioned above, we have also extended the FK model to describe the critical condition for combustion when a furnace is submitted to a constant temperature rise: $T_f = T_{in} + bt$.

Our approach starts from the fact that the reaction time is as functionally dependent on temperature in non-isothermal conditions as it is in isothermal conditions but we replace T_{Iso} with the temperature at which the reaction rate is at its maximum, T_{Max} , which is expressed by Kissinger's formula. This temperature can easily be calculated analytically.^{8,9} Following the same approach that we used for the isothermal case, the FK parameter is described by a linear dependence on the initial reactant consumption:

$$\Lambda_{cr,CHR,0}^{(1D)} = C_0^{(1D)} \times 4.5 \times (1 + 5.8 \alpha_{Ind,CHR}) \quad (3)$$

However, the isothermal case is not achieved when $b \rightarrow 0$ due to the differences in the initial furnace temperature in the two thermal treatments. Note that the FK parameter is greater in non-isothermal conditions than in isothermal conditions. This means that combustion can be achieved at a lower critical temperature under isothermal conditions.

In the case of films, the effect that the substrate has on combustion has also been analysed. It is found that the substrate makes two opposing contributions to the critical thickness. On the one hand, low substrate conductivity hinders the transport of heat from the sample to the substrate, lowers the heat dissipation through the substrate, and enhances combustion (i.e. the critical thickness is reduced). On the other hand, low substrate diffusivity and large substrate thickness results in a temperature gradient along the substrate that slows the transfer of heat from the furnace to the sample thus making combustion more difficult (i.e. the critical thickness increases). Therefore, the minimum critical thickness is related to the opposing effects of thermal conductivity and thermal diffusivity.

It should be noted that in the case of films, it is virtually impossible to achieve thermal explosion for thicknesses below 1 μm , even in the case of highly exothermic reactions.

The FK parameter coincides with the ratio of the reaction time versus the diffusion time. Since diffusion depends on the geometry, we have reformulated the diffusion time to adapt the FK parameter for two-dimensional problems:

$$t_D^{(2D)} = \frac{1}{C^{(2D)}} \frac{(d^{(2D)})^2}{a}. \quad (4)$$

where $C^{(2D)}$ is a constant that depends on the geometry and $d^{(2D)} \equiv V^{1/3}$ is the characteristic length of the system

$$C^{(2D)} = C_0^{(1D)} \left[\pi \left(\frac{R}{H} \right)^2 \right]^{2/3} + C_\infty^{(1D)} \left[\pi \frac{H}{R} \right]^{2/3} \quad (5)$$

In this case it is more convenient to determine critical mass rather than critical thickness:

$$m_{cr, Iso} = \rho \left[\Lambda_{cr, Iso}^{(2D)} \frac{a}{A} \frac{R_G}{E_A} \frac{T_{Iso}^2}{\Delta T_{AD}} \exp \left(\frac{E_A}{R_G T_{Iso}} \right) \right]^{3/2} \quad (6)$$

$$m_{cr,CHR} = \rho \left[\Lambda_{cr,CHR}^{(2D)} \frac{a R_G T_{CHR}^2}{A E_A \Delta T_{AD}} \exp\left(\frac{E_A}{R_G T_{CHR}}\right) \right]^{3/2} \quad (7)$$

Testing our model with real TG experiments, we have observed that the samples that are subjected to combustion have masses that agree reasonably with our theoretical predictions.

The removal of heat from the sample becomes more difficult as thickness is increased. Therefore, overheating will occur above a certain sample mass value given that this is the result of relatively low heat dissipation. Thus, the endset temperature shifts to an apparently lower value and the duration of the process is reduced as the sample mass is increased. This odd behaviour has been experimentally reported for BaTFA powders (Figure IV-3) as well as for the cyano complex precursors that we used for the synthesis of perovskite-type oxides via SHS (Figure VII-2Figure VII-3.a).

The accuracy when determining the sample temperature in TA experiments is called into question by the occurrence of overheating above a critical sample mass. This also applies to kinetic parameters since the reaction kinetic is also altered. Therefore, we have established a criterion to determine the maximum sample mass in TA experiments. In addition, we have checked the validity of non-isothermal kinetic analysis.

First, we have analysed two different effects that contribute to deviations when determining the sample temperature: the thermal gradients related to heat transport through the sample and heat evolved due to endothermic or exothermic reactions of the sample.

Following the same approach used in the formulation of the two-dimensional expression of the diffusion time (Eq.4), we have related the temperature delay to heat conduction:

$$\Delta T \equiv T(R, 0) - T(0, h) = C \frac{b}{a} V^{2/3} \quad (8)$$

Where C is a shape factor that accounts for the particular geometry and depends exclusively on the h/Rratio. C has been determined numerically.

$$C = \frac{1}{2} \left(\frac{(h/R)^2}{\pi + 2\pi\sqrt{2}(h/R)^3} \right)^{2/3} \quad (9)$$

This allowed us to calculate a critical sample mass related to heat transport assuming a maximum uncertainty of 1K which is within the typical range of apparatus limitations.

$$m_{crit} = \rho \left(\frac{1}{C} \frac{a}{b} \right)^{3/2} \quad (10)$$

Assuming a value of C for a typical crucible, we observed that critical masses would be 3.8 and 11.5mg for Ba(TFA)₂ and Y(TFA)₃ in the form of powders. These values broadly agree with the general criterion that sample masses should be <10mg.¹⁰ In contrast, the critical masses for indium, aluminium and alumina are 1.5, 1.7 and 0.12kg. Such huge differences between powders and bulk materials can mainly be explained by the already mentioned differences in the thermal conductivity.

With regards to overheating due to chemical reactions, we have numerically determined the value of the sample thickness that results in a temperature difference of 1K. This result indicates that the ratio between a fixed ΔT and the maximum possible overheating is equal to a fixed ratio between the diffusion and reaction times. Therefore, using the same two-dimensional expression of the diffusion time that we used in Eq. 4 we could adapt the one-dimensional case to a two-dimensional situation.

$$t_D^{(2D)} = \frac{2C}{a} V^{2/3} \quad (11)$$

Taking into account that C has the same shape factor that we used in Equation 9:

$$m_{crit} = \rho \left(\frac{5 \cdot 10^{-5} caE_a}{C} \frac{c_R}{R_G q A e^{-E_A/R_G T_{Max}}} \right)^{3/2} \quad (12)$$

Furthermore, we also developed an expression for the maximum heat flow allowed to prevent overheating:

$$\left\langle m \frac{dq}{dt} \right\rangle_{crit} = \rho \left(\frac{5 \cdot 10^{-5} caE_a}{C} \frac{c_R}{R_G} \right)^{3/2} \left(\frac{c_R}{q A e^{-E_A/R_G T_{Max}}} \right)^{1/2} \quad (13)$$

Finally, we checked the effect of overheating on the determination of the activation energy. In Fig. IV-8 we showed that the application of isoconversional methods fails when sample is overheated. However, we observed that, at the very early stages of the reaction, the values of the activation energy determined coincides either the sample is overheated or thermalizes. Moreover, we have shown an example in Fig. IV-10 that when single step reactions evolve in a combustion process the kinetic analysis results in a nearly constant activation energy and both, isoconversional method and the Kissinger method provide an approximation for the activation energy.

VIII.1. References

1. Camirand, C. P. Measurement of thermal conductivity by differential scanning calorimetry. *Thermochim. Acta* **417**, 1–4 (2004).
2. Klemensiewicz, Z. Thermal Conductivity of Powders. *Nature* **164**, 589–589 (1949).
3. Mishra, S. K., Das, S. & Pathak, L. C. Defect structures in zirconium diboride powder prepared by self-propagating high-temperature synthesis. *Mater. Sci. Eng. A* **364**, 249–255 (2004).
4. Hirano, T., Tosho, T., Watanabe, T. & Akiyama, T. Self-propagating high-temperature synthesis with post-heat treatment of $\text{La}_{1-x}\text{Sr}_x\text{FeO}_3$ ($x = 0-1$) perovskite as catalyst for soot combustion. *J. Alloys Compd.* **470**, 245–249 (2009).
5. Hirano, T., Purwanto, H., Watanabe, T. & Akiyama, T. Self-propagating high-temperature synthesis of Sr-doped LaMnO_3 perovskite as oxidation catalyst. *J. Alloys Compd.* **441**, 263–266 (2007).
6. Frank-Kamenetskii, D. A. Diffusion and Heat Exchange in Chemical Kinetics. **2nd enl. a**, (Princeton University Press, 1955).
7. Merzhanov, A. G. & Khaikin, B. I. Theory of combustion waves in homogeneous media. *Prog. Energy Combust. Sci.* **14**, 1–98 (1988).
8. Roura, P. & Farjas, J. Analytical solution for the Kissinger equation. *J. Mater. Res.* **24**, 3095–3098 (2009).
9. Farjas, J. & Roura, P. Exact analytical solution for the Kissinger equation: Determination of the peak temperature and general properties of thermally activated transformations. *Thermochim. Acta* **598**, 51–58 (2014).
10. Wendlandt, W. W. Thermal Analysis, *Wiley*, New York, 1986.

IX. GENERAL CONCLUSIONS

The main contributions of the present work are:

- Combustion in thin films is virtually impossible due to the high surface-area-to-volume ratio that enhances the efficiency of heat dissipation through the substrate. On the other hand, this high surface-area-to-volume ratio also enhances gas transport and exchange allowing advanced oxides to be synthesised at lower temperatures.
- Powders are more likely to undergo combustion than bulk materials on account of their low thermal conductivity, which is similar to that of the surrounding gas.
- Under oxygen atmosphere LaFeO_3 and LaCoO_3 perovskite-type powders can be obtained from heteronuclear cyano complex precursors by means of combustion synthesis. The surface area of LaFeO_3 and LaCoO_3 synthesised via SHS from heteronuclear cyano complex precursors is up to two orders of magnitude greater than that of similar perovskite-type oxides obtained from other precursors.
- A numerical procedure has been developed to analyse exothermic solid state chemical reactions taking into account conductive heat transfer through the sample. Simulations satisfactorily describe the main features of the evolution of TG curves for single-step reactions. On the other hand, numerical simulations fail in other situations such as those where gas transport is relevant. Notwithstanding, the combustion threshold is always well predicted with sufficient accuracy.
- We have revisited the Frank-Kamenetskii criterion taking into account reactant combustion. In addition, its applicability has been extended to cylindrical reactors and continuous heating rate temperature programs. In all cases our approach provides an accurate prediction for a wide range of parameters that cover many practical situations. Our criterion allows the minimum sample mass or sample size for combustion to occur to be established.
- The substrate or vessel walls have a negligible effect when substrate conductivity is much higher than the sample conductivity or when the sample thickness is greater than the substrate thickness, which is the usual condition for chemical reactors. Conversely, in the case of low thermal diffusivity and thick substrates, combustion is more difficult. However, the formation of a temperature gradient is slightly enhanced only in the case of relatively thin substrates with lower conductivity, in other cases the presence of a substrate hinders the formation of temperature gradients.

- We have developed a method based on Camirand's method that allows the thermal conductivity of powders to be determined using a DSC apparatus by melting a reference metal sphere that is sunk up to its equator in a hemispherical crucible completely filled with the desired powder.
- We have determined two relationships related to heat propagation and to heat released by an exothermic reaction that provide a criterion for the maximum mass to prevent the formation of temperature gradients larger than 1K within a sample in TA experiments. The aspect ratio of the sample has been taken into account.
- Although it has been shown that the kinetic analysis may lead to significant inaccuracies when the critical mass is exceeded, the activation energy and pre-exponential term can still be determined at the very earliest stages of the reaction. Moreover, in the particular case of a single-step reaction where overheating turns to a thermal runaway, isoconversional methods or the method of Kissinger provide trustworthy results.

